

NATIONAL ADVISORY COMMITTEE FOR AERONAUTICS

TECHNICAL MEMORANDUM

No. 1062

INVESTIGATION OF SINGLE STAGE AXIAL FANS

By P. Ruden

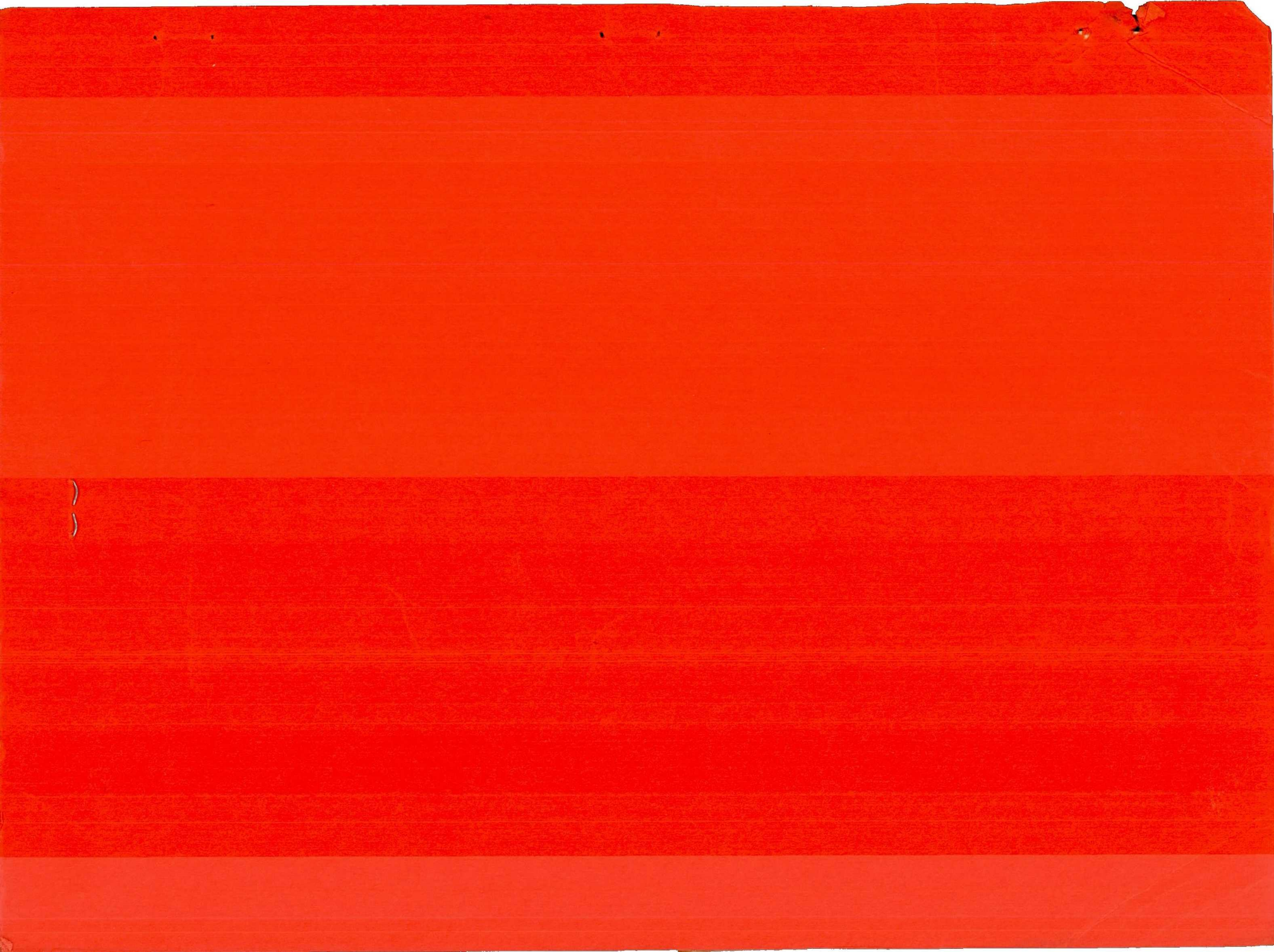
Luftfahrtforschung

Vol. 14, No. 7, July 20, 1937 and No. 9, September 20, 1937
Verlag von R. Oldenbourg, München und Berlin



Washington
April 1944

REPRODUCED BY
**NATIONAL TECHNICAL
INFORMATION SERVICE**
U. S. DEPARTMENT OF COMMERCE
SPRINGFIELD, VA. 22161



TECHNICAL MEMORANDUM NO. 1062

INVESTIGATIONS OF SINGLE-STAGE AXIAL FANS*

By P. Ruden

The following investigations are connected with experiments on fans carried out by the author in the Göttingen Aerodynamic Laboratory within the framework of the preliminary experiments for the new Göttingen wind-tunnel project.

A fan rotor was developed which had very high efficiency at the design point corresponding to moderate pressure rise and which, in addition, could operate at a proportionately high pressure rise. To establish the determining operating factors the author carried out extensive theoretical investigations in Hannover. In this it was necessary to depart from the usual assumption of vanishing radial velocities. The calculations were substantially lightened by the introduction of diagrams. The first part of the report describes the theoretical investigations; the second, the experiments carried out at Göttingen.

SUMMARY

It is customary, in the theoretical treatment of axial turbines, to set all radial velocity components equal to zero. It is found that this assumption makes it impossible to estimate the behavior of the fan over its entire operating range. In particular, no sufficient explanation can be given, on this assumption, for the fact that fan rotors with outwardly increasing blade chord maintain considerably greater throttling than rotors with outwardly decreasing blade chord. For the solution of the problem just outlined, formulas for the calculation of stationary and rotating cascades are derived, which are based on a consideration of small radial velocities. The method of calculation differs from the

*"Untersuchungen über einstufige Axialgebläse." Luftfahrtforschung, vol. 14, no. 7, July 20, 1937, pp. 325-346 and no. 9, Sept. 20, 1937, pp. 458-473.

/

hitherto customary one primarily in that, after the calculation of the individual cascade section characteristics, a throughflow distribution calculation must be undertaken, which correlates definite operating conditions of the individual cascade sections. (See secs. II and III.) The usual cascade corrections are to be applied in the calculation of the section characteristics.

In the present report the Betz method which, in the calculation of cascade corrections, takes account only of the circulation of the neighboring profiles is extended by the introduction of a thickness correction. (See sec. V, 2.) In the determination of the cascade section characteristics, diagrams are introduced which substantially lighten the task of calculation. (See sec. IV.) These diagrams give, in addition, a good survey of the existing possibilities and permit quick estimates to be made, as illustrated by a series of examples. (See sec. VI, 1 and 2.) The throughflow distribution calculation requires the solution of a differential equation, which is reduced to a simple iteration process on the corresponding difference equation. (See sec. VII, 3.)

The throughflow condition allows, for instance, the design of a rotor to change a nonuniform to a uniform energy distribution. (See sec. IV, 3.) Likewise, a simple method can be given for the determination of the blade chord distribution which guarantees constant energy over the whole throughflow cross section, not only for the design operating point but over a wider throttling range. Lastly, the throughflow condition permits a reliable estimate of the stability of the rotor flow to be made.

The comparison of the theoretical calculations for three rotors with the experiments (sec. VII) show that the torque on the rotor shaft can be calculated with greatest certainty. The efficiency can also be predicted with sufficient accuracy if the experimentally determined clearance losses (sec. VIII) are included. Greater uncertainties arise in the calculation of the efficiency of the total blower installation including exit guide vanes and hub diffuser. In this connection the main difficulty may be ascribed to the rather little-known action of the hub diffuser. But for guide vanes there is an additional loss due to secondary flows (sec. V), which cannot yet be included with sufficient accuracy. The secondary flows of the boundary layers at the outside sections in rotors are practically nonexistent, but do exist at the hub and

in a manner equivalent in action to a boundary-layer suction. These facts explain why the $\zeta_{A_{max}}$ of the hub sections may be safely exceeded. Separation of the entire rotor flow sets in only when $\zeta_{A_{max}}$ at the outer sections is exceeded.

On this basis, rotors with outwardly increasing blade chords are suitable for high loadings, especially as the throughflow distribution calculation shows that the axial throughflow velocity in the neighborhood of the outer wall is considerably larger than the average throughflow velocity. For small flows more favorable working conditions for the outer blade parts are automatically produced.

In conclusion, experimental investigations on four rotors with adjustable blades and also experimental investigations on the influence of tip clearance on efficiency and the maximum attainable throttling are given.

It is to be noted that the method of calculation derived for blowers may be applied directly to axial pumps. The application of the method to the calculation of axial turbines should offer no difficulty.

NOTATION

Coordinates:

x coordinate of axial direction, positive in throughflow (free-stream) direction

r distance from blower axis

θ angle between radius vector r and a zero plane passing through blower axis

r_i hub radius

r_a rotor radius

$$R = \frac{r}{r_a}$$

Blade characteristics:

z number of blades

l profile chord

d maximum profile thickness

D mean profile thickness referred to profile chord

$t = \frac{2\pi r}{z}$ cascade spacing at cylindrical section $r =$
constant

$\lambda = \frac{lz}{2\pi r}$ section solidity

$$\lambda' = \lambda \left(1 + \frac{\pi}{6} D \lambda^2 \right)$$

δ profile angle, measured between profile chord and
x-direction

$\delta_1 = 90 - \delta$, angle between profile chord and plane normal
to axis

α angle of attack

Absolute velocities:

c_m axial velocity

c_u tangential velocity

c'_{u_1} tangential velocity directly before cascade

c'_{u_2} tangential velocity directly behind cascade

c_r radial velocity

v_m axial disturbance velocity

v_u tangential disturbance velocity

} produced by
finite blade
thickness

ω angular velocity of rotor

$\varphi = \frac{c_m}{r_a \omega}$ throughflow coefficient

$$\Delta\varphi = \frac{c_{m2} - c_{m1}}{r_a \omega}$$

$$\delta = \frac{rc_u}{r_a^2 \omega}$$

$$\Delta\delta = \frac{r(c'u_2 - c'u_1)}{r_a^2 \omega}$$

Relative velocities:

$$w_m = c_m$$

$$w_r = c_r$$

$$w_u = c_u - r\omega$$

$$w = \sqrt{w_m^2 + w_u^2 + w_r^2}$$

$$\varphi^* = \frac{w_m}{r\omega} = \varphi \frac{r_a}{r}$$

$$\delta^* = \frac{w_u}{r\omega}$$

$$\Delta\delta^* = \frac{w_{u2} - w_{u1}}{r\omega} = \frac{\Delta w_u}{r\omega} = \Delta\delta \left(\frac{r_a}{r}\right)^2$$

The subscripts 1 and 2 denote cross sections far before and far behind the cascade, respectively.

Pressures:

p static pressure

p_g total pressure

$$\psi = \frac{p_{g2} - p_{g1}}{\frac{\rho}{2}(r_a \omega)^2} = \frac{\Delta p_g}{\frac{\rho}{2}(r_a \omega)^2}$$

$$\psi^* = \psi \left(\frac{r_a}{r} \right)^2 = \frac{\Delta p_g}{\frac{\rho}{2} (r\omega)^2}$$

Forces:

A section lift

W section drag

T tangential force

S axial force

$$\zeta_A = \frac{A}{\frac{\rho}{2} w^2 l} \quad \text{lift coefficient}$$

ζ_{Ae} lift coefficient of isolated profile

ζ_{Ag} lift coefficient of profile in cascade

$$\zeta_W = \frac{W}{\frac{\rho}{2} w^2 l} \quad \text{drag coefficient}$$

$$\epsilon = \frac{\zeta_W}{\zeta_A} \quad \text{profile glide angle}$$

$$\zeta_T = \frac{T}{\frac{\rho}{2} w^2 l} \quad \text{tangential force coefficient}$$

$$\zeta_S = \frac{S}{\frac{\rho}{2} w^2 l} \quad \text{axial force coefficient}$$

$$k = \text{cascade effect coefficient defined by } \frac{\partial \zeta_{Ag}}{\partial \alpha} = k \frac{\partial \zeta_{Ae}}{\partial \alpha}$$

$$K = \frac{\lambda' \zeta_T}{\cos \beta}$$

M. torque on rotor shaft

η efficiency

Auxiliary quantities:

β angle between relative stream direction and meridian plane

Γ circulation along a circle $r = \text{constant}$

$\sigma_o = \frac{\bar{\psi}_o^2}{\psi}$ throttling coefficient

$X = \frac{-\varphi^*}{\dot{\psi}_1^*}$

$Y = -\frac{2\Delta\dot{\psi}^*}{\dot{\psi}_1^*} = -\frac{\psi^*}{\eta\dot{\psi}_1^*}$

$X^* = \frac{1}{X} = -\frac{\dot{\psi}_1^*}{\varphi^*}$

$Y^* = \frac{Y}{X} = \frac{2\Delta\dot{\psi}^*}{\varphi^*}$

The subscript o indicates quantities calculated for zero blade thickness; a bar denotes quantities averaged by integration.

I. INTRODUCTION

It is usual, in the theoretical treatment of axial blowers, to set the radial velocity components equal to zero. On this assumption the flow is substantially two dimensional in character: All cylindrical surfaces coaxial with rotor or stator axis are stream surfaces and after development of the cylindrical surfaces the flow can be treated in known manner as plane cascade flow. One significant result is that the axial velocity distribution before and behind the cascade must be the same by continuity.

However, the assumption of vanishing radial velocity component is not fulfilled in general. A simple consideration will illustrate this assertion: Visualize a fan installation consisting of a rotor and a set of exit guide vanes, with the axial entrance velocity as being constant.¹ The same thing is to apply to the energy of the entering fluid. The exit guide vanes are so designed that the fluid leaves in a purely axial direction. The rotor imparts energy to the fluid. If this energy change is constant over the whole cross section, then the fluid energy per unit volume - that is, the total head - is constant not only before but also behind the exit guide vanes.

$$p_g = p + \frac{\rho}{2} c_m^2 \quad (1)$$

The static pressure p must likewise be constant in every plane normal to the axis far before or behind the fan, since any pressure drop within such a plane would cause radial or tangential accelerations of the flow contrary to the assumption of pure axial flow velocity direction in the regions far before or behind the fan installation. It follows from equation (1) that the axial velocity c_m in the exit cross section is constant and by continuity must equal the axial entrance velocity for fixed cross section. In this particular case, then, the condition mentioned at the start is fulfilled, at least in its total effect.

It is different when the energy imparted to the fluid by the rotor is not constant over the whole cross section. If the assumptions for the entrance flow are retained, the energy per unit volume (namely, the total pressure in the exit cross section) is no longer constant. Again assuming that the fluid leaves the exit guide vanes in purely axial direction, the static pressure must, as before, be constant in every cross section behind the fan; and it follows from equation (1) that c_m at exit can no longer be constant. Radial velocity components must

¹This statement refers to the velocity distribution in the throughflow cross section as well as to the time variation of the flow phenomena. In the following only steady operating conditions will be treated.

therefore arise in the flow passing through the fan and these cause a change in the axial velocity distribution.²

If the total pressure and axial velocity of the entrance flow are constant, the blower rotor, in general, is designed so that the energy input for the chosen operating condition is likewise constant over the whole rotor cross section. Under these circumstances the question of whether and when a nonuniform energy yield of the rotor arises is pertinent. To answer this question it is necessary to examine the nature of energy interchange more closely: To this end consider a blade element of radial width dr at distance r from the rotor axis. If the resultant force on the blade element has a component T in the plane normal to the axis (fig. 1), the work $T r \omega$ is done on the element, where ω is its angular velocity about the rotor axis. For simplicity it is assumed that all the work done on the blade element is given up to the fluid without loss. Then energy of the amount $T r \omega$ is given up to the fluid, and for constant axial velocity the requirement of constant energy addition is equivalent to the condition $T = \text{constant}/r$. The resulting force on the blade element for a given section, angular velocity and axial throughflow velocity is a function of the section angle of attack, which is to be chosen in accordance with the assumption made previously for the operating point of the design calculation, so that the condition given for the force component T is fulfilled. If the fan operates at a pressure rise other than that used in the design, the ratio of axial to rotational velocity, and hence the angle of attack, is different for each airfoil element. The condition $T = \text{constant}/r$ is, in general, no longer fulfilled. It may be inferred that, without special precautionary measures, constant energy addition occurs only for a particular operating condition. If other operating conditions are to be considered, the limiting assumption of constant input energy must be relinquished.

²It is sufficient in the preceding considerations to establish the change in axial velocity distribution and the existence of the radial velocities necessarily associated therewith only for the region of the blades. It will be shown later, however, that the radial velocities assume their greatest value there and only decrease toward zero with increasing distance from the blade region.

Similar considerations for adjustable blowers also lead to the result that the condition of constant input energy is no longer fulfilled when the angle of attack of the blower blades is other than that specified by the design.

II. THE SYSTEM OF TRAILING VORTICES BEHIND THE CASCADE

A cylindrical system of coordinates is chosen the x-axis of which coincides with the fan axis. Its positive direction is the flow direction. The distance of a point from the x-axis is as usual denoted by r . The angle θ denotes the angular rotation of the radius vector from a zero direction. The direction of rotation is in the sense of a right-hand screw relation to the x-axis.

The examples considered in the introduction are of a very special nature. To achieve more general results, the appearance of radial velocities may equally be explained from another point of view. The following considerations are entirely analogous to those forming the basis of the well-known vortex theory of airfoils and propellers. (See reference 1.) The blades of a fixed or rotating cascade are considered to be replaced by vortices bound to the respective blade locations. Their vortex strength is equal to the circulation $\Gamma(r)$ around the respective blade element. If $\Gamma(r)$ is constant along the blade span, the circulation at the hub assumes the value $\Gamma = \Gamma_1$ discontinuously and similarly drops discontinuously from $\Gamma = \Gamma_a$ to zero at the outer wall. According to the Helmholtz vortex theorems, the blade root and tip are each the origin of a free (trailing) vortex of strength Γ . For variable circulation along the blade span, a vortex sheet of strength $d\Gamma/dr$ per unit length in the blade trailing edge direction comes trailing off the blade in addition to the vortices Γ_1 and Γ_a . The direction of an element of trailing vortex coincides with that of the velocity relative to a coordinate system fixed to the cascade.

To simplify matters, two assumptions are made: The radial velocities which may arise are small with respect

to the throughflow velocity, so that in the calculation of the induced velocities of the trailing vortices it suffices to consider the trailing vortices as distributed on a right cylinder coaxial with the blower axis. Except for extreme cases, this condition is fulfilled very well for fans where the housing and hub are cylinders extending far upstream and downstream. Secondly, the limiting transition to an infinite number of blades is made. This limiting transition simplifies the flow to the extent that all quantities are thus made to depend only on x and r . This transition is justified because the cascades considered generally have a large number of blades. Elsewhere it will be shown that, under certain assumptions to be formulated later, the formulas derived for an infinite number of blades hold for velocities averaged with respect to the coordinate θ . To make the derivations easily apparent, however, the limiting case of an infinite number of blades will be treated first.

If $z\Gamma(r)$ is the total circulation of the z -blades, the limiting transition is effected so that the amount of the total circulation of every cylindrical section is maintained. The two-dimensionally distributed vortex sheet becomes a system of three-dimensionally distributed trailing vortices the vortex lines of which coincide with the streamlines of the relative flow.

Consider a cylindrical surface coaxial with the rotor. According to the preceding assumptions this is approximately a vortex surface. If each vortex element of such a vortex surface is resolved into a component parallel to the cylinder generating lines and a component along the tangent perpendicular to the generating lines, the trailing vortices of the cylindrical surface may be considered as a system of ring vortices with the diameter of the cylinder, and a system of straight vortices coinciding with the cylinder generating lines. On the assumption that the blade region is of negligible extent in the axial direction, so that the blade space can be contracted to a plane, both vortex systems start from the rotor plane and extend to infinity in the positive direction. The last assertion assumes, of course, that two fans, one behind the other, are sufficiently separated so as not to have any mutual influence. It is evident that the first vortex system induces axial and radial velocities in the rotor plane, the second, tangential velocities.

To calculate the tangential velocities induced in the rotor plane by the system of straight line vortices, it is noted that the velocities induced by a straight line vortex in the plane from which it starts are half as large as those corresponding to an equal vortex extending infinitely in both directions. To compute the velocity in the rotor plane introduced by a straight vortex of radius r' and thickness dr' bounded by the rotor plane, a system of straight vortices extending from both sides to infinity is introduced. These vortices are located on the same cylinder but have only half the vortex strength. The velocity field corresponding to this vortex system is, by symmetry, a function only of r . It follows that all radial velocities of this field must vanish; otherwise fluid would have to originate inside of a cylinder coaxial with a vortex surface. No axial velocities are generated by this straight line vortex system. Hence only the tangential velocities remain to be investigated: If r' denotes the radius of the straight line vortex surface and $dw_u(r, r')$ the tangential velocity at distance r from the axis due to the vortex system, the circulation around a circle of radius r is $2\pi r dw_u(r, r')$. If the circle is inside the vortex surface, the circulation must equal zero, since no vortex is enclosed. But if the circle surrounds the vortex cylinder, the circulation equals the total vortex strength of the cylinder

$$2\pi r' \frac{\gamma(r')}{2} dr', \text{ where } \gamma(r') \text{ is the vortex density of}$$

the straight vortices originating in the rotor plane. Hence the rotational velocity inside the vortex cylinder is

$$dw_u = 0$$

and outside

$$dw_u = \frac{\gamma(r')}{2} \frac{r'}{r} dr'$$

According to the foregoing, the total vortex strength of a cylindrical surface is

$$2\pi r' \frac{\gamma(r')}{2} dr' = \frac{z}{2} \frac{d\Gamma(r')}{dr'} dr'$$

and hence

$$dw_u(r, r') = \frac{z}{4\pi r} \frac{d\Gamma(r')}{dr'} dr' \quad \text{for } r' < r$$

$$dw_u(r, r') = 0 \quad \text{for } r' > r$$

The totality of trailing straight line vortex systems originating in the cascade plane, including the hub and outer vortices, induce in the rotor plane the velocity

$$\begin{aligned} w_u(St) &= \int_{r_i}^{r_a} dw_u(r, r') + \frac{\Gamma_i}{4\pi r} \\ &= \frac{z}{4\pi r} \int_{r_i}^r \frac{d\Gamma(r')}{dr'} dr' + \frac{\Gamma_i}{4\pi r} = \frac{z}{4\pi r} \Gamma(r) \end{aligned}$$

Since the bound vortices add nothing to the tangential velocity in the cascade plane, this tangential velocity component is the sum of the tangential velocity w_{u_1} in front of the cascade and the velocity $w_u(St)$

$$(w_u)_{\text{cascade}} = w_{u_1} + \frac{z}{4\pi r} \Gamma(r) \quad (2)$$

This equation leads to the important conclusion that except for the tangential velocity in front of the cascade the tangential velocity in the cascade plane depends on the circulation corresponding to the radial location under consideration, rather than on the radial distribution of circulation.

As is known, the total blade circulation of a cylindrical section of radius r is the difference in circulation before and behind the cascade. The circulation before and behind the cascade is measured along circles with the radius of the cylindrical section. If w_{u_1} and w_{u_2} denote the mean tangential velocities before and behind the cascade, respectively, then

$$z\Gamma(r) = 2\pi r(w_{u_2} - w_{u_1})$$

which, when substituted into equation (2) gives

$$(w_u)_{\text{cascade}} = w_{u_1} + \frac{1}{2} (w_{u_2} - w_{u_1}) = \frac{1}{2} (w_{u_2} + w_{u_1}) \quad (3)$$

The radial and axial velocities induced in the cascade plane by the trailing vortices are not independent of the circulation distribution. The relation between axial velocity and circulation distribution is discussed elsewhere. However, a proposition to be used later will be derived here. To this end, consider a vortex tube having its origin in the cascade plane and made up of ring vortices of radius r' . Figure 2 shows schematically a ring vortex of this vortex tube. The reflected ring vortex with respect to the cascade plane is shown as a dotted circle.³

This reflected ring vortex would exist if the vortex tube extended to infinity in both directions. The velocities induced in the plane $x = 0$ by such a vortex tube correspond to the velocity field in a plane normal to the axis far behind the cascade. In figure 2 the vortex element ds and the image element ds' are without loss of generality taken to be the top elements of the respective ring vortices. The distances a and a' of these elements from an arbitrary point P in the cascade plane are equal. According to the Biot-Savart law, each vortex element induces velocities dv and dv' at P which are equal in magnitude. Since the induced velocity is at right angles to the vortex element, dv and dv' must lie in that plane at right angles to the cascade plane, a cross section of which is shown in figure 2. It is evident from figure 2 that the dotted ring vortex doubles the axial velocity while causing all other components, in particular the radial component, to vanish. It follows for the vortex tube originating in the cascade plane that the axial velocity it induces in the cascade plane is only half as large as that far behind the cascade and that all induced radial velocities vanish at large distances before and behind the cascade plane. Similarly, it follows from this consideration that

³By reflection hereinafter is meant only the image of the geometric form, the sense of rotation of the vortex element being maintained.

$$(w_m)_{\text{cascade}} = \frac{1}{2} (w_{m_1} + w_{m_2}) \quad (4)$$

$$w_{r_1} = w_{r_2} = 0 \quad (5)$$

where the subscripts 1 and 2 denote regions far before and behind the cascade, respectively.

III. THE THROUGHFLOW CONDITION

1. The Euler Equations for Flow Through a Rotor with Infinite Number of Blades

The relation between the axial throughflow velocity and the circulation distribution can be derived by consideration of the trailing ring vortices emanating from the back of the rotor. It is simpler, however, to derive this relation by direct integration of the Euler equations. The energy losses arising from the flow through the rotor are then easily taken into account by a slight extension of the argument. The fluid medium is taken to be incompressible. This assumption is sufficiently valid for fans the circumferential velocity of which remains less than about 150 meters per second (492 ft/sec). A rotating set of axes is used for the rotor to obtain stationary conditions. The limiting case of an infinite number of rotor blades which is dealt with first represents a simplification, as mentioned previously, because of the rotational symmetry which prevails. The forces exerted by the rotor blades on the fluid do not constitute a surface distribution but may be visualized as impressed volume forces. They are functions only of r and x . Their magnitude is defined by the type of limiting transition of finding a rotor with infinite number of blades to substitute for a given rotor with z -blades. To this end a ring of cross section $dx dr$ is placed through the rotor. (See fig. 3.) This ring cuts out on every blade an element on which the tangential and axial forces per unit area are, respectively, $\partial T/\partial s$ and $\partial S/\partial s$.⁴

⁴Forces T and S and forces A and W which appear later are in agreement with the usual definitions of forces on profile sections, namely, forces per unit length spanwise.

The symbol ds denotes the line element traced on the blade by the dx side of the ring. The radial component of the force on the blade element is negligible inasmuch as the normal to the blade surface is sufficiently exactly perpendicular to the radial direction. The z -blades in the entire ring act on the fluid with the tangential

force $-z \frac{\partial T}{\partial s} ds dr$ and the axial force $-z \frac{\partial S}{\partial s} ds dr$. If β is the angle between ds and dx then

$$ds = \frac{dx}{\cos \beta}$$

and with

$$\frac{1}{\cos \beta} \frac{\partial T}{\partial s} = T' \quad \text{and} \quad \frac{1}{\cos \beta} \frac{\partial S}{\partial s} = S'$$

the axial force becomes

$$-z S' dx dr$$

and the tangential force becomes

$$-z T' dx dr$$

These values are maintained in the limiting transition to an infinite number of blades, so that the forces on the volume element $dx dr \times rd\theta$ are

$$- \frac{z}{2\pi r} S' dx dr \times rd\theta$$

in axial direction and

$$- \frac{z}{2\pi r} T' dx dr \times rd\theta$$

in tangential direction.

The volume forces are, of course, zero outside of the rotor. The Euler equations in cylindrical coordinates are, with due regard to the volume forces previously discussed:

$$\left. \begin{aligned}
 w_m \frac{\partial w_m}{\partial x} + w_r \frac{\partial w_m}{\partial r} + \frac{1}{\rho} \frac{z}{2\pi r} S' &= - \frac{1}{\rho} \frac{\partial p}{\partial x} \\
 w_m \frac{\partial w_r}{\partial x} + w_r \frac{\partial w_r}{\partial r} - \frac{w_u^2}{r} - \omega^2 r - 2\omega w_u &= - \frac{1}{\rho} \frac{\partial p}{\partial r} \\
 w_m \frac{\partial w_u}{\partial x} + w_r \frac{\partial w_u}{\partial r} + \frac{w_r w_u}{r} + 2\omega w_r + \frac{1}{\rho} \frac{z}{2\pi r} T' &= 0
 \end{aligned} \right\} \quad (6)$$

To these is added the equation of continuity written in the form:

$$\frac{\partial}{\partial x} (r w_m) + \frac{\partial}{\partial r} (r w_r) = 0 \quad (7)$$

If the Euler equations are multiplied, respectively, by

$$w_m = \frac{dx}{dt}, \quad w_r = \frac{dr}{dt}, \quad w_u = \frac{d(r\theta)}{dt}$$

and then added, the result is, after multiplication by ρ , and since

$$\frac{\partial}{\partial x} (w_r)^2 = 0$$

$$\frac{DH}{dt} + \frac{z}{2\pi r} (S' w_m + T' w_u) = 0 \quad (8)$$

where

$$\left| H = p + \frac{\rho}{2} \left[w_m^2 + w_r^2 + w_u^2 - (w_r)^2 \right] \right. \quad (9)$$

The operator $\frac{D}{dt}$ is the particle derivative

$$\frac{D}{dt} = w_m \frac{\partial}{\partial x} + w_r \frac{\partial}{\partial r}$$

The quantity in parentheses in equation (8) can be written as

$$w \left(S' \frac{w_m}{w} + T' \frac{w_u}{w} \right)$$

Then

$$\frac{w_m}{w} = \cos(x, w), \quad \frac{w_u}{w} = \cos(\tau, w)$$

where (x, w) and (τ, w) , respectively, denote the angles formed by the axial and tangential velocities with the relative velocity direction. Since the radial component of the force on a blade element has been assumed zero then

$$w(S' \cos(x, w) + T' \cos(\tau, w)) = w W'$$

and

$$W' = \frac{\partial W}{\partial s} \frac{1}{\cos \beta}$$

where $\frac{\partial W}{\partial s}$ is the force component per unit surface on the blade element in the free-stream direction. Equation (8) becomes, with this change,

$$\frac{DH}{dt} + \frac{z}{2\pi r} W' w = 0$$

If W' is known as a function s_0 of the distance along the streamline, then equation (8) can be integrated along the streamline⁵ to give

$$\left| H_2 - H_1 = - \frac{z}{2\pi r} \int_1^2 W' ds \right. \quad (10)$$

where the points 1 and 2 follow consecutively in the stream direction. The integral on the right-hand side is proportional to the work done by the drag along the streamline. For viscosity-free fluid $W' = 0$. In the case of small viscosity, the flow outside of the boundary layer can, as is known, be regarded as frictionless so

⁵ The equation $w = \frac{ds_0}{dt}$ is approximated here by $\frac{ds}{dt}$.

that the previous considerations retain their validity. The integral in equation (10) has a positive value, however, with $H_2 < H_1$. If the drag is set equal to zero, equation (10) becomes, for a fixed coordinate system ($\omega = 0$), the well-known Bernoulli equation.

The integral in equation (10) may be evaluated for cascades with small axial projection. Since W' vanishes outside of the cascades and $\cos \beta$ is approximately constant,

$$\int_1^2 W' ds = \frac{1}{\cos \beta} \int_1^2 \frac{\partial W}{\partial s} ds = \frac{W}{\cos \beta}$$

and hence

$$H_2 - H_1 = - \frac{z}{2\pi r} \frac{W}{\cos \beta} \tag{11}$$

By definition $\frac{\partial W}{\partial s}$ is the drag component per unit surface on a blade of the original z -blade cascade and accordingly $W = \int_1^2 \frac{\partial W}{\partial s} ds$ is the blade profile drag per unit length spanwise.

A further important point can be made from the second Euler equation which can be written as follows:

$$w_m \frac{\partial w_r}{\partial x} + w_r \frac{\partial w_r}{\partial r} - \frac{(w_u + \omega r)^2}{r} = - \frac{1}{\rho} \frac{\partial p}{\partial r}$$

Far upstream and downstream from the rotor, $w_r = 0$ according to equation (5). With $w_u + \omega r = c_u$, the following equation is valid for a cross section at a great distance from the rotor:

$$\left| \frac{c_u^2}{r} = \frac{1}{\rho} \frac{\partial p}{\partial r} \right. \tag{12}$$

The last Euler equation need only be used to derive the throughflow condition outside of the rotor, where

$T' = 0$ and the equation simplifies to the conventional

$$\frac{D}{dt} (r c_u) = 0$$

Integration along any streamline that does not go through the region of the blades yields

$$r c_u = \text{constant} \quad (13)$$

Along every streamline outside of the rotor, therefore, the angular momentum is constant.

2. Derivation of the Throughflow Conditions

for Dissipationless Flow

The first problem involves the derivation of the throughflow conditions for viscosity-free fluid. In this instance the force on a blade is perpendicular to the local stream direction and hence $W' = 0$. If two cross sections far upstream and downstream from the cascade are denoted by subscripts 1 and 2, equation (10) or (11) gives

$$H(r_2, x_2) = H(r_1, x_1)$$

and

$$\frac{\partial H_2}{\partial r_2} \frac{\partial r_2}{\partial r} = \frac{\partial H_1}{\partial r_1} \frac{\partial r_1}{\partial r} \quad (14)$$

where

$$r = \frac{1}{2}(r_1 + r_2)$$

The radii r_1 and r_2 are taken to correspond to one stream surface. Then, r is the radius of the same stream surface in the plane of the rotor. Equation (4) yields, with $\Delta c_m = c_{m_2} - c_{m_1}$, and since $c_m = W_m$:

$$(c_m)_{\text{cascade}} = c_{m_1} + \frac{\Delta c_m}{2}$$

from the definition of a streamline, for example,

$$\int_{r_i}^{r(x)} c_m(r', x) \times 2\pi r' dr' = \text{constant}$$

there follows, assuming that $r_2 - r_1$, $r - r_1$, and Δc_m are small to the first order. (See the developments farther along.)

$$\int_{r_i}^{r_1} c_{m_1} r' dr' \approx \int_{r_i}^{r_2} c_{m_1} r' dr' - (r_2 - r_1) c_{m_1}(r_1) = \int_{r_i}^{r_2} c_{m_2} r' dr'$$

and hence:

$$r_2 - r_1 = \frac{1}{c_{m_1}(r_1)} \int_{r_i}^{r_2} \Delta c_m \times r' dr' \approx \frac{1}{c_{m_1}(r_1)} \int_{r_i}^r \Delta c_m r' dr'$$

Analogously,

$$r - r_1 = \frac{1}{c_{m_1}(r_1)} \int_{r_i}^r \frac{\Delta c_m}{2} r' dr'$$

The last two relations yield directly

$$r - r_1 = \frac{1}{2} (r_2 - r_1)$$

$$r = \frac{1}{2} (r_2 + r_1)$$

Since c_r vanishes at great distances from the cascade, the introduction of absolute velocities leaves:

$$\frac{\partial H}{\partial r} = \frac{\partial p}{\partial r} + \frac{\rho}{2} \frac{\partial}{\partial r} (c_m^2 + c_u^2 - 2r\omega c_u)$$

$\frac{\partial p}{\partial r}$ is replaced by $\rho \frac{c_u^2}{r}$ from equation (12) and after a

simple transformation:

$$\frac{\partial H}{\partial r} = \frac{\rho}{2} \left[\frac{1}{r^2} \frac{\partial}{\partial r} (rc_u)^2 + \frac{\partial}{\partial r} (c_m^2 - 2\omega rc_u) \right]$$

which becomes, from equation (14),

$$\begin{aligned} \frac{\partial}{\partial r} (c_{m1}^2 - c_{m2}^2) = & \frac{1}{r_2^2} \frac{\partial}{\partial r} (rc_u)_2^2 - \frac{1}{r_1^2} \frac{\partial}{\partial r} (rc_u)_1^2 \\ & - 2\omega \frac{\partial}{\partial r} \left[(rc_u)_2 - (rc_u)_1 \right] \quad (15) \end{aligned}$$

Now, as was discussed in the introduction, rotor and guide vanes are generally designed so that $(rc_u)_1$ as well as $(rc_u)_2$ are constant spanwise at the design operating

point. Hence $\frac{\partial}{\partial r} (rc_u)$ will be small for other operating

conditions, except for regions in the neighborhood of the inner and outer walls. In these boundary regions the pre-

vious assumptions are not always valid since $\frac{\partial}{\partial r} (rc_u)$

can assume large values for thick boundary layers. In the neighborhood of the wall, however, it is $r_1 \approx r \approx r_2$ on kinematical grounds. Hence, for these regions, r_1^2 and r_2^2 can be replaced by r^2 in equation (15) without appreciable error. For the median zone

$$\frac{\Delta r}{2} = r - r_1 = \int_{x_1}^0 \frac{c_r}{c_m} dx$$

and a corresponding equation for $(r_2 - r)$ are applicable. The quotient c_r/c_m is small, as was assumed. Moreover, since this quantity drops to zero with increasing distance from the rotor, $\Delta r/2$ is likewise a small quantity. It

is evident from the preceding statements that $\frac{\partial}{\partial r} (rc_u)^2$

is likewise small of the first order in the middle region

so that here also $\frac{1}{r^2} \frac{\partial}{\partial r} (rc_u)^2$ can be replaced by

$\frac{1}{r^2} \frac{\partial}{\partial r} (rc_u)^2$. Thus the throughflow condition for the

whole region reads:

$$\frac{\partial}{\partial r} (c_{m_1}^2 - c_{m_2}^2) = \frac{1}{r^2} \frac{\partial}{\partial r} \left[(rc_u)_2^2 - (rc_{u_1})^2 \right] - 2\omega \frac{\partial}{\partial r} \left[(rc_u)_2 - rc_{u_1} \right] \quad (16)$$

It is readily proved that

$$(rc_u)_2^2 - (rc_u)_1^2 = (rc'_{u_2} - rc'_{u_1})^2 + 2rc'_{u_1}(rc'_{u_2} - rc'_{u_1})$$

where c'_{u_1} and c'_{u_2} are the absolute tangential velocities immediately before and behind the rotor, for which according to equation (13)

$$(rc_u)_1 = rc'_{u_1} \quad \text{and} \quad (rc_u)_2 = rc'_{u_2}$$

The quantity in parentheses on the left-hand side of equation (16) can be approximated by $-2c_{m_1}\Delta c_m$. Equation (16) is divided by $r_a\omega^2$ to obtain the throughflow condition in dimensionless form. Putting

$$\frac{c_{m_1}}{r_a\omega} = \varphi_1, \quad \frac{c_{m_2}}{r_a\omega} = \varphi_2, \quad \varphi_2 - \varphi_1 = \Delta\varphi$$

$$\frac{rc'_{u_1}}{r_a^2\omega} = \delta_1, \quad \frac{rc'_{u_2}}{r_a^2\omega} = \delta_2, \quad \delta_2 - \delta_1 = \Delta\delta$$

and

$$\frac{r}{r_a} = R$$

gives, after a simple calculation, the throughflow condition for rotors

$$\left. \begin{array}{l} \frac{\partial}{\partial R} (\varphi_1^2 - \varphi_2^2) \\ - \frac{\partial}{\partial R} (2\varphi_1 \Delta\varphi) \end{array} \right\} = \frac{1}{R^2} \frac{\partial}{\partial R} \left[\Delta\vartheta (\Delta\vartheta + 2\vartheta_1) \right] - 2 \frac{\partial}{\partial R} \Delta\vartheta \quad (17)$$

For stationary guide vanes $\omega = 0$ in equation (16). Basing all guide vane velocities on the circumferential velocity $r_a\omega$ of the rotor, the throughflow condition for stationary guide vanes is obtained in the same manner as in the foregoing equations at

$$\left. \begin{array}{l} \frac{\partial}{\partial R} (\varphi_1^2 - \varphi_2^2) \\ - \frac{\partial}{\partial R} (2\varphi_1 \Delta\varphi) \end{array} \right\} = \frac{1}{R^2} \frac{\partial}{\partial R} \left[\Delta\vartheta (\Delta\vartheta + 2\vartheta_1) \right] \quad (18)$$

where the subscripts 1 and 2 denote as before cross sections far upstream and downstream from the cascade.

3. The Throughflow Condition including Energy Losses

The energy losses produced in the flow through a cascade have up to now been disregarded. They can be taken into account in a simple manner, however. To this end, the physical significance of H for a rotor is first defined. From equation 9 after introduction of absolute velocities,

$$H = p + \frac{\rho}{2} \left[(c_m^2 + c_r^2 + c_u^2) - 2\omega r c_u \right] = p_g - \rho\omega r c_u$$

The first term on the right-hand side is the well-known energy per unit volume; $\rho r c_u$ is the angular momentum per unit volume. If this angular momentum is visualized as being produced by the rotor, then a torque corresponding to this production of angular momentum acts on the rotor. Accordingly the work that must be expended on the rotor rotating with angular velocity ω to bring the angular momentum per unit volume from zero to the given value is $\omega\rho r c_u$. The difference in H before and behind the

rotor is

$$H_2 - H_1 = (p_{g2} - p_{g1}) - \rho\omega(r_2c_{u2} - r_1c_{u1}) \quad (19)$$

The first parenthetical expression on the right-hand side is the energy gain per unit volume, the second the loss per unit volume of rotor. If the fluid flows without loss from cross section 1 to cross section 2, the energy gain equals this energy loss and $H_1 = H_2$ as assumed in the foregoing section. For a viscous fluid $H_2 < H_1$ according to equation (10) and the statements connected therewith. From equation (19) it is concluded that in this case the expended work per unit volume $\rho\omega(r_2c_{u2} - r_1c_{u1})$ is greater than the useful output $p_{g2} - p_{g1}$. If the efficiency of a rotor element, included between two neighboring stream surfaces is defined as

$$\eta = \frac{p_{g2} - p_{g1}}{\rho\omega(r_2c_{u2} - r_1c_{u1})} = \frac{p_{g2} - p_{g1}}{\rho\omega(rc'_{u2} - rc'_{u1})} \quad (20)$$

equation (19) becomes

$$H_2 - H_1 = (\eta - 1) \rho\omega(rc'_{u2} - rc'_{u1}) \quad (21)$$

For stationary cascades, no external energy is supplied, but there is an energy loss in total pressure; for example,

$$p_{g2} - p_{g1} = \Delta p_g$$

so that

$$H_2 - H_1 = \Delta p_g \quad (22)$$

Equations (21) and (22) yield exactly as before the throughflow condition including energy loss:

For rotors

$$\left. \begin{aligned} & \frac{\partial}{\partial R} (\varphi_1^2 - \varphi_2^2) \\ & - \frac{\partial}{\partial R} (2\varphi_1 \Delta\varphi) \end{aligned} \right\} = \frac{1}{R^2} \frac{\partial}{\partial R} \left[\Delta\psi (\Delta\psi + 2\psi_1) \right] - 2 \frac{\partial}{\partial R} (\eta \Delta\psi) \quad (23)$$

For stators

$$\left. \begin{aligned} \frac{\partial}{\partial R} (\varphi_1^2 - \varphi_2^2) \\ - \frac{\partial}{\partial R} (2\varphi_1 \Delta\varphi) \end{aligned} \right\} = \frac{1}{R^2} \frac{\partial}{\partial R} \left[\Delta\vartheta (\Delta\vartheta + 2\vartheta_1) \right] - \frac{\partial}{\partial R} \left(\frac{\Delta p_g}{\frac{\rho}{2} (r_a \omega)^2} \right) \quad (24)$$

Equations (17) and (18) or (23) and (24) are used later to evaluate φ_2 or $\Delta\varphi$ for given ϑ_1 , $\Delta\vartheta$, φ_1 and known energy loss. The solutions obtained in this manner must satisfy the following conditions

$$\left. \begin{aligned} \int_{r_i}^{r_a} \varphi_1 2\pi r dr &= \int_{r_i}^{r_a} \varphi_2 2\pi r dr \\ \int_{r_i}^{r_a} \Delta\varphi 2\pi r dr &= 0 \end{aligned} \right\} \quad (25)$$

4. The Conversion of the Throughflow Formula to Cascades with a Finite Number of Blades

It remains to be proved that the throughflow condition, derived on the assumption of an infinite number of blades is actually a condition for the mean flow velocities. For this purpose it is only necessary to prove that equations (6) and (7) hold for the mean flow velocities.⁶ Again assuming a frictionless and incompressible

⁶The validity of equations (3), (4), and (5) follows easily by simple integration along a closed circle $r = \text{constant}$ over the velocity components induced on this circle by the trailing vortex surfaces: If the trailing vortex surfaces are continued by their geometric reflections with respect to the cascade plane, the same laws hold for the integral values as for the induced velocities of the ring and straight line vortex system.

fluid medium, the Euler equations read:

$$\left. \begin{aligned} w_m \frac{\partial w_m}{\partial x} + w_r \frac{\partial w_m}{\partial r} + w_u \frac{\partial w_m}{r \partial \theta} &= - \frac{1}{\rho} \frac{\partial p}{\partial x} \\ w_m \frac{\partial w_r}{\partial x} + w_r \frac{\partial w_r}{\partial r} + w_u \frac{\partial w_r}{r \partial \theta} - \frac{w_u^2}{r} - \omega^2 r - 2\omega w_u &= - \frac{1}{\rho} \frac{\partial p}{\partial r} \\ w_m \frac{\partial w_u}{\partial x} + w_r \frac{\partial w_u}{\partial r} + w_u \frac{\partial w_u}{r \partial \theta} + \frac{w_r w_u}{r} + 2\omega w_r &= - \frac{1}{\rho r} \frac{\partial p}{\partial \theta} \end{aligned} \right\} (26)$$

to which is to be added the equation of continuity

$$\frac{\partial}{\partial x} (r w_m) + \frac{\partial}{\partial r} (r w_r) + \frac{\partial}{r \partial \theta} (r w_u) = 0 \quad (27)$$

To arrive at average values with respect to the coordinate θ only one periodic sector needs to be considered: Stream lines originating at the front and rear stagnation point of a blade and extending to infinity upstream and downstream are supposed to form stream surfaces. If the cascade has z -blades, these stagnation point stream surfaces together with the blade surfaces divide the fluid region into z -periodic arcs. Let the blade pressure sides be given by the function

$$\theta = \theta_d(r, x) + \frac{v 2\pi}{z} \quad (v = 0 \text{ to } z - 1)$$

and the blade suction sides by

$$\theta = \theta_s(x, r) + \frac{v 2\pi}{z} \quad (v = 0 \text{ to } z - 1)$$

At the connecting stagnation point stream surfaces

$$\theta_s(r, x) \quad \text{and} \quad \theta_d(r, x)$$

coincide. Here the subscripts s and d merely serve to identify the two sides of the stream surface. Consideration may be limited to the first periodic sector

since the flow phenomena at corresponding points of the periodic sector are the same. This periodic sector or "arc" as it is termed hereafter cuts an arc out of each circle $r = \text{constant}$, which extends from

$$\theta = \theta_d(r, x) \quad \text{to} \quad \theta = \theta_s(r, x) + \frac{2\pi}{z}$$

To integrate, say the first Euler equation over a periodic arc, it is written by means of the equation of continuity in the following form:

$$\frac{\partial}{\partial x} (rw_m^2) + \frac{\partial}{\partial r} (rw_r w_m) + \frac{\partial}{\partial \theta} (rw_u w_m) = - \frac{r}{\rho} \frac{\partial p}{\partial x}$$

and integrating over the periodic arc gives

$$\begin{aligned} & \int_{r\theta_d}^{r(\theta_s + \frac{2\pi}{z})} \frac{\partial}{\partial x} (rw_m^2) d(r\theta) + \int_{r\theta_d}^{r(\theta_s + \frac{2\pi}{z})} \frac{\partial}{\partial r} (rw_r w_m) d(r\theta) \\ & + (rw_u w_m)_s - (rw_u w_m)_d = - \frac{r}{\rho} \int_{r\theta_d}^{r(\theta_s + \frac{2\pi}{z})} \frac{\partial p}{\partial x} d(r\theta) \end{aligned} \quad (28)$$

In addition:

$$\begin{aligned} & \frac{\partial}{\partial x} \int_{r\theta_d}^{r(\theta_s + \frac{2\pi}{z})} rw_m^2 d(r\theta) = \int_{r\theta_d}^{r(\theta_s + \frac{2\pi}{z})} \frac{\partial}{\partial x} (rw_m^2) d(r\theta) \\ & + \left[rw_m^2 \frac{\partial(r\theta)}{\partial x} \right]_s - \left[rw_m^2 \frac{\partial(r\theta)}{\partial x} \right]_d \end{aligned}$$

Corresponding transformations can be made for the other integrals of equation (28) and the equation becomes

$$\begin{aligned}
 & \frac{\partial}{\partial x} \int_{r\theta_d}^{r\left(\theta_s + \frac{2\pi}{z}\right)} r w_m^2 d(r\theta) + \frac{\partial}{\partial r} \int_{r\theta_d}^{r\left(\theta_s + \frac{2\pi}{z}\right)} r w_r w_m d(r\theta) \\
 & + \left[r w_m \left(w_u - w_m \frac{\partial(r\theta)}{\partial x} - w_r \frac{\partial(r\theta)}{\partial r} \right) \right]_s \\
 & - \left[r w_m \left(w_u - w_m \frac{\partial(r\theta)}{\partial x} - w_r \frac{\partial(r\theta)}{\partial r} \right) \right]_d \\
 & = - \frac{r}{\rho} \left[\frac{\partial}{\partial x} \int_{r\theta_d}^{r\left(\theta_s + \frac{2\pi}{z}\right)} p d(r\theta) + \frac{\partial S}{\partial x} \right] \quad (29)
 \end{aligned}$$

with (fig. 4)

$$\frac{\partial S}{\partial x} = p_d \frac{\partial(r\theta_d)}{\partial x} - p_s \frac{d(r\theta_s)}{dx}$$

Since the surface $F_d = r\theta - r\theta_d(x, r) = 0$ is a boundary flow surface, the equation

$$\frac{D(F_d)}{dt} = \left[-w_m \frac{\partial(r\theta_d)}{\partial x} - w_r \frac{\partial(r\theta_d)}{\partial r} + w_u \right]_d = 0$$

must apply. (See Lamb, reference 2, sec. 9.) The same holds for

$$F_s = r\theta - r\theta_s(x, r) = 0$$

Hence the bracketed expressions on the left-hand side of equation (29) vanish, leaving:

$$\begin{aligned}
& \frac{\partial}{\partial x} \int_{r\theta_d}^{r\left(\theta_s + \frac{2\pi}{z}\right)} r w_m^2 d(r\theta) + \frac{\partial}{\partial r} \int_{r\theta_d}^{r\left(\theta_s + \frac{2\pi}{z}\right)} r w_r w_m d(r\theta) + \frac{r}{\rho} \frac{\partial S}{\partial x} \\
& = - \frac{r}{\rho} \frac{\partial}{\partial x} \int_{r\theta_d}^{r\left(\theta_s + \frac{2\pi}{z}\right)} p d(r\theta) \quad (30)
\end{aligned}$$

The mean value of w_m is defined at:

$$\frac{1}{L} \int_{r\theta_d}^{r\left(\theta_s + \frac{2\pi}{z}\right)} w_m d(r\theta) = \bar{w}_m(r, x)$$

where L is the length of the periodic arc. Let $w_m = \bar{w}_m + \Delta w_m$. Assume that Δw_m is small so that its second power is negligible. Corresponding assumptions are made for

$$\Delta w_r = w_r - \bar{w}_r, \quad \Delta w_u = w_u - \bar{w}_u, \quad \Delta p = p - \bar{p}$$

If these expressions for w_m , w_r , and p are substituted into equation (30) and if the terms of at least the second order are neglected:

$$\begin{aligned}
L \bar{w}_m \frac{\partial}{\partial x} \bar{w}_m + L \bar{w}_r \frac{\partial}{\partial r} \bar{w}_m + \frac{\bar{w}_m}{r} \left[\frac{\partial}{\partial x} (L r \bar{w}_m) + \frac{\partial}{\partial r} (L r \bar{w}_r) \right] \\
+ \frac{1}{\rho} \frac{\partial S}{\partial x} = - \frac{1}{\rho} \frac{\partial (L \bar{p})}{\partial x} \quad (31)
\end{aligned}$$

To determine the value of the bracketed expression on the left-hand side the equation of continuity is integrated over the periodic arc and affords exactly as before

$$\begin{aligned}
& r \left(\theta_s + \frac{2\pi}{z} \right) & r \left(\theta_d + \frac{2\pi}{z} \right) \\
\frac{\partial}{\partial x} \int_{r\theta_d}^{r\theta_s + \frac{2\pi}{z}} r w_{md}(r\theta) & + \frac{\partial}{\partial r} \int_{r\theta_d}^{r\theta_s + \frac{2\pi}{z}} r w_{rd}(r\theta) \\
& + r \left[w_u - w_m \frac{\partial(r\theta)}{\partial x} - w_r \frac{\partial(r\theta)}{\partial r} \right]_s \\
& - r \left[w_u - w_m \frac{\partial(r\theta)}{\partial x} - w_r \frac{\partial(r\theta)}{\partial r} \right]_d = 0
\end{aligned}$$

The bracketed expressions vanish again in the same way as before, and from the definition of the mean values the equation of continuity for the mean velocities follows at

$$\frac{\partial}{\partial x} (Lr\bar{w}_m) + \frac{\partial}{\partial r} (Lr\bar{w}_r) = 0 \quad (32)$$

Herewith equation (31) becomes

$$\bar{w}_m \frac{\partial \bar{w}_m}{\partial x} + \bar{w}_r \frac{\partial \bar{w}_m}{\partial r} + \frac{1}{\rho L} \frac{\partial S}{\partial x} = - \frac{1}{\rho L} \frac{\partial (L\bar{p})}{\partial x} \quad (33)$$

If the bars are omitted in equations (32) and (33) and $\frac{1}{L}$ is replaced by the approximation $\frac{z}{2\pi r}$, the equation of continuity (7) and the first of the Euler equations (6) are obtained. The other Euler equations (6) are derived in exactly the same way.

In retracing the derivation of the throughflow condition, it becomes evident that the substitution of $\frac{2\pi r}{z}$ for L is of no importance for the throughflow condition. Hence equations (17) and (18) or (23) and (24) are valid also for the mean velocities by a finite number of blades, provided that the departures from the mean values are small of at least the first order. This condition is fulfilled for frictionless fluids, except in extreme cases. The conditions with regard to losses in fluids with friction are decidedly more unfavorable. The losses become apparent in narrowly bounded dead air regions in the neighborhood of the cascade, so that there

the departure of the local total head from the mean value can no longer be regarded as small. In this case the neglected second order terms can cause an appreciable error.

IV. DIAGRAMS FOR PREDICTING THE CASCADE CHARACTERISTICS

1. Integration of the Third Euler Equation

in the Blade Region

In order to calculate the action of a cascade on a fluid medium at the prescribed initial condition φ_1, ψ_1 , equations (23) and (24) must be supplemented by the relation between $\varphi = \varphi_1 + \frac{\Delta\varphi}{2}$ and $\Delta\psi$. The last Euler equation (6), which so far had been applied only outside of the cascade, is used to find this relation, which, after introduction of absolute velocities reads:

$$c_m \frac{\partial (rc_u)}{\partial x} + c_r \frac{\partial (rc_u)}{\partial r} = - \frac{1}{\rho} \frac{z}{2\pi} T' \quad (34)$$

Let ds_m be the length element along the meridian line of the rotationally symmetrical stream surface of the mean velocity field. With c_{ms} denoting the component of the mean velocity along this meridian line, the fact that the meridian line belongs to a stream surface, results in:

$$c_{ms} : c_m : c_r = ds_m : dx : dr$$

By means of these equations, equation (34) can be expressed in the form

$$c_{ms} \frac{d}{ds_m} (rc_u) = - \frac{r}{\rho} \frac{z}{2\pi r} T'$$

In conjunction with the developments in section III, 4, the periodic arc L is substituted for $\frac{2\pi r}{z}$. At the

same time the velocities must be replaced by the mean velocities, so that:

$$L\bar{c}_{ms} \frac{d}{ds_m} (r\bar{c}_u) ds_m = - \frac{r}{\rho} T' ds_m \quad (35)$$

Now, the axial projection of cascades used in fans is, in general, small; whereas the equation of continuity, equation (32), shows that the change of $L\bar{c}_{ms} = L\bar{w}_{ms}$ in the direction of the meridian line is small of the same order as w_r . Therefore $L\bar{c}_{ms}$ can be replaced by a constant inside the cascade in first approximation. At entrance to the blade region: $L\bar{c}_{ms} = \frac{2\pi r}{z} \bar{c}_{m0}$. The same is true at exit from the blade region and \bar{c}_{m0} is accordingly the mean throughflow velocity for vanishing profile thickness. The quantity $L\bar{c}_{ms}$ in equation (35) can be replaced by $\frac{2\pi r}{z} \bar{c}_{m0}$. A constant average value can similarly be substituted for r and equation (35) integrated with respect to s_m . The result is the conventional momentum equation known from plane cascade theory:

$$-T = \rho \frac{2\pi r}{z} \bar{c}_{m0} \Delta c_u \quad (36)$$

where

$$\Delta c_u = \bar{c}_{u2} - \bar{c}_{u1}$$

and

$$T = \int_1^2 \frac{\partial T}{\partial s} \frac{ds_m}{\cos \beta} = \int_1^2 \frac{\partial T}{\partial s} ds$$

The integral, however, in distinction to plane cascade theory is not evaluated along a cylindrical section coaxial with the cascade but along the mean stream surface. But the first named path of integration can still be chosen, for the same reasons which governed the substitution of a constant mean value for $L\bar{c}_{ms}$. Quantity

$T(r)$, then, is the tangential force per unit length radially, experienced by a profile of the z -blade rotor at the radial location $r = \text{constant}$.

2. Diagram for the Calculation of Section

Characteristics of Rotors

Although the calculation of rotor characteristics on the basis of equation (36) is known it is nevertheless more closely examined, since it is to serve as a basis for several diagrams which substantially simplify the process of calculation. Rotor section is defined as the section of a rotor marked off by two neighboring near stream surfaces.

The characteristic of any rotor section is calculated first as a function of its axial throughflow velocity without regard to the mutual influence of the individual rotor sections. The values of axial throughflow velocity to be correlated to these characteristics are for the present unknown. The correlation is given by the throughflow condition.

Figure 5 is familiar from plane cascade theory and requires no further explanation. It is merely stated that the mean relative velocity denoted by w is identical with that formerly indicated by w_∞ and likewise the angle β between w and the meridian direction coincides with β_∞ . The angle β is always measured from the positive axial direction. Its positive sense is, as usual, counterclockwise so that in conformity with the definitions of the positive directions of w_m and w_u the following equations hold:

$$\cos \beta = \frac{w_m}{w} \quad \sin \beta = - \frac{w_u}{w} \quad (37)$$

To obtain the usual nondimensional force coefficient, equation (36) is divided by $\frac{1}{2} \rho w^2 l$, where w is the mean relative velocity at the location of the profile under consideration in the absence of the profile from the cascade, and l is the profile chord. Upon introduction of the solidity ratio $\lambda = \frac{l}{2\pi r}$, division by

$\frac{1}{2} \rho w^2 l$ and with $w_m = \bar{c}_m$ and $\Delta c_u = \Delta w_u$ equation (36) becomes

$$-\lambda \zeta_T = 2 \frac{w_m}{w} \frac{\bar{c}_{m0}}{\bar{c}_m} \frac{\Delta w_u}{w}$$

The throughflow velocity $w_m = \bar{c}_m$ corresponding to w reduces to \bar{c}_{m0} only for vanishing profile thickness. With

$$\lambda' = \lambda \frac{\bar{c}_m}{\bar{c}_{m0}} \quad \text{and} \quad \frac{w_m}{w} = \cos \beta \quad (38)$$

$$-\frac{\lambda' \zeta_T}{\cos \beta} = 2 \frac{\Delta w_u / rw}{w / rw} \quad (39)$$

For very thin blades $\lambda' \approx \lambda$. For finite blade thickness $\lambda' > \lambda$. The value of $\frac{\bar{c}_m}{\bar{c}_{m0}}$ is calculated elsewhere. Disregarding the influence in quadrature of the radial component

$$\frac{w}{rw} = \sqrt{\left(\frac{w_m}{rw}\right)^2 + \left(\frac{w_u}{rw}\right)^2}$$

where, according to equations (3) and (4) $w_m = \frac{1}{2}(w_{m1} + w_{m2})$ and $w_u = w_{u1} + \Delta w_u / 2$. These formulas also apply to very thin blades only. The corrections necessary for finite blade thickness are likewise given later. Analogously to previous definitions, let

$$\varphi^* = \frac{w_m}{rw}, \quad \vartheta_1^* = \frac{w_{u1}}{rw}, \quad \Delta \vartheta^* = \frac{\Delta w_u^*}{rw}$$

The asterisk indicates that the cited quantities refer to the tangential velocity of the pertinent section rather than to the peripheral velocity and that they are referred to the relative velocities. It is

$$\frac{w}{rw} = |\vartheta_1^*| \sqrt{\left(\frac{\varphi^*}{\vartheta_1^*}\right)^2 + \left(1 + \frac{1}{2} \frac{\Delta\vartheta^*}{\vartheta_1^*}\right)^2} \quad (40)$$

with which equation (39) becomes

$$-\frac{\lambda' \zeta_T}{\cos \beta} = \frac{2 \frac{\Delta\vartheta^*}{|\vartheta_1^*|}}{\sqrt{\left(\frac{\varphi^*}{\vartheta_1^*}\right)^2 + \left(1 + \frac{1}{2} \frac{\Delta\vartheta^*}{\vartheta_1^*}\right)^2}} \quad (41)$$

This equation deduced from the momentum theorem is contrasted with another derived from the disposition of forces on the profile. From figure 6

$$\zeta_T = \mp \zeta_{Ag} \cos \beta - \zeta_W \sin \beta \quad (42)$$

The sign before ζ_{Ag} must be determined by the conditions in the individual case (right- or left-hand wheel rotation, turbine or pump operation). In the following the right-hand pump rotator (fig. 5) is referred to, and hence after introduction of the profile glide angle $\epsilon = \frac{\zeta_W}{\zeta_{Ag}}$

$$\frac{\lambda' \zeta_T}{\cos \beta} = -\lambda' \zeta_{Ag} \left(1 + \frac{\epsilon}{\cot \beta}\right) \quad (43)$$

The quantities ζ_{Ag} and ϵ for a given cascade are functions of the angle of attack α . If δ is the angle of incidence of the blade profile to the axial direction, then $+\alpha = \beta - \delta$. (See fig. 6.) If α is expressed in terms of β in ζ_T , $\lambda' \zeta_T / \cos \beta$ is a function of β alone. In this case $0 \leq \beta \leq \frac{\pi}{2}$; hence $\cot \beta$ can be chosen as independent variable instead of β . From figure 5

$$\cot \beta = -\frac{w_m}{w_u} = -\frac{\frac{w_m}{rw}}{\frac{w_{u1}}{rw} + \frac{1}{2} \frac{\Delta w_u}{rw}}$$

$$\cot \beta = - \frac{\frac{\varphi^*}{\vartheta_1^*}}{1 + \frac{1}{2} \frac{\Delta \vartheta^*}{\vartheta_1^*}} \quad (44)$$

Let

$$\left. \begin{aligned} X &= - \frac{\varphi^*}{\vartheta_1^*} \\ Y &= - \frac{2\Delta\vartheta^*}{\vartheta_1^*} \end{aligned} \right\} \quad (45)$$

It is evident that for pumps and fans Y has only positive values while X can change sign. In particular ϑ_1^* is usually negative for rotors; hence

$$\vartheta_1^* = - |\vartheta_1^*| \quad (46)$$

In a coordinate system with ordinate Y and abscissa X , the curves $\cot \beta = \text{constant}$ are, according to equation (44), the straight lines

$$\cot \beta - \frac{\cot \beta}{4} Y - X = 0 \quad (47)$$

Every straight line of this family goes through the point $X = 0, Y = +4$, and intersects the x-axis in the point $Y = 0, X = \cot \beta$. According to the preceding developments, $\frac{\lambda' \zeta_T}{\cos \beta}$ is a constant, say K , on a straight line of equation (47).

By equation (46) and with due regard to equation (46) this value also may be taken from the curve

$$K = \frac{-Y}{\sqrt{X^2 + \left(1 - \frac{Y}{4}\right)^2}} \quad (48)$$

Since X occurs as a square in equation (48), its sign is immaterial. The family of curves (equation (48)) becomes, by simple transformation,

$$\left(\frac{1 - \frac{K^2}{16}}{K} \right)^2 \left[Y + \frac{K^2}{4 \left(1 - \frac{K^2}{16} \right)} \right]^2 - \left(1 - \frac{K^2}{16} \right) X^2 = 1$$

This equation has the form of a single parametered family of hyperbolas and ellipses referred to their common center, which is on the y-axis at

$$Y = - \frac{K^2}{4 \left(1 - \frac{K^2}{16} \right)}$$

For $K = 0$ there is obtained a straight line, $Y = 0$, for $0 < K < 4$ hyperbolas, and for $4 < K < \infty$ ellipses. For $K = 4$ the equation becomes the parabola

$$X^2 = \frac{1}{2} (Y - 2)$$

Figure 7 illustrates the hyperbolic elliptic family. Since all velocities considered here are relative, diagram I holds for both the stationary and rotating cascades. Admittedly, the range of X and Y in diagram I is sufficient for the majority of practical rotors, but not for stators. In the case of the rotor the initial rotation ϑ_1^* is of the order -1 ; while for a guide vane it becomes very small and may even vanish. Equation (45) shows that X as well as Y can assume very large values in this case. Hence a different diagram is given for guide vanes, which avoids these difficulties, as will be explained elsewhere. In the following paragraph it is assumed that diagram I applies chiefly to rotors.

To find an operating point for a given rotor from diagram I, the solidity λ or λ' , the angle of incidence δ , and the tangential force coefficient, $\zeta_T(\alpha)$ must be known. These data give $K = \frac{\lambda' \zeta_T}{\cos \beta}$ as a function of β according to equation (42). For $K = K_0$ belonging to the straight line for $\beta = \beta_0$ and the corresponding member of the elliptic-hyperbolic family, the point of intersection is the operating point. The straight line $\beta = \beta_0$, which passes through $X = 0, Y = 4$ and $X = \cot \beta_0, Y = 0$ need not be indicated in the diagram. It is sufficient to fix the point of intersection by means of a straightedge..

With this point the corresponding relative or absolute tangential component of the exit velocity is readily obtained. It is:

$$w_{u_2} = w_{u_1} + \Delta w_u$$

and after division by rw and according to the definitions of equation (45)

$$\frac{w_{u_2}}{rw} = \phi_1^* \left(1 + \frac{\Delta \phi^*}{\phi_1^*} \right) = \phi_1^* \left(1 - \frac{Y}{2} \right)$$

$$\left| \frac{c_{u_2}}{rw} = \phi_1^* \left(1 - \frac{Y}{2} \right) + 1 \right. \quad (49)$$

The value of $1 - \frac{Y}{2}$ is read off directly from diagram I.

3. Diagram for Calculation of

Rotor Section Efficiencies

To obtain the energy given off on the fluid by the rotor from the X-, Y-diagram, recourse is had to equation (20). This equation can be written in the following form:

$$2 \frac{c'_{u_2} - c'_{u_1}}{rw} = \frac{p_{2g} - p_{1g}}{\eta \frac{\rho}{2} (rw)^2}$$

Putting in this equation yields

$$\frac{p_{2g} - p_{1g}}{\frac{\rho}{2} (rw)^2} = \psi^*$$

and, as formerly

$$\frac{c'_{u_2} - c'_{u_1}}{rw} = \frac{w'_{u_2} - w'_{u_1}}{rw} = \Delta \phi^*$$

then

$$2\Delta \phi^* = \frac{\psi^*}{\eta}$$

or by equation (45)

$$\left| \frac{\psi^*}{\eta} = - \delta_1^* Y \right. \quad (50)$$

To calculate the pressure coefficient ψ^* , both the initial rotation δ_1^* and the cascade efficiency η must be fixed. From equations (19) and (11)

$$p_{g_2} - p_{g_1} = \rho w (rc' u_2 - rc' u_1) - \frac{z}{2\pi r} \frac{W}{\cos \beta}$$

whence, after substitution in equation (20) and several transformations,

$$\eta = 1 - \frac{\lambda \zeta_W}{\cos \beta} \frac{\left(\frac{w}{rw}\right)^2}{2 \left(\frac{\Delta w u}{rw}\right)}$$

Lastly, by equation (39) with,

$$\eta = 1 + \frac{\zeta_W}{\zeta_T} \frac{w}{rw}$$

To take the finite profile thickness into account, the second term of the right-hand side is multiplied by

$\frac{l}{L} \frac{1}{\lambda'}$, where \bar{L} is the average length between blades along the periodic arc.

The value of ζ_T is given by equation (42). Again preferring a right-hand rotation fan rotor and choosing the previous sign before ζ_{Ag} , the insertion of the glide angle $\epsilon = \frac{\zeta_W}{\zeta_A}$ then results in

$$\frac{\zeta_T}{\zeta_W} = - \left[\frac{\cos \beta}{\epsilon} + \sin \beta \right]$$

which, upon substitution of equation (37), becomes

$$\frac{\zeta_T}{\zeta_W} = -\frac{1}{\epsilon} \left(\frac{w_m}{r\omega} - \epsilon \frac{w_{u1} + \frac{\Delta w_u}{2}}{r\omega} \right) \frac{r\omega}{w}$$

and by equations (40) and (45),

$$\eta = 1 + \epsilon \frac{\psi_1^* \left[X^2 + \left(1 - \frac{Y}{4} \right)^2 \right]}{X + \epsilon \left(1 - \frac{Y}{4} \right)}$$

To calculate this expression easily with the aid of a diagram, it is written in the following form:

$$\eta = 1 + \frac{\psi_1^*}{\frac{1}{\epsilon} f_1 + f_2} \tag{51}$$

where

$$f_1 = \frac{X}{X^2 + \left(1 - \frac{Y}{4} \right)^2}$$

and

$$f_2 = \frac{1 - \frac{Y}{4}}{X^2 + \left(1 - \frac{Y}{4} \right)^2}$$

It is easily verified that in an X-, Y-coordinate system the ordinate scale (Y) of which is four times as small as the abscissa scale (X), the curves $f_1 = \text{constant}$ are circles of radius $r = \frac{1}{2f_1}$ and center $X = r, Y = 4$, and r is measured along the x-axis. Likewise, the curves $f_2 = \text{constant}$ are circles of radii $r = \frac{1}{2f_2}$ and center $X = 0, Y = 4 - r$. These circles can be used for convenient calculation of the curves $f_1 = \text{constant}, f_2 = \text{constant}$. If the ordinate scale is the same as the abscissa scale, the ellipse diagram II (fig. 8) is obtained.

The ellipses $f_1 = \text{constant}$ are the solid curves and $f_2 = \text{constant}$, the dashed ones. This diagram enables easy calculation of the efficiency corresponding to any operating point X, Y according to equation (51).

4. Diagram for Calculating the Section Characteristics of Stationary Guide Vanes

The absolute value of β_1^* for stationary guide vanes is, in general, small. Consequently X and Y become so large that diagram I becomes useless. To obtain a useful diagram for this case also, it should be noted that only the hyperbolas of the ellipse-hyperbola family of diagram I are used. For large values of X the hyperbolas may be approximated by their asymptotes. The slope of these asymptotes to the x -axis is specified by line Y/X . This consideration suggests the introduction of the following coordinate system: $Y^* = Y/X$ as ordinate and $X^* = 1/X$ as abscissa. For this purpose equations (41) and (44) are written in the form:

$$K = \pm \frac{Y^*}{\sqrt{1 + \left(X^* - \frac{1}{4} Y^*\right)^2}} \quad (52)$$

$$\tan \beta = X^* - \frac{1}{4} Y^* \quad (53)$$

The sign in equation (52) does not enter when the equation is squared to obtain the family of curves. Hence it is sufficient to use $|K|$ in the application of diagram III; Y^* is normally negative for right-hand rotation of fans using either entrance or exit guide vanes; while X^* is zero or negative.

The curves of equation (52) are plotted in an X^* -, Y^* -coordinate system in figure 9, diagram III. In this coordinate system the straight lines of equation (53) have the same slope for all β .

$$\frac{Y^* - Y_0^*}{X^* - X_0^*} = 4 \quad (54)$$

They intersect the x-axis in the point $X^* = \tan \beta$.

To determine an operating point for a given cascade from diagram III, λ' , δ , and $\xi_T(\alpha)$ must be known, exactly as for rotors. With these data $K = \frac{\lambda' \xi_T}{\cos \beta}$ is then a known function of β . For $\beta = \beta_0$, let $K = K_0$. The corresponding operating point lies on a straight line of equation (53), for which $\tan \beta = \tan \beta_0$, and on a curve of equation (52) corresponding to the parameter $K = K_0$. To specify the point of intersection, it is not necessary to draw in the straight lines of equation (53). Simply place a straightedge at the slope of equation (54) through the point $Y^* = 0$, $X^* = \tan \beta_0$.

Since the relative velocity equals the absolute velocity for stationary guide vanes,

$$c_{u2} = w_{u1} + \Delta w_u \quad (55)$$

and after division by rw while allowing for equation (45)

$$\begin{aligned} \frac{c_{u2}}{rw} &= \vartheta_1^* \left(1 - \frac{Y}{2} \right) \\ &= \vartheta_1^* \left(1 - \frac{1}{2} \frac{Y^*}{X^*} \right) \end{aligned} \quad (56)$$

This formula is applicable only when $\vartheta_1^* \neq 0$, hence mainly for exit guide vanes. These have the task of changing the rotational kinetic energy behind the rotor to pressure. If the change is complete, $c_{u2} = 0$ and from equation (56)

$$2X^* = Y^*$$

The straight line given by this equation is shown dashed in diagram III. If the rotation ϑ_1^* is only partly removed, then

$$2X^* > Y^*$$

This inequality defines the region below the dashed curve in diagram III. Correspondingly it is true for the

region above the dotted line that the tangential momentum imparted to the fluid by the cascade is too large, and consequently produces a rotation opposite to the inlet rotation. The parenthetical expression of equation (56) gives the remaining, or counterrotation, in fractions of δ_1^* . It is

$$f_3 = 1 - \frac{1}{2} \frac{Y^*}{X^*}$$

which may be written

$$2(1 - f_3) X^* = Y^* \quad (57)$$

In this equation X^*, Y^* indicates the operating point to be found. But if X^* and Y^* are considered as varying coordinates, equation (57) represents a straight line passing through the origin of diagram III and the particular operating point. For $X^* = 0.5$ equation (57) gives

$$1 - Y^*(0.5) = f_3$$

This equation shows that

$$f_3 = \frac{1}{\delta_1^*} \frac{c_{u_2}}{rw} \quad (58)$$

can be read directly from the line $X^* = 0.5$ if the origin is connected to the operating point with a straight-edge and its intersection with the line $X^* = 0.5$ is read off on the scale given in diagram III.

If δ_1^* is small or equal to zero, it is practical to replace equation (58) by another formula. After division by rw , equation (55) may be written in the following form:

$$\begin{aligned} \frac{c_{u_2}}{rw} &= \delta_1^* + \frac{\varphi^* \Delta \delta^*}{\varphi^*} \\ &= \delta_1^* + \frac{\varphi^*}{2} Y^* \end{aligned} \quad (59)$$

Formula (59) holds in general, but in practice, is somewhat more inconvenient than equation (58).

5. Diagram for the Calculation of Energy

Losses in Stationary Guide Vanes

Since the stator does not impart energy to the fluid medium, it is expedient for the present purpose to calculate the energy losses of the flow through the guide vanes direct rather than in the form of an efficiency. According to equations (22) and (11)

$$\Delta\psi^* = \frac{\Delta p_g}{\frac{\rho}{2} (rw)^2} = - \frac{\lambda \zeta_w}{\cos \beta} \left(\frac{w}{rw} \right)^2$$

With $\cos \beta = \frac{w_m}{w}$ and equations (40) and (45), a short calculation gives

$$|\Delta\psi^*| = - \lambda \zeta_w (\varphi^*)^2 f_4 \tag{60}$$

where

$$f_4 = \left[1 + \left(X^* - \frac{Y^*}{4} \right)^2 \right]^{3/2}$$

The curves $f_4 = \text{constant}$ are straight lines in the X^* -, Y^* -coordinates:

$$\sqrt{(f_4)^{2/3} - 1} = X^* - \frac{Y^*}{4}$$

They are plotted in diagram IV of figure 10. Corresponding to any operating point X^*, Y^* , a value f_4 can be obtained by interpolation. Since by equation (45)

$\varphi^* = - \frac{\delta_1^*}{X^*}$, the energy loss for a known $\lambda \zeta_w$ is easily obtained from equation (60).

The finite blade thickness may be taken into account by using $\frac{l}{L}$ instead of λ in equation (60). Moreover,

the velocity corrections given in the next section are to be applied. It may be remarked in conclusion that diagrams I and III overlap in their regions of application. It is therefore possible to use diagram III for the

calculation of unusual rotors and diagram I for the calculation of extreme stators. The same holds for diagrams II and IV.

V. NOTE ON THE CONVERSION OF ISOLATED WING POLARS TO CASCADE POLARS

1. The Corrections Due to Blade Circulation

In the foregoing division the calculation of a cascade was based on the profile coefficient

$$\frac{\zeta_T}{\cos \beta} = - \zeta_{Ag} \left(1 + \frac{\epsilon}{\cot \beta} \right)$$

that is, on the lift coefficient and the glide angle of the profile in cascade. The lift coefficient may be obtained from theoretical calculations, which, however, furnish no information as to the glide angle ϵ or the maximum lift coefficient $(\zeta_A)_{\max}$. It is therefore necessary to resort to experimental data. Cascade measurements would naturally be most suitable. Unfortunately, measurements are so few that experiments on isolated blades must be resorted to. These can only be applied directly, however, when the ratio of cascade spacing to blade chord is so large that the mutual interference of the cascade profiles can be neglected. This simple condition does not exist in many practical cases, and so the isolated wing polars must be converted to cascade polars in a suitable manner.

The problem of applying research data for isolated wings to profiles in cascade arrangement frequently has been treated. It essentially involves the following: Every profile of a cascade finds itself in a disturbance field of the other profiles, which are called neighboring profiles. This field of disturbance exists at the location of the particular profile consideration by visualizing the latter as being removed from the cascade. The presence of the neighboring profiles induces a change in the stream velocity as well as a curvature of the streamlines at the place of the omitted profile. With regard to the omitted profile these streamlines are called the "undisturbed" streamlines of the cascade. The omitted

profile, when placed back in this curved flow, naturally is subjected to different forces from those in the corresponding straight line streamline field. If the angle of attack of the cascade profile is measured from the mean stream direction, as defined previously, it is seen that the linear relation between lift coefficient and angle of attack is maintained. The lift for zero angle of attack is altered, however, as is the slope $\frac{d\zeta_A}{d\alpha}$, which is with the usual terminology,

$$\frac{d\zeta_{Ag}}{d\alpha} = k \frac{d\zeta_{Ae}}{d\alpha}$$

There are two methods by which the lift coefficient of an isolated wing can be converted to that of a profile in cascade: namely, accept the isolated profile without form change and calculate the corresponding cascade coefficients, or fit the profile shape to the "undisturbed" flow in such a manner that the coefficients remain unchanged. The latter procedure is more suitable for the application of data obtained for isolated airfoils. This is especially true when the flow becomes more highly curved due to the proportionately higher blade solidity. Practically any normal airfoil has negative curvature relative to such a flow, and hence exhibits a very unfavorable form.

The adaptation of the individual airfoil to the cascade flow is relatively simple by the procedure given by Betz. (See reference 3.) If the airfoil is curved by this procedure, the lift coefficient of the profile in cascade is approximately equal to that of the isolated profile for the angle of attack α_j on which the calculation was based. For other angles of attack the lift coefficient is given by

$$\zeta_{Ag}(\alpha) = \zeta_{Ae}(\alpha_j) + k \frac{d\zeta_{Ae}}{d\alpha} (\alpha - \alpha_j) \quad (61)$$

and $\epsilon = \epsilon(\zeta_A)$. The factor k is a function of the solidity $\lambda = \frac{z\ell}{2\pi r}$ and that mean stream direction β_0 for which the lift of the profile in cascade vanishes;

k is given in diagrammatic form by Weinig. (See reference 4, p. 40.) But since β_0 is, for the present, unknown, an approximate value must be assumed for it. In this instance, it is expedient to use the value $\beta_0^{(1)}$ = $\alpha_{0e} + \delta$ where α_{0e} is the zero lift angle of the isolated airfoil. The value of k found from the k -diagram with this approximation is used to calculate the angle of attack $\alpha_0^{(1)}$ for which $\xi_{Ag}^{(1)} = 0$ in equation (61). The equation $\beta_0^{(2)} = \alpha_0^{(1)} + \delta$ is a second approximation, and the calculation can then be repeated. It is seen that two approximations generally are sufficient for the determination of k .

2. The Corrections for Finite Profile Thickness

The Betz procedure takes account only of the blade profile circulation distribution, which, as for an isolated airfoil, is determined by the profile mean line. The results accordingly are applicable only to very thin profiles. In practice, however, it frequently happens that the profile thickness in high solidity cascades is no longer negligible. To take this into account, the profile mean line is visualized as being inflated by a source distribution. For this purpose the profile ordinates are measured from the profile mean line, and the length s along the mean line measured from the leading edge is chosen as abscissa. Let $y_S(s)$ and $y_D(s)$ be the ordinates of the suction and pressure sides. The sources distributed on the profile mean line introduce equal and opposite normal velocities v_n on both sides of the mean line. The magnitude of the normal velocity follows from the kinematic boundary condition on suction and pressure sides:

$$\frac{d}{ds} y_S = - \frac{d}{ds} y_D = \frac{v_n}{w}$$

or

$$\frac{v_n}{w} = \frac{1}{2} \frac{d}{ds} (y_S - y_D)$$

For w the constant average velocity can be used (by way of a first approximation), which prevails in the position

of the profile under consideration when the latter is visualized as being omitted from the cascade. Surrounding the element ds with a control line affords

$$2v_n ds = q(s) ds$$

where $q(s)$ is the density of source strength, and finally

$$q(s) = w \frac{d}{ds} (y_S - y_D) \quad (62)$$

The neighboring blades can be replaced by this superposition of sources and circulation of Betz. It can be shown that the disturbances introduced by the sources are smaller than the vortex disturbances. For this reason, it is sufficient to assume the source distribution along the straight profile chord and to calculate the disturbance velocities arising therefrom at the profile chord location of the omitted profile. If the origin of the coordinates is fixed at the leading edge of the omitted profile, the coordinates of a source element are (fig. 11)

$$x' = s' \cos \delta, \quad \tau' = vt - s' \sin \delta \quad (63)$$

where $t = \frac{2\pi r}{z}$, and $-\infty < v \leq -1$, $1 < v \leq \infty$. The coordinates of a starting point on the omitted profile chord are

$$x = s \cos \delta, \quad \tau = -s \sin \delta \quad (64)$$

If $a^2 = (x' - x)^2 + (\tau' - \tau)^2$ the potential of a source element at the point x', τ' is

$$d\Phi = \frac{q(s') ds'}{2\pi} \ln a$$

The disturbance velocities of the source element are given by differentiation with respect to x and τ , respectively:

$$\left. \begin{aligned} dv_m &= \frac{\partial}{\partial x} (d\Phi) = - \frac{q(s') ds'}{2\pi} \frac{x' - x}{a^2} \\ dv_u &= \frac{\partial}{\partial \tau} (d\Phi) = - \frac{q(s') ds'}{2\pi} \frac{\tau' - \tau}{a^2} \end{aligned} \right\} \quad (65)$$

It is assumed for simplicity that $s' - s$ is small compared to vt . Then approximately

$$a^2 = (vt)^2 \left(1 - 2 \frac{s' - s}{vt} \sin \delta \right)$$

With equations (63) and (64), equation (65) becomes, after neglecting terms of second and higher powers of

$$\left(\frac{s' - s}{vt} \right),$$

$$dv_m = - \frac{q(s') ds'}{2\pi(vt)^2} (s' - s) \cos \delta$$

$$dv_u = - \frac{q(s') ds'}{2\pi(vt)^2} (vt + (s' - s) \sin \delta)$$

The disturbance velocity at the point x, T is obtained by integration and summation over the source elements of all the neighboring profiles. Since the integral along

the entire chord $\int_0^l q(s') ds'$ must vanish on grounds of

continuity, it simplifies to

$$v_m = - \frac{\cos \delta}{\pi t^2} \sum_{v=1}^{\infty} \frac{1}{v^2} \int_0^l q(s') s' ds'$$

$$v_u = - \frac{\sin \delta}{\pi t^2} \sum_{v=1}^{\infty} \frac{1}{v^2} \int_0^l q(s') s' ds'$$

Substituting the approximate expression, equation (62), for $q(s)$ and integrating by parts results in

$$\int_0^l q(s') s' ds' = -w \int_0^l (y_S - y_D) ds' = -wF$$

where F is the profile section area. Let $F = Dl^2$; then it is plain that D is the ratio of the mean profile thickness to the profile chord. With

$$\sum_{v=1}^{\infty} \frac{1}{v^2} = \frac{\pi^2}{6}$$

finally,

$$\left. \begin{aligned} v_m &= w \cos \delta \frac{\pi}{6} D \lambda^2 \\ v_u &= w \sin \delta \frac{\pi}{6} D \lambda^2 \end{aligned} \right\} \quad (66)$$

Since the quantity $\frac{\pi}{6} D \lambda^2$ is normally small, equations

(66) represent small velocity corrections. To include them, it is sufficient to change the mean velocity (mean of entrance and exit velocity) at the omitted profile location by the corrections given previously. Moreover, $\delta = \beta - \alpha$. Since α is usually small, δ can be replaced by β in equation (66).⁷ It is evident from the diagrams that

$$w \cos \delta \sim w \cos \beta = w_m$$

$$-w \sin \delta \sim -w \sin \beta = w_u$$

and, after introduction of the dimensionless coefficients,

$$\left. \begin{aligned} \frac{v_m}{rw} &= \varphi_0^* \frac{\pi}{6} D \lambda^2 \\ \frac{v_u}{rw} &= - \left(\vartheta_0^* + \frac{\Delta \vartheta_0^*}{2} \right) \frac{\pi}{6} D \lambda^2 \end{aligned} \right\} \quad (67)$$

The subscript 0 for φ^* , ϑ_1^* , and $\Delta \vartheta^*$ indicates that these quantities refer to the uncorrected velocities corresponding to infinitely thin blades. For rotors and

⁷The substitution of β for δ is equivalent to the assumption that the sources and sinks lie on the "undisturbed" cascade streamline defined in section V, 1.

stationary guide vanes with entrance rotation other than zero, the last equation because of equation (45), can be written in the form

$$\frac{v_u}{rw} = - \delta_0^* \left(1 - \frac{\gamma_0}{4} \right) \frac{\pi}{6} D \lambda^2$$

This formula is impractical for cascades with small δ_0^* . This applies in particular to guide vanes according to section IV, 4. To obtain a useful formula for this case, also the second of equation (67) is rewritten in the form:

$$\begin{aligned} \frac{v_u}{rw} &= - \left(\delta_0^* + \varphi_0^* \frac{\Delta \delta_0^*}{2\varphi_0^*} \right) \frac{\pi}{6} D \lambda^2 \\ &= - \left(\delta_0^* + \frac{\varphi_0^*}{4} \gamma_0^* \right) \frac{\pi}{6} D \lambda^2 \end{aligned}$$

It is plain from equation (66) and figures 12 and 13 that the direction of the disturbance velocity arising from the finite profile thickness is in the image direction to the profile chord along the x-axis. Therefore, besides the increase in throughflow velocity, there is a reduction in angle of attack in retarded flow (pump cascade, fig. 12), and an increase in angle of attack in accelerated flow (turbine cascade, fig. 13). These facts in most cases might be the cause of the apparent discrepancies in the experimental check of the theoretical conversion formulas for the lift coefficient.

To use the diagrams given in section IV, the corrections for the throughflow velocity and for the initial rotation are added, whence

$$\left. \begin{aligned} \varphi^* &= \varphi_0^* \left(1 + \frac{\pi}{6} D \lambda^2 \right) \\ \delta_1^* &= \delta_0^* \left[1 - \left(1 - \frac{\gamma_0}{4} \right) \frac{\pi}{6} D \lambda^2 \right] \end{aligned} \right\} \quad (68)$$

or

$$\delta_1^* = \delta_0^* \left(1 - \frac{\pi}{6} D \lambda^2 \right) - \frac{\varphi_0^*}{4} \gamma_0^* \frac{\pi}{6} D \lambda^2$$

entering these values in formulas (45), while neglecting

second and higher powers of $\frac{\pi}{6} D \lambda^2$, gives

$$\left. \begin{aligned} \text{or} \quad & X = X_0 \left[1 + \left(2 - \frac{Y_0}{4} \right) \frac{\pi}{6} D \lambda^2 \right] \\ \text{and} \quad & X^* = X_0^* \left(1 - \frac{\pi}{3} D \lambda^2 \right) - Y_0^* \frac{\pi}{24} D \lambda^2 \\ & Y = \frac{Y_0}{1 - \left(1 - \frac{Y_0}{4} \right) \frac{\pi}{6} D \lambda^2} \\ & Y^* = \frac{Y_0^*}{1 + \frac{\pi}{6} D \lambda^2} \end{aligned} \right\} \quad (69)$$

In addition

$$\frac{\bar{c}_m}{c_{m_0}} = \frac{\varphi^*}{\varphi_0^*} = 1 + \frac{\pi}{6} D \lambda^2$$

and according to equation (38)

$$\left| \lambda' = \lambda \left(1 + \frac{\pi}{6} D \lambda^2 \right) \right. \quad (70)$$

The tangential exit velocity is calculated with equation (49), (56), or (59) according to equation (68) or (69), respectively. However, since the tangential velocity contribution due to the finite blade thickness decreases rapidly outside of the cascade, this contribution must be subtracted from the calculated value thus giving, for instance, instead of equation (49)

$$\left. \begin{aligned} \frac{c_{u_2}}{rw} &= \vartheta_1^* \left(1 - \frac{Y}{2} \right) + 1 - \frac{v_u}{rw} \\ &= \vartheta_0^* \left[1 - \left(1 - \frac{Y_0}{4} \right) \frac{\pi}{6} D \lambda^2 \right] \left(1 - \frac{Y}{2} \right) \\ &\quad + 1 + \vartheta_0^* \left(1 - \frac{Y_0}{4} \right) \frac{\pi}{6} D \lambda^2 \\ &= \vartheta_0^* \left(1 - \frac{Y_0}{2} \right) + 1 \end{aligned} \right\} \quad (71)$$

Similarly, instead of equations (56) and (59),

$$\frac{c_{u_2}}{rw} = \delta_0^* \cdot f_0^* \quad (72)$$

$$\frac{c_{u_2}}{rw} = \delta_0^* + \frac{\varphi_0^*}{2} \gamma_0^* \quad (73)$$

3. General Remarks on the Applicability of Measurements on Isolated Profiles to Profiles in Cascade

The discussion of the applicability of isolated airfoil polars to cascade calculations is concluded with the observation that according to the experimental investigations by Christiani (reference 5) the glide angles for pump cascades are slightly higher and those for turbine cascades slightly smaller than those for isolated profiles. There is no influence practically on the $C_{A_{max}}$ values for the case in question, for example, pump cascades. In contrast, the dependence on Reynolds number is no longer negligible according to the measurements made by O. Walchner on the Göttingen 622-25 profiles (reference 6). The operation of the thicker hub profile at a Reynolds number based on profile chord below about 0.8×10^5 to 1×10^5 particularly should be avoided. The measurements of F. Gutsche (reference 7) show that the characteristics of the flow about the profile change very unfavorably below this critical Reynolds number; The profile drag increases considerably and separation of flow occurs at a much smaller angle of attack than above the critical Reynolds number.

Another important fact is pointed out: In the experimental investigations on profiles in cascade for which a plane flow between two parallel walls is used, secondary flows arise, which are well known from curved flow investigations. They are due to the fact that the stream velocity in the neighborhood of the wall is smaller than at midchannel, and the positive and negative pressures are correspondingly lower at the blade tips. The situation is schematically shown in figure 14. There is a pressure drop in the direction of the arrows. This pressure drop deflects the boundary-layer flow resulting

in the mentioned secondary flow. Conditions should be similar for stationary guide vanes. It is different, however, for rotors: It appears that the superposed tangential velocity of the profile section causes, on the one hand, a much smaller drop in velocity toward the (outer) wall, especially when the characteristic φ^* is small, and, on the other hand, a simultaneous change in angle of attack. In addition to this, there is the centrifugal deflection of the boundary layer about which little is known, however. All these phenomena act together in such a manner that for the rotors described later the circulating flows of the previously described type were in no case observed in the neighborhood of the outer wall, but were very strongly evident in the neighborhood of the hub. To make the boundary layer flow visible, a blade was covered with the sensitized paper "Ozalid." By means of a bent (clamped) tube about 3 millimeters in diameter a thin ammonia stream with the local velocity could be introduced into the flow before the rotor. The trace of the ammonia-air mixture on the Ozalid covered blade was dyed blue. Figure 15 shows the resulting streamline picture. The deflection of the flow on the suction side is clearly perceived. Although these stream pictures provide some qualitative insight into the progress of the secondary flow through the rotor, these phenomena still need further exploration before the secondary flows observed in stationary cascades and in rotors can be correlated. These secondary flows can influence considerably the pressure changes at high blade loadings. But on the basis of the foregoing remarks the conversion of pressure measurements on cascades to rotors must be regarded, for the present, as very uncertain.

VI. APPRAISAL AND DISCUSSION OF CHARACTERISTIC CASES

1. General Conclusions for Rotors

Subsequent to the foregoing discussion of the principal data for the blower calculations, it is appropriate to present several appraisals and in conjunction discuss some typical cases of blower construction. The effect of the thickness correction is illustrated on a worked out problem. For the cases considered here $\lambda' = \lambda$. Since the glide angle ϵ is small relative to unity at normal angles of attack, equation (43) can be approximated to

$$K = \lambda \zeta_{Ag} \quad (74)$$

Small values of $\cot \beta$ are naturally ruled out. This formula and diagrams I and III afford a convenient survey of the existing possibilities. By reason of

$$\psi^* = \psi \left(\frac{r_a}{r} \right)^2 \quad \text{and} \quad \varphi^* = \varphi \left(\frac{r_a}{r} \right)$$

equations (50) and (45) give for a rotor

$$\left. \begin{aligned} Y &= \frac{-\psi}{\eta \delta_1^*} \left(\frac{r_a}{r} \right)^2 \\ X &= \frac{-\varphi}{\delta_1^*} \frac{r_a}{r} \end{aligned} \right\} \quad (75)$$

For a rotor without entrance guide vanes, $\delta_1^* = -1$. If the total pressure rise Δp_g , the tangential velocity $r_a \omega$, and the throughflow velocity c_m are given, then ψ and φ are defined. The rotor efficiency is about constant over the entire rotor cross section when $\epsilon = \epsilon_{\min}$ is so chosen that the operating point of the sections in diagram I lies on a concave upward parabola (see equation (75)) with vortex at the origin of the coordinates. That is, the X-Y-points corresponding to the neighborhood of the hub section lie farthest from the origin. Since ζ_{Ag} is restricted upward equation (74) gives a simple estimate of the necessary solidity λ . For a fairly high pressure coefficient ψ and a small hub diameter, λ becomes very large for sections near the hub. But according to existing experimental knowledge it seems advisable to avoid high solidity. Besides an increase in angular velocity, which is limited by technical difficulties for the most part, there are essentially two possibilities to keep the solidity small: Make the hub rotor r_i/r_a large. This shortens the parabola discussed previously, but, at the same time, it increases the throughflow velocity and hence X for fixed outside diameter, so that the parabola is shifted to the right in the X-Y-diagram. Figure 7 thus shows that both measures reduce K and hence, from equation (74), the necessary solidity.

The first of formulas (75) shows a further possibility of decreasing Y and hence, in general, K . In the case of right-hand rotation,

$$\phi_1^* = -1 + \phi_1 \left(\frac{r_a}{r} \right)^2 \quad (76)$$

The subscript 1 denotes a plane before the rotor but behind the entrance guide vanes. The absolute value of ϕ_1^* accordingly can be increased by using the entrance guide vanes to pre-twist the fluid oppositely to the rotor direction of rotation. By equation (75) this method reduces Y efficiently. By the second formula of (75), X is reduced proportionately, the operating point X, Y of diagram I lying on the straight line connecting the origin and the point corresponding to $\phi_1^* = -1$. The pre-twisting decreases K more effectively as the angle between the tangent to the curve $K = \text{constant}$ and this straight line is greater. This is the case primarily in the left part of diagram I; hence a pre-twist appears advisable only for small throughflow velocities.

Formula (51) shows that pre-twisting ($\phi_1^* < -1$) lowers the efficiency of a rotor. For the rest, the efficiency depends largely on f_1 for fixed ϕ_1^* , since the factor of f_1 in equation (51) becomes very large for good glide angles. Diagram II (fig. 8) shows f_1 as a function of X and Y . For constant Y , f_1 has its maximum value on the straight line $\cot \beta = 1$. This line connects, according to the developments of IV,2, the points $X = 0, Y = 4$ and $Y = 0, X = 1$. For good rotor efficiency, the operating point must be designed to fall in the neighborhood of this straight line. This condition governs the choice of rate of speed, the choice of pre-rotation, but above all, the choice of r_1/r_a , since for fixed outer diameter and given delivery volume, the throughflow velocity and hence X is a function of the hub ratio.

For vanishing throughflow velocity - that is, $X = 0$ - there is $f_1 = 0$. In this case the efficiency is independent of c according to equation (51) and is solely a function of f_2 for fixed ϕ_1^* . Since f_2 increases with Y , useful efficiencies for very small throughflow velocities are obtained only with large Y .

The factor f_2 loses its effect on the efficiency at all but small distances from the y-axis. It is evident from formula (51) and diagram II (fig. 8) that for fixed δ_1^* , there is a general tendency for the rotor efficiency to increase with increasing Y - that is, higher loading. The glide angle is, of course, assumed to be independent of the loading. This is true, however, only in a certain range, so that the maximum efficiency of a rotor family of the same profile first increases somewhat with the loading but then decreases. (See reference 8.)

2. General Conclusions for Guide Vanes

Similar conclusions for stationary guide vanes are easily secured with the aid of diagrams III and IV (figs. 9 and 10). However, the following problem is pointed out: The exit guide vanes have the task of converting the energy of the tangential velocity component into pressure. In those cases in which the tangential exit velocity components are not found disturbing, it is profitable to insert exit guide vanes only when the surrender of the kinetic energy of rotation would imply a perceptible loss. The question of the magnitude of this energy therefore arises. The tangential component of the absolute exit velocity of the rotor is by equations (49), (76), and (50),

$$\frac{c_{u_2}}{r_a \omega} = \left(\delta_1 + \frac{\psi}{2\eta} \right) \frac{r_a}{r}$$

The subscripts 1 and 2 denote the planes before and behind the rotor. This equation yields the ratio of the kinetic energy corresponding to c_{u_2} to the energy gain through the rotor:

$$\frac{\left(\frac{c_{u_2}}{r_a \omega} \right)^2}{\psi} = \frac{\left(\delta_1 + \frac{\psi}{2\eta} \right)^2}{\psi} \left(\frac{r_a}{r} \right)^2 \quad (77)$$

If a pre-rotation opposite to the direction of rotor rotation is imparted to the fluid by a set of entrance guide vanes, then $\delta_1 < 0$ in the case of right-hand rotation. For $\delta_1 = -\frac{\psi}{2\eta}$, c_{u_2} vanishes so that no exit

guide vanes are necessary. With fixed entrance guide vanes, however, this condition is fulfilled only for a single operating condition. The pre-rotation imparted to the fluid by fixed entrance guide vanes is directly proportional to the axial throughflow velocity (equation (59)), while the pressure coefficient, as shown later, normally increases with decreasing throughflow velocity.

Since the tangential velocities behind the fan have a disturbing effect in wind tunnels with closed return passage, fans without exit vanes are useful only for tunnels with a single jet cross section. The minor changes in fan-operating condition introduced by the variable model drag are negligible. Wind-tunnel fans designed for operation with different jet cross sections must be fitted with exit guide vanes. These are easily constructed by means of diagram III, so that the exit rotation vanishes for all the operating conditions which might arise. For instance, if a high solidity $\lambda \geq 1.43$ is chosen (see reference 4, p. 42), the direction at the exit of the guide vanes is independent of the entrance direction. For the design of guide vanes complying with the condition of no rotation at the exit over a large operating range, the procedure is as follows: Select two possible operating conditions X^* , Y^* from the rotor exit velocities and the condition of no rotation at exit. For this purpose only X^* needs to be ascertained, and Y^* is chosen to lie on the dotted line in diagram III, according to section IV, 3. Then read off the coefficient K and $\tan \beta$ from diagram III for each cascade section. Since the angle difference $\Delta\beta$ for both operating conditions is equal to the difference in angle of attack, equations (74) and (61) yield the equation

$$\Delta K = \lambda k \frac{d\zeta_{Ae}}{d\alpha} \Delta\beta$$

from which λk can be calculated. The corresponding λ is then easily obtained by means of a diagram showing the cascade factor k as a function of $1/\lambda$. (See reference 4.) The angle difference $\Delta\beta$, or $\Delta\alpha$, must be small enough to lie within the range of angles of attack for which the profile flow adheres. This specification of the solidity gives two possible operating points of the exit guide vanes which lie on the dotted line of diagram III. This means that the flow at exit from the guide vanes is free from rotation. All other operating points

of the specified guide vanes for which the profile flow adheres will lie on the dotted line of diagram III. Rotation-free flow will no longer obtain when separation of flow sets in.

Incidentally it should be noted that it is not always advantageous to convert all the rotation to pressure by means of exit guide vanes. For instance, if a diffuser is used to convert the axial velocity into pressure, the diffuser efficiency can be considerably increased by means of a small rotational velocity. (See reference 9.)

3. Rotor Design

For the discussion of rotor design the throughflow condition (equation (23)) is utilized. From equations

(45) and (50) $\Delta\theta = \frac{1}{2} \left(\frac{\Psi}{\eta} \right)$ which entered in equation (23)

gives, after a short calculation:

$$\frac{\partial}{\partial R} (\varphi_2^2 - \varphi_1^2) = \left[\eta - \frac{1}{R^2} \left(\frac{\Psi}{2\eta} + \theta_1 \right) \right] \frac{\partial}{\partial R} \left(\frac{\Psi}{\eta} \right) + \frac{\Psi}{\eta} \left[\frac{\partial \eta}{\partial R} - \frac{1}{R^2} \frac{\partial \theta_1}{\partial R} \right] \quad (78)$$

The discussion is, for the present, limited to rotors without entrance guide vanes. In this case $\theta_1 = 0$ and equation (78) becomes

$$\frac{\partial}{\partial R} (\varphi_2^2 - \varphi_1^2) = \left[\eta - \frac{1}{R^2} \frac{\Psi}{2\eta} \right] \frac{\partial}{\partial R} \left(\frac{\Psi}{\eta} \right) + \frac{\Psi}{\eta} \frac{\partial \eta}{\partial R} \quad (79)$$

In the normal working range of a good rotor η is approximately constant; hence the last term on the right-hand side likewise vanishes. If the fan sucks the fluid from a large reservoir in which it is practically at rest, then φ_1 is constant over the cross section with the use of a proper entrance duct. In the event that φ_2 itself is to have a uniform distribution, either $\eta = \frac{1}{R^2} \frac{\Psi}{2\eta}$, or

the pressure coefficient Ψ must be constant over the rotor cross section according to equation (69). The first condition will be analyzed later. The second conforms with the considerations of the introduction.

If a uniform axial velocity distribution is specified for both the operating condition of the design

calculation and the neighboring range, a well defined distribution of section solidity λ must be chosen. To fix this distribution, the design operating point of every rotor section is marked in diagram I. To illustrate, if the throughflow coefficients φ_j and the pressure coefficients ψ_j are given, the design operating points are

defined by $X_j = \varphi_j \frac{r_a}{r}$, $Y_j = \left(\frac{\psi}{\eta}\right)_j \left(\frac{r_a}{r}\right)^2$ The rotor effi-

ciency must next be estimated, but with the aid of diagram II and the first approximation for the operating point X_j, Y_j , this estimate can be improved. Fixing the solidity of any one section of radius r_1 enables the entire X - Y -characteristic of the section to be constructed with the aid of the profile polar. Then select an operating point $X_h(r_1), Y_h(r_1)$ of this characteristic, which does not coincide with the design operating point. According to equation (79) $\varphi_2 = \varphi_1$ and $\varphi_h(r) = \varphi_h(r_1)$ since $\varphi = \frac{1}{2}(\varphi_2 + \varphi_1)$, on the assumption that ψ_h and η_h are themselves constant for this operating condition over the rotor cross section. On this basis the corresponding operating points of the other sections are directly indicated:

$$X_h(r) = \frac{r_1}{r} X_h(r_1), \quad Y_h(r) = \left(\frac{r_1}{r}\right)^2 Y_h(r_1)$$

The accompanying values of $K_h(r)$ and the angle differences $\Delta\beta(r) = \Delta\alpha(r) = \beta_h(r) - \beta_j(r)$ permit the calculation of the solidity exactly as for the exit guide vanes. The result is a blade chord distribution, which decreases greatly toward the outer section.

In the event that the energy of the entering flow exhibits considerable nonuniformities, it will be endeavored to fill these "energy holes" with additional energy from the rotor. A typical representative of this case is the open-jet wind tunnel with fan situated close behind the collecting cone. The thickness of the boundary layer before the blower is of the order of magnitude of half the collecting tube radius. If the static pressure in the entrance cross section is equal to zero, the total pressure, referred to $\frac{1}{2}\rho(r_a\omega)^2$, in the entrance

cross section is given by φ_1^2 . The requirement of constant total pressure behind the rotor is synonymous with $\Psi = \text{constant} - \varphi_1^2$. The constant is specified by the energy level necessary to overcome the throttling. In this case, too, there is a constant efficiency over the entire rotor cross section; hence equation (79) can be written in the following form:

$$\frac{\partial}{\partial R} (\varphi_2^2) = \frac{\text{constant} - \varphi_1^2}{2\eta^2 R^2} \frac{\partial}{\partial R} (\varphi_1)^2$$

The φ_2 distribution corresponding to a given φ_1 distribution can be calculated by this equation. The throughflow velocity in the plane of the rotor is then likewise known: $\varphi = \frac{1}{2} (\varphi_1 + \varphi_2)$. Since $\varphi(r)$ as well as $\Psi(r)$ are then given, the design operating point in diagram I is fixed for every section. The distribution of solidity to give uniform total head distribution behind the rotor for the neighboring operating points is found the same way as in the previously discussed case.

Analogous considerations can be made for rotors with entrance rotation. If $\vartheta_1(r) = \text{constant}$, the above line of reasoning is not changed, except that equation (78) must be chosen as starting point instead of equation (79).

4. Estimate of the Throughflow Distribution

In conclusion, a number of simple model problems are worked out, which enable the designer to appraise the results of his measures.

For entrance guide vanes, $\vartheta_1 = 0$. On the assumption that the distribution of the energy losses over the cross section of the stator is uniform, equation (24) yields:

$$\frac{\partial}{\partial R} (\varphi_1^2 - \varphi_2^2) = \frac{1}{R^2} \frac{\partial}{\partial R} (\Delta\vartheta)^2 = \frac{1}{R^2} \frac{\partial}{\partial R} (\vartheta_2)^2 \quad (80)$$

This equation indicates that for $\vartheta_2 = \text{constant}$ there is no change in the throughflow distribution through the guide vanes.

An attempt was made to have guide vanes impart to the air a rotation increasing linearly with the distance from the axis (reference 9), in which case $\phi_2 = CR$, where C is a constant. Introducing this value into equation (80) readily affords

$$\varphi_2^2 = \varphi_1^2 + 2C^2 \ln \frac{1}{R} + \text{constant} \quad (81)$$

φ_2 accordingly increases without limit for $R = 0$ and drops quickly with increasing radius. The throughflow condition is not valid for such a marked variation, since it was assumed for its deviation that $\Delta\varphi = \varphi_2 - \varphi_1$ is small of the first order. At any event, equation (81) indicates correctly the character of the flow: because, apart from the fact that the desired tangential velocity in the attempt cited previously was not completely attained, a strong displacement of the axial flow in the sense of equation (81) was experimentally established.

As previously stated, the deflection of the flow through entrance guide vanes is proportional to the throughflow velocity (equation (59)). If the guide vanes are designed so that ϕ_2 is constant for constant throughflow velocity, then $\phi_2 = C\varphi$, where C is a constant. By neglecting a quadratic term in $\Delta\varphi$, $2(\varphi_1^2 - \varphi^2)$ can be substituted for $(\varphi_1^2 - \varphi_2^2)$ and equation (80) becomes

$$\frac{\partial}{\partial R} (\varphi^2) = \frac{1}{1 + \frac{1}{2} \left(\frac{C}{R}\right)^2} \frac{\partial}{\partial R} (\varphi_1^2)$$

Since $\frac{1}{1 + \frac{1}{2} \left(\frac{C}{R}\right)^2} < 1$, this equation shows that every

"valley" in the φ_1 distribution is more or less strongly smoothed out - that is, most strongly in the neighborhood of the hub.

The most important case for exit guide vanes is that in which the fluid leaves the guide vanes in purely axial direction, where $\phi_2 = 0$ and $\Delta\phi = -\phi_1$. On the hypothesis that the energy loss Δp_g is constant over the whole cross section, equation (24) yields

$$\frac{\partial}{\partial R} (\varphi_2^2) = \frac{\partial}{\partial R} (\varphi_1^2) + \frac{1}{R^2} \frac{\partial}{\partial R} (\psi_1^2)$$

Here also there is no change in throughflow distribution for $\Delta\psi = -\psi_1 = \text{constant}$. If ψ_1 increases toward the outside, φ_2 exhibits a stronger increase toward the outside than φ_1 , and vice versa. The boundary layer on the outer wall merits particular attention. Owing to the tip clearance, the rotation behind the rotor decreases

toward the wall. Hence $\frac{\partial}{\partial R} (\psi_1^2) < 0$ in the neighborhood of the outer wall, and from the preceding equation it follows that the boundary layer of the φ_2 distribution is worse than that of the φ_1 distribution.

The conditions at the rotor are most difficult to survey. To arrive in some degree at general formulas for this case, sweeping simplifications, which lessen the value of the appraisals, must be made. In spite of this, however, the qualitative insight provided by the formulas is useful.

According to figure 6, the profile angle of attack increases with decreasing throughflow velocity. So long as the flow does not separate, the coefficient K also increases with decreasing φ . Diagram I indicates that

the same fact applies to Y and hence to $\frac{\psi}{\eta}$. If

$\left(\frac{\psi}{\eta}\right)_j$, φ_j are the characteristics serving as basis of the

design, the function $\frac{\psi}{\eta}(\varphi)$ in the neighborhood of the

design point can be represented by a Taylor series, of which only the first term is retained. Worked out examples show that a good approximation is obtained for $\frac{\psi}{\eta}(\varphi)$, except when separation of flow occurs. Thus,

$$\frac{\psi}{\eta}(\varphi, R) = \frac{\psi}{\eta}(\varphi_j) + a(R) [\varphi_j - \varphi]$$

where the coefficient $a(R)$ is always positive. Differentiation with respect to R yields

$$\frac{\partial}{\partial R} \left(\frac{\psi}{\eta}\right) = (\varphi_j - \varphi) \frac{\partial a}{\partial R} - a \frac{\partial \varphi}{\partial R}$$

By entering these values into equation (78), the limitation to $\psi_1 = \text{constant}$ and $\eta = \text{constant}$ with $\varphi_2^2 - \varphi_1^2 = 2(\varphi^2 - \varphi_1^2)$ leaves:

$$\frac{\partial \varphi}{\partial R} \left[\varphi + \frac{a}{4} \left\{ \eta - \frac{1}{R^2} \left(\frac{\varphi}{2\eta} + \psi_1 \right) \right\} \right] = \varphi_1 \frac{\partial \varphi_1}{\partial R} + \frac{\varphi_j - \varphi}{4} \left\{ \eta - \frac{1}{R^2} \left(\frac{\psi}{2\eta} + \psi_1 \right) \right\} \frac{\partial a}{\partial R}$$

If $\Delta\varphi$ is assumed small compared to φ_1 , φ_1 can substitute for φ in the preceding equation, so that

$$\frac{\partial \varphi}{\partial R} = \frac{\varphi_1}{\varphi_1 + \frac{a}{4} \left[\eta - \frac{1}{R^2} \left(\frac{\psi}{2\eta} + \psi_1 \right) \right]} \frac{\partial \varphi_1}{\partial R} + \frac{1}{4} \frac{(\varphi_j - \varphi_1) \left[\eta - \frac{1}{R^2} \left(\frac{\psi}{2\eta} + \psi_1 \right) \right]}{\varphi_1 + \frac{a}{4} \left[\eta - \frac{1}{R^2} \left(\frac{\psi}{2\eta} + \psi_1 \right) \right]} \frac{\partial a}{\partial R} \quad (82)$$

For a rotor design in which the solidity distribution was defined for $\varphi_1 = \text{constant}$, the curves of $\frac{\psi}{\eta}(\varphi)$ for all sections coincide, and $\frac{\partial a}{\partial R} = 0$. Since, at the same time, $\frac{\partial \varphi_1}{\partial R} = 0$, then φ itself must be constant with $\varphi_1 = \text{constant}$, in agreement with the conclusions of previous arguments.

The condition $\frac{\partial a}{\partial R} = 0$ is, for the present, retained.

It depends solely on the choice of λ distribution, hence is given by the blade design. If the φ_1 distribution has local hills or valleys, these are either accentuated or weakened depending on whether $\left[\eta - \frac{1}{R^2} \left(\frac{\psi}{2\eta} + \psi_1 \right) \right]$ is negative or positive. The effect of this bracketed expression is so much greater as φ_1 is smaller. The sign changes for:

$$\left(\frac{\psi}{\eta}\right)_{cr} = 2(R^2 \eta - \delta_1)$$

For fixed δ_1 and η , $\left(\frac{\psi}{\eta}\right)_{cr}$ is smaller closer to the hub. If the fluid is given a rotation opposite to the rotor direction of rotation, then $\delta_1 < 0$ and $\left(\frac{\psi}{\eta}\right)_{cr}$ becomes greater.

The fact that for $\frac{\psi}{\eta} > \left(\frac{\psi}{\eta}\right)_{cr}$ the hills or valleys of the axial velocity distribution are accentuated by the fan may be regarded as a manifestation of instability of the rotor flow. For

$$\varphi + \frac{a}{4} \left[\eta - \frac{1}{R^2} \left(\frac{\psi}{2\eta} + \delta_1 \right) \right] = 0$$

the variation of the nonuniformities of the φ_1 distribution increases without limit and has, besides, an indefinite sign. In fact, difficulties arise on rotors with high pressure coefficients which seem to indicate instability of flow even for those operating conditions at which flow separation likely has not yet occurred. The

critical value of $\left(\frac{\psi}{\eta}\right)_{cr}$ itself appears to be substantially lower than that given by the formulas if figured with the high average efficiency of the theory. This discrepancy probably is due to the fact that, on the one hand, the local efficiency may be very much smaller than the average efficiency, and on the other, that the throughflow condition is, on principle, not suitable for stability investigations; since stationary conditions had been assumed in its derivation in the beginning. An extension of the theory in this direction is under way.

If $\frac{\partial a}{\partial R} \neq 0$, the second term on the right-hand side of equation (82) also must be noted. In this term the expression

$$\varphi_1 + \frac{a}{4} \left[\eta - \frac{1}{R^2} \left(\frac{\psi}{2\eta} + \delta_1 \right) \right]$$

plays the same role as previously. The following is limited to

$$\eta - \frac{1}{R^2} \left(\frac{\Psi}{2\eta} + \delta_1 \right) > 0$$

a condition which, according to the preceding developments, probably is a necessary premise for practical rotor design. In this case, the sign of the second term of equation (82)

is the sign of $(\varphi_j - \varphi_1) \frac{\partial a}{\partial R}$. As is subsequently shown, only positive values of $\frac{\partial a}{\partial R}$ occur so that the second

term on the right of equation (82) effects, for $\varphi_1 < \varphi_j$, a reduction of the throughflow velocity in the neighborhood of the hub and an increase at greater distances from the hub. The opposite holds true for $\varphi_1 > \varphi_j$.

In conclusion, the influence of a nonuniform axial velocity on the total efficiency is briefly discussed. If the entire total head is counted for the efficiency, the distribution of axial exit velocity is of no importance. It is different when the exit kinetic energy is to be recovered. In this case, a diffuser must be used behind the fan to convert the exit kinetic energy to pressure. Let c_{\min} be the smallest absolute velocity in a cross section behind the fan but before the diffuser, in which, moreover, the static pressure has become constant. Then, as is easily evident from Bernoulli's equation, at

the most, $\frac{1}{2} \rho c_{\min}^2$ is recoverable. The nonuniform axial exit velocity distribution thus has an unavoidable exit loss in consequence. On the other hand, it is also conceivable that the diffuser efficiency can be bettered by a velocity distribution which increases outwardly. Experiments of this kind are unfortunately not available, so that the question of the influence of the axial exit velocity distribution on the fan efficiency must, for the present, remain unanswered.

VII. EXPERIMENTAL AND THEORETICAL INVESTIGATION OF THREE ROTORS AND TWO STATORS

1. Description of Test Stand, Calibrations

Figure 16 shows the layout of the test stand. It consists of a tube 4 meters (13.1 ft) in length and 500 millimeters (19.7 in.) in diameter; its inlet side is enlarged to form a well-rounded, broadly faired entrance cone. The streamline hub is built into the tube, its maximum diameter being 250 millimeters (9.85 in.). The forward part of the hub is held by three faired struts and is designed to carry the bearing for the rotor. The rear part of the hub is carried by the guide vanes and at the tip by three faired struts.

The shaft leading from motor to the head of the hub is faired. The motor is mounted so as to be free to swing on both its shaft ends. It carries a scale arm by which the torque can be measured.

Several difficulties were encountered in the determination of the scale zero, because the ball bearings, when stationary, have comparatively great friction. But after the ball bearings were washed clean, the zero point could be determined with sufficient accuracy. The slight asymmetries of the rotor were eliminated by weighing in numerous rotor positions.

The determination of the pure rotor torque requires the subtraction of the bearing friction torque from the measured torque. The usual bearing friction measurement, which consists of an extrapolation of the torque to zero angular velocity, proved to be very unreliable because the motor angular velocity could not be made small enough. For this reason, the zero rotation torque was determined with rotating hub and rotor blades removed. Check measurements with rotating shaft but concurrently removed rotor hub proved the hub bearing friction negligibly small.

The motor speed was measured by a revolution counter operating for 1 minute. The revolution counter was inserted electromagnetically by means of slip rings driven by a small synchronous motor. The time scale could be adjusted very conveniently by small modifications of the contact path.

A diaphragm was attached at the end of the test stand for throttling, the opening being variable by means of a valve and cover plates. To include the region of very small throttling, the diaphragm A was removed for several measurements and a diffuser put in its place.

For the quantity measurement, the wall was pierced at I. With v_I denoting the velocity in the cross section at the test station, Bernoulli's equation gives, on the assumption of $v_I = \text{constant}$ over the cross section:

$$v_I = \sqrt{\frac{2}{\rho} (-p_I)}$$

The throughflow volume is obtained by multiplication with the entrance cross section F_I . This formula is not strictly valid because of the boundary layer formation, and must be corrected by a pipe factor. This was determined by careful measurements of the velocity distribution. It is

$$Q = f \sqrt{\frac{2}{\rho} (-p_I)} F_I$$

where $f = 0.985$

The total head difference was recorded by means of the pierced wall station II. On the assumption of constant velocities in cross sections I and II

$$\Delta p_g = \Delta p + \frac{\rho}{2} c_I^2 \left[\left(\frac{F_I}{F_{II}} \right)^2 - 1 \right]$$

where Δp is the difference in wall pressure and F_{II} the cross section of measuring plane II. Since the diameter of the shaft casing tube is only 50 millimeters, $F_I \approx F_{II}$; hence the last term of the previous equation can be discounted. The procedure would be more exact if, instead of the preceding equation, the following average value equation is used:

$$\Delta p_g = \Delta p + \frac{1}{F_{II}} \int_{F_{II}} \frac{\rho}{2} c_{II}^2 dF - \frac{1}{F_I} \int_{F_I} \frac{\rho}{2} c_I^2 dF$$

The two integrals for the design operating point were defined experimentally and found to be sufficiently coincident; hence the formula $\Delta p_g = \Delta p$ is obtained again. This derivation of the preceding formula includes the small increase of exit energy due to nonuniform distribution (boundary layer, hub drag) for the design operating point. For other operating conditions, the effect of greater nonuniformities in increasing the exit energy, is, for simplicity, disregarded so that the formula given previously was regarded as valid for all operating conditions.

2. Data on Rotors and Stators

The fans tested were of the single-stage, axial-flow type, with exit guide vanes and without entrance guide vanes. The common characteristics of the first three eight-blade rotors were the following: The design operating point was the same for all three rotors. A pressure coefficient of $\bar{\Psi} = 0.188$ and a flow coefficient of $\bar{\Phi}_0 = 0.45$ was specified for the entire fan, including the hub diffuser. The total pressure boost set up by the rotor is naturally to be decreased by the diffuser and the guide vane losses. The diffuser efficiency was assumed at $\eta_0 = 0.85$ (see Hütte, vol. I, 26th ed., p. 377), the guide vane losses being computed according to the formulas derived in section IV, 5. The corresponding Göttingen 622 to 625 airfoil sections and those derived by interpolation were used in the rotor blade design, and in such a way that the thickness ratio of the profile from the hub outward decreased uniformly for all the rotors. The profile angle $\delta_1 = 90^\circ - \delta$ was so determined that the total pressure boost of the rotor for the design operating point was constant over the entire rotor cross section. To be sure, this goal was not entirely achieved. This was largely due to the fact that the corrections for finite blade thickness were allowed for by a rough - that is, excessive average value - since the correction formulas in section V, 2 were at the time not yet in existence. Likewise, the dependence of the polars on Reynolds number could not be considered. The polar measurements then existing had been secured at only one Reynolds number. It should also be mentioned that through an error, the profile sections near the hub of rotor II were curved a little too much.

The three rotors of this family differed in the distribution of their blade chords. Rotor I had a profile chord linearly decreasing toward the outside; rotor II, constant; and rotor III, linearly increasing.

The exact data for the three rotors are given in figures 17 to 19 and in table I. The chord distribution was secured on the basis of the dimensionless profile chord with a rotor radius of 250 millimeters (9.85 in.), rather than the solidity λ , as it afforded a clear representation of the chord distribution. The profile ordinates are given as usual in percent of the local profile chord.

The data for both stators are shown similarly in figures 29 and 21 and table II. Stator I had nine blades shaped from 2 millimeter (0.0787 in.) thick sheet. The guide vanes were designed to remove all the rotation at the design operating point. In order to avoid excessive solidity, the lift coefficient chosen for these operating conditions was comparatively large. Consequently the guide vane flow separated at a throttling not much greater than the design throttling. The resultant lower efficiency is discussed later. The design of stator I was based on the cambered circular arc profile with

$\frac{f}{l} = 0.05$ (reference 10, p. 96), f being the camber and l the profile chord.

Stator II also had nine blades the design of which was based on the cambered Göttingen 624 airfoil section. It was hoped that by the use of the profiled blades the flow would adhere over a large throttling range especially since, according to the experimental results gained with guide vane I, the operating condition of rotation-free exit was shifted toward lower φ_0 -values - that is, greater throttling. It is to be noted that neither guide vane quite satisfied the condition for rotation-free exit over a large throttling range postulated in section VI, 2.

3. Recalculation of Rotor and Stator

To insure an easier interpretation of the test data, the theoretical investigation of the rotors is given first. The individual cascades of the fan are calculated in the order of their arrangement in the fan installation - that is, proceeding in free-stream direction - so that in every case the distribution of free-stream velocity and of the

initial rotation can be regarded as known. The procedure indicated by the foregoing derivations is briefly summarized here: Each rotor is visualized as being divided by mean stream surfaces into cascade sections. The mean stream surfaces are defined as the rotationally symmetrical stream surfaces corresponding to the previously defined mean velocities. For each of these sections, the X -, Y -characteristic, the efficiency, and the tangential exit velocity has been calculated by means of the diagrams of section IV without regard to their mutual influence, but with allowance for the corrections for the circulation and the thickness. To illustrate the order of magnitude of these corrections, the cascade effect coefficient k is shown plotted against $R = \frac{r}{r_a}$ in figure 22 for the three rotors. The correspondence to the individual rotors is indicated by Roman numerals. The factor $D\lambda^2$, necessary for the prediction of the effect of finite blade thickness, is shown as a dashed curve. Quantity D is the ratio of mean profile thickness to chord and, because of the relationship of the Göttingen 622 to 625 airfoil sections, is proportional to the maximum thickness d :

$$D = 0.675 \frac{d}{l}$$

The calculation of the cascade section characteristics is based on the profile polars converted to infinite aspect ratio. (See reference 6, p. 108.) By formulas

$$(61), (43), \text{ and } (70), \quad K = \frac{\lambda' \zeta_T}{\cos \beta} \quad \text{is obtained as a func-}$$

tion of β , where β , for the case of right-hand wheel rotation, must be put equal to $\delta + \alpha$; for the sake of trial, $K(\beta)$ was calculated for various Reynolds numbers. It was found that K is fairly independent of the Reynolds number. This fact is evident from equation (43) when considering that, apart from the zone of small angles of attack, the lift coefficient ζ_A increases somewhat with increasing Reynolds number; whereas the glide angle ϵ becomes smaller. Obviously this holds only for average values of $\cot \beta$. If $\cot \beta$ is very small, $K(\beta)$ decreases with increasing Reynolds number; the opposite holds true for large values of β . To prevent misconceptions, it should be noted that, in contrast to $K(\beta)$, the efficiency is closely related to the Reynolds number.

If $K(\beta)$ is known; the methods given in section IV, 2 can be used to determine the X-,Y-characteristic of each fan section. The formulas (69) give the transition to X_0, Y_0 where, in the factor of $\frac{\pi}{6} D\lambda^2$, Y_0 can be substituted for Y without appreciable error. For a rotor without initial rotation $\phi_0^* = -1$; and hence, according to equations (45) and (50),

$$X_0 = \varphi_0^*$$

$$Y_0 = \frac{\psi^*}{\eta}$$

From the definitions of φ_0^* and ψ^* the relations

$$\varphi_0 = R X_0$$

$$\frac{\psi}{\eta} = 2\Delta\phi = R^2 Y_0$$

are readily derived.

The ensuing sample calculation illustrates the significance of k and D . Rotor III, for which the correction terms are highest according to figure 22, is to serve for this purpose. The calculation is carried out at first with cascade effect of the finite blade thickness as well as the "neighboring circulation" neglected - that is, $D = 0$ and $k = 1$ are used in all the formulas. With these approximations the dotted curves of figure 23 are obtained for four sections of rotor III. With k as given by figure 22 but retaining $D = 0$, the solid curves

of figure 23 are obtained. The curves $\frac{\psi}{\eta} (\varphi_0)$ accordingly

appear to be turned through a comparatively small angle by the cascade effect coefficient k . That is, the rotation is about the design operating point since, for this point, $\zeta_{Ae} = \zeta_{Ag}$ owing to the additional profile camber.

The dotted curves in figure 24 agree with the solid curves of figure 23. If the thickness correction D from figure 22 as well as the cascade effect coefficient is taken into account, the solid curves of figure 24 are obtained. For the sake of clarity only the curves for two cascade sections are shown. The effect of finite

profile thickness manifests itself largely as a shift of the curves to the left.

It would seem, on comparing figures 23 and 24, as if the thickness correction were greater than the circulation correction. But this is not true because the principal portion of the circulation correction is anticipated by the extra camber and does not appear in figure 23.

To return to the comparison of the calculations for the three rotors, figures 25 to 27 show the curves $\frac{\psi}{\eta}(\varphi_0)$ for the four sections along with the section efficiencies, calculated from equation (51) and diagram II. The curves $\frac{\psi}{\eta}(\varphi_0)$ are, as previously assumed, approximately straight lines in their principal range. The most apparent difference among the three rotors is that the slope of the curves to the φ_0 -axis on rotor I is about the same for all sections, and becomes so much greater on the other two rotors as the corresponding sections are farther from the hub. If $\frac{\partial}{\partial \varphi_0} \left(\frac{\psi}{\eta} \right) = -a(R, \varphi_0)$, then $\frac{\partial a}{\partial R}$ is so much greater, the faster the profile chord increases toward the outside. Complete coincidence of the cascade section curves $\frac{\psi}{\eta}(\varphi_0)$ - that is, $\frac{\partial a}{\partial R} = 0$ - requires a still stronger decrease of profile chord to the outside than is the case with rotor I.

Since the hub profile is the same for all three rotors, the curves $\frac{\psi}{\eta}(\varphi_0)$ and $\eta(\varphi_0)$ agree almost exactly for the cascade nearest to the hub. (Considerations of the excessive camber of the profiles near the hub are omitted in the interests of systematic analysis.) On the other hand, the efficiency curves of the sections farthest from the hub show further distinctive characteristics of the three rotors, just as the curves $\frac{\psi}{\eta}(\varphi_0)$ did. The efficiency depends primarily on the glide angle ϵ , which increases sharply at separation of flow. Increase of glide angle means reduction in efficiency (equation

(51)), so that the highest cascade section efficiencies indicate the region in which the flow adheres. The region of adhering flow on a given profile is defined by a certain angle of attack range between α_{\min} and α_{\max} . These angles of attack correspond, for fixed blade angle δ , to the stream angles β_{\min} and β_{\max} , because of $\alpha = \beta - \delta$. A change in blade angle δ is, as a result, accompanied by a displacement of the region $\beta_{\min} < \beta < \beta_{\max}$. It follows from diagram I that larger β -values correspond to smaller φ_0 -values. On the other hand, diagram I gives a mean stream angle β_j for the prescribed design operating point. Since $\alpha_j = \beta_j - \delta_j$, larger δ_j correspond to smaller α_j . Since, at the same time, the design operating point corresponds to a definite coefficient $K \approx \lambda \zeta_A(\alpha_j)$, a larger δ_j is necessarily associated with a larger λ ($\zeta_A(\alpha_j)$ becomes smaller with smaller α_j). Summarizing, it may be stated that the region of adhering flow can be shifted toward small φ_0 -values by increasing the solidity λ . The position of the efficiency curves for the outer sections in figures 25 to 27 confirms this argument.

The section characteristics of figures 25 to 27 were obtained without regard to their mutual influence. To determine an operating condition that will hold simultaneously for the entire rotor, the correlation of the quantity coefficient $\varphi_0(R)$ must be determined with the aid of the throughflow condition. All φ -, δ -values in the following calculations refer to infinitely thin blades. The subscript 0, which should be used throughout, is omitted for the sake of simplicity. The throughflow condition in the form of equation (79) is suitable for the purpose in view. Since the rotor sucks the air out of a large reservoir (fig. 16), φ_1 can be assumed constant if the small boundary layer development in a properly designed entrance cone is discounted. Writing further $\varphi_2 = \varphi_1 + \Delta\varphi$, φ_2^2 may be put equal to $\varphi_1^2 + 2\Delta\varphi\varphi_1$ to the order of approximation maintained so far. Then the difference equation corresponding to the differential equation (79) gives:

$$\begin{aligned} \Delta\varphi(R_{\nu+1}) - \Delta\varphi(R_{\nu}) &= \frac{1}{2\varphi_1} \left\{ \left[\eta(R'_{\nu}) - \frac{1}{2(R'_{\nu})^2} \frac{\psi}{\eta}(R'_{\nu}) \right] \left[\frac{\psi}{\eta}(R_{\nu+1}) - \frac{\psi}{\eta}(R_{\nu}) \right] \right. \\ &\quad \left. + \frac{\psi}{\eta}(R'_{\nu}) \left[\eta(R_{\nu+1}) - \eta(R_{\nu}) \right] \right\} \quad (83) \end{aligned}$$

where R_{ν} denotes the calculated section; R'_{ν} is a mean value defined by $R_{\nu} < R'_{\nu} < R_{\nu+1}$. This difference equation is easily resolved by iteration, when proceeding from an assumed distribution $\varphi(R_{\nu})$ corresponding to

$$\varphi_1 = \frac{1}{F} \int_F \varphi(r) 2\pi r dr$$

where F is the throughflow cross section. The corresponding values of $\frac{\psi}{\eta}(R_{\nu})$ and $\eta(R_{\nu})$ are read from figures 25 to 27. The quantities $\frac{\psi}{\eta}(R'_{\nu})$ and $\eta(R'_{\nu})$ are equaled to

$$\frac{1}{2} \left[\frac{\psi}{\eta}(R_{\nu+1}) + \frac{\psi}{\eta}(R_{\nu}) \right] \quad \text{and} \quad \frac{1}{2} \left[\eta(R_{\nu+1}) + \eta(R_{\nu}) \right]$$

respectively. Substitution into equation (83) yields

$$\Delta\varphi^{(1)}(R_{\nu+1}) - \Delta\varphi^{(1)}(R_{\nu})$$

whence

$$\Delta\varphi^{(1)}(R_{\mu+1}) = \sum_{\nu=1}^{\mu} \left[\Delta\varphi^{(1)}(R_{\nu+1}) - \Delta\varphi^{(1)}(R_{\nu}) \right] + \text{constant}$$

The constant is determined with the aid of the conditional equation (25). The first approximation of the φ distribution is

$$\varphi^{(1)} = \varphi_1 + \frac{1}{2} \Delta\varphi^{(1)}$$

The calculation is repeated with this approximation until the $(m + 1)$ th approximation is in sufficiently exact agreement with the n th. The iteration method, as a rule, converges very quickly, so that by a skillful assumption of the resulting distribution, a single round of calculation suffices. Difficulties begin to arise in the region of separated flow, where the efficiency curves drop very steeply. The procedure necessarily does not converge here. Divergence generally means flow separation in the rotor; hence the rapidity of convergence, in a certain sense, may be regarded as a criterion for the stability of the rotor flow.

The solutions obtained by the foregoing procedure are indicated by thick cross lines in figures 25 to 27. In the region of adhering flow the ψ/η distribution is somewhat uniformized by the displacement of the φ_1 distribution. The opposite is true when the flow separates. On rotor I the $\zeta_{A_{max}}$ at the outer section is already exceeded for $\bar{\varphi}_0 = 0.324$.

The iteration still converges; therefore the throughflow distribution is still clearly defined. But from the marked decrease of velocity in the neighborhood of the wall, it may be concluded that the rotor flow is unstable at around $\bar{\varphi}_0 = 0.324$. On rotor II the $\zeta_{A_{max}}$ is likewise first reached at the outer sections. Instability is to be expected for a coefficient $\bar{\varphi}_0$ of about 0.273.

Moreover, in this particular case the profiles of all the sections operate simultaneously in the neighborhood of $\zeta_{A_{max}}$. For rotor III, on the other hand, $\zeta_{A_{max}}$ occurs first at the sections near the hub - that is, at a mean coefficient of $\bar{\varphi}_0 = 0.301$ - as a result of the strong displacement of the throughflow toward the outside. According to the conclusions so far the rotor flow should separate at the hub for a throughflow coefficient somewhat below that just given.

If the distribution is calculated for a greater number of mean throughflow coefficients, the rotor characteristics are readily secured: The quantities $\frac{\psi}{\eta}$ and η , for a definite average throughflow coefficient, are read off for each section; and the mean values $\bar{\psi}$ and $\bar{\eta}$ are

obtained by integration over the whole rotor plane. Figure 30 shows the result of this mean value formation for rotor III.

Since the calculation of the guide vanes manifests nothing substantially new, the procedure is only briefly indicated: The function $K(\beta) = \frac{\lambda' \xi_T}{\cos \beta}$ is first defined

by means of the section polars for each cascade section. The X^* , Y^* -characteristic and the factor f_3 , expressing the exit rotation in fractions of the entrance rotation, are found by means of diagram III and the procedure given

in section IV, 4. The energy loss $\frac{\Delta \psi^*}{\phi^{*2}}$ for the particu-

lar throughflow coefficient at any operating point X^* , Y^* of a section can be obtained from equation (60) with the aid of diagram IV. The calculation of the throughflow distribution is similar to that of the rotor by iteration of a difference equation, which is easily obtained from equation (24). The exit values of the rotor, obtained from the rotor distribution calculation for any average coefficient $\bar{\phi}_0$, serve as entrance values of ϕ_{01} and ψ_{01} - that is, in this particular case of rotation-free entrance into the rotor, $\phi_{01} = \bar{\phi}_0 + \Delta \phi_{rotor}$ and

$\psi_{01} = \frac{1}{2} \left(\frac{\psi}{\eta} \right)_{rotor}$ (Subscript 1 refers to the entrance

plane of the stator.) If the throughflow distribution ϕ^* for a mean throughflow coefficient $\bar{\phi}_0$ is known,

then the energy loss itself can be calculated from the

corresponding value of $\frac{\Delta \psi^*}{\phi^{*2}}$. The average energy loss is

again obtained by integration.

4. Comparison of Theoretical and Experimental Results

The rotor efficiency was obtained directly by means of total pressure measurements before and behind the rotor, although it was carried out along only one radial direction. However, since it is fairly safe to assume rotational symmetry on the rotor, they should permit a reliable calculation of the efficiency. The total head tube was insensitive to angle ($\pm 15^\circ$) within wide limits.

Nevertheless, the greatest possible care was taken to head the tube in the stream direction. Figures 28 and 29 show the distribution of total head increase for several throughflow coefficients on rotors I and III, respectively, together with the theoretical curves (dashes). Figure 29 is limited to the experimental curve for $\bar{\varphi}_0 = 0.247$ since the profile polars were not measured far enough to enable a calculation for this throughflow coefficient. Besides, the iteration procedure is not to be expected to converge for this mean throughflow coefficient; even here it is apparent that rotor III operates at a mean coefficient far below $\bar{\varphi}_0 = 0.301$. At this value, according to the foregoing arguments, the maximum lift coefficient of the hub section is already exceeded.

Apart from the neighborhood of hub and outer wall, there is good agreement between the theoretical and experimental curves. The latter decrease sharply in the neighborhood of the outer wall $\left(\frac{r}{r_a} \approx 1\right)$. This is largely due to the clearance losses. The increases occurring in the neighborhood of the hub are probably caused by the secondary flows mentioned at the end of section V, 3. The theoretical curve of rotor III shows a sharp decrease near the hub for $\bar{\varphi}_0 = 0.316$. (See fig. 29.) The reason is that the hub profile at the cited mean throughflow coefficient is at an angle of attack for which the polar of the isolated section already indicates incipient separation. The marked difference between theoretical and experimental total pressure distributions itself suggests that the separation phenomena on the hub profile do not occur in the same manner as on the isolated profile. Another unusual fact is that at very high loadings the increases are similar to those at the hub.

The total pressure distributions of figure 29 for rotor III were integrated over the rotor section, assuming rotational symmetry (besides the total pressure measurements of fig. 28, further measurements were made but omitted here for clearness). The throughflow volume and the torque on the rotor shaft were measured simultaneously with the total pressure distribution so that the rotor efficiency can be computed by means of the planimetered total head increase: If M denotes the torque applied to the rotor shaft, Q the flow per second, η the rotor efficiency, $\eta_{MD} = \Delta p_g Q$, or in dimensionless rotation,

$$\eta = \bar{\Psi} \bar{\varphi}_0 \frac{\frac{\rho}{2} r_a^3 \omega^2 F}{M}$$

where F is the cross section of the blade region. The efficiency obtained is shown as a dotted line in figure 30. The individual test points are identified separately. Their scatter is a measure of the certainty of the efficiency determination. Figure 30 also shows the measured total pressure curve $\Psi(\bar{\varphi}_0)$ and the curve

$$\frac{\bar{\Psi}}{\bar{\eta}} = \frac{1}{\bar{\varphi}_0} \frac{M}{\frac{\rho}{2} r_a^3 \omega^2 F}$$

From the definition of efficiency (equation (20)), it follows, by reason of

$$dM = \rho(rc'u_2 - rc'u_1) c_m 2\pi r dr$$

that

$$\frac{1}{\bar{\eta}_{th}} = \frac{1}{F} \int \frac{dM}{\varphi \Psi \frac{\rho}{2} r_a^3 \omega^2}$$

From two applications of the mean value theorem of integral calculus, it can be concluded that $\bar{\eta}$ is approximately equal to $\bar{\eta}_{th}$. Likewise:

$$\frac{1}{\bar{\varphi}_0} \frac{M}{\frac{\rho}{2} r_a^3 \omega^2 F} \approx \left(\frac{\bar{\Psi}}{\bar{\eta}} \right)_{th}$$

Figure 30 shows very good agreement of the curves $\frac{\bar{\Psi}}{\bar{\eta}}$.

This proves that, in any case, the torque theoretically obtained agrees very closely with the actual. For reasons discussed previously, the theoretical curve can be calculated only to $\bar{\varphi}_0 = 0.301$. The comparison of the curves $\bar{\eta}(\bar{\varphi}_0)$, and accordingly of the curves $\bar{\Psi}(\bar{\varphi}_0)$, proves less favorable. As already seen from figures 28 and 29, $\bar{\Psi}_{th} > \bar{\Psi}$. The additional loss, expressed by $\bar{\eta} < \bar{\eta}_{th}$, is attributable to the flow phenomena between

the blades and the outer wall. It might be supposed that the secondary flow at the hub also contributes to this loss. But experimental investigations, reported subsequently, indicate that the clearance loss accounts for the major part. The recalculation of rotor I and the comparison with the experimentally determined rotor efficiency shows approximately the same difference in efficiency of from 0.02 to 0.03.

To sum up, it may be stated that if the theoretically calculated efficiency is reduced on account of clearance losses (tip clearance 1 mm = 0.04 in.) by 0.02 to 0.03, the rotor efficiency as well as the average total pressure rise of the rotor can be accurately predicted.

The determination of the total head increase of the entire fan requires the inclusion in the calculations of the stator and diffuser losses in addition to the rotor loss. Figure 31 (see also table 4 for $\delta_1 = 27.5^\circ$) shows the results for rotor III and stator I of figure 32 (see

also table 5 for $\frac{s}{2r_a} = 0.002$) and for rotor III and

stator II. The differences in the individual curves are proportional to the energy losses in the correspondingly identified parts of the fan. The rotor loss was calculated by means of the formulas of section IV without regard to the additional clearance or hub losses. The same holds for the stator. The diffuser loss was assumed in both cases at 15 percent of the theoretical pressure equivalent of the axial velocity. Lastly, the tip clearance losses were inserted from figure 30. Curve η' represents the total efficiency obtained by this method. The agreement with the experimentally determined efficiency, the test points of which are denoted by circles, is better in figure 31 than in figure 32. A number of plausible reasons can be given for the deviations: First, the efficiency of the hub diffuser was arbitrarily assumed. It may be supposed that its efficiency is better behind stator I, the thin circular arc blades of which cause thin wakes, than behind stator II with its relatively thick blade profiles. Besides, the hub diffuser efficiency is not necessarily constant over the whole operating range. It may be assumed that a rotation behind the stator lowers the efficiency of the "inner diffuser" (contrary to reference 9). An additional loss is further effected by the hub flow on the stator walls,

which surely depends on the strongly varying stream direction of the stator blades. The experiments of Christiani and Keller (references 5 and 8) on stationary cascades indicate that this loss is greater for stator II than for stator I. Lastly, the pressure measurements themselves are in error, due to the residual rotation and the non-uniformity of the axial exit velocity, in such a way that the measured total head increase is somewhat smaller than the actual one.

An attempt might be made to apportion the difference between η_{th} and η_g among the possibilities indicated. But the data available at present are few to allow a division with any claim to reliability. Summing up, it may be said, therefore, that a definite uncertainty still remains in the calculation of the total output of a fan.

Individually, however, significant conclusions can be drawn from the distribution of the losses of figures 31 and 32. The predominating effect of the diffuser losses at large throughflow coefficients is surprising. This comparatively large share of the diffuser losses is less a result of the increase of diffuser losses with increasing throughflow volume than of the simultaneous decrease of the rotor total pressure boost. Figure 31 indicates a strong increase of energy losses for stator I at $\bar{\varphi}_0 < 0.44$. The flow along stator I has separated for these operating conditions. A comparison with the measured efficiency curve of figure 31 shows this tendency quite plainly in the total efficiency. On the whole, it is evident from figure 31 that stator I is not entirely suitable for rotor III, since the operating range for minimum losses occurs at too great quantities of flow. In contrast, stator II is substantially more favorable.

Reverting to the discussion of the point at which separation occurs, it has already been mentioned that a decrease in throughflow coefficient is accompanied by an increase in angle of attack. At rotors I and II the maximum lift $\zeta_{A_{max}}$ occurs first at the outer sections, according to figures 25 and 26 - that is, the throughflow distribution on rotor I can still be definitely determined for the average $\bar{\varphi}_0 = 0.324$. The method diverges for a smaller average throughflow coefficient. The critical mean coefficient for rotor II is $\bar{\varphi}_0 = 0.273$. Contrariwise, on rotor III $\zeta_{A_{max}}$ is exceeded first at the hub

sections. The critical mean coefficient for the distribution calculation is $\bar{\varphi}_0 = 0.301$. The pressure-quantity curves for the three rotors are represented in figure 33. It is evident that for rotors I and II the flow separates at throughflow coefficients sufficiently close to those given previously, while for rotors III the flow adheres down to $\bar{\varphi}_0 = 0.245$. The total efficiency curve (figs. 31 and 32) is, in fact, steeper for $\bar{\varphi}_0 < 0.3$ than for $\bar{\varphi}_0 > 0.3$, but the steady increase of the curve $\bar{\psi}(\bar{\varphi}_0)$ proves that the flow can not properly be said to have separated as yet. These facts lead to the conclusion that exceeding $\zeta_{A_{max}}$ at the hub sections does not have the same significance as at the outer sections. It therefore remains to be proved whether the separation of flow at $\bar{\varphi}_0 = 0.245$ can be correlated with exceeding $\zeta_{A_{max}}$ at the outer sections.

For this purpose figure 27 is used again. Although, as has been explained earlier, an increased solidity λ shifts the point of separation of the outer sections toward lower throughflow velocities, this fact alone is not sufficient to explain the preservation of a stable flow condition down to $\bar{\varphi}_0 = 0.245$. Figure 27 shows that $\zeta_{A_{max}}$ is already exceeded at $\varphi_0 = 0.29$ on the outer section. But, remembering that the throughflow velocity on rotor III is appreciably higher near the outer wall than the mean throughflow velocity; it can, in fact, be proved that separation of flow alone at the outer profiles causes separation of the entire rotor flow. Since the iteration procedure for the distribution calculation fails for $\bar{\varphi}_0 < 0.3$ because of the difficulties at the hub profiles, there remains only extrapolation with which to determine the increase of throughflow velocity near the outer wall for the mean throughflow $\bar{\varphi}_0 = 0.245$. To this end $\varphi_0(R=0.96) - \bar{\varphi}_0$ was plotted against φ_0 in figure 34 for the three rotors. The experimentally determined critical throughflow coefficients at which the rotor flow separates are indicated by dot-dash lines parallel to the ordinate axis. For rotors I and II the quantity $\varphi_0(R=0.96) - \bar{\varphi}_0$ lies on a straight line up to near the separation point. Assuming the same for rotor III the extrapolation (dotted line) gives for $\varphi_0(R=0.96) = 0.288$ the value $\bar{\varphi}_0 = 0.245$. This coefficient is, then, approximately attained in the section near the outer wall when rotor flow separation occurs. As is seen from figure 27, this is exactly the value at which the section efficiency falls steeply.

In point of fact, tuft observations indicated that separation always sets in first at the outer wall. Subsequent to separation the flow reverses in such a way that comparatively quiet flow with large axial velocity prevails near the hub, while the flow reverses toward the outside. For the rest it may be noted that at rotor flow separation all the peculiarities known from polar measurements arose above the $\zeta_{A_{max}}$; that is to say, prolongation by cautious throttling, later readhesion of flow upon reduction of throttling.

The conclusion from the foregoing considerations of experiment and theory, the latter being valid only for $\Phi_0 > 0.3$, is that the outer section alone is responsible for the breakdown of the entire rotor flow. The reliability of this method is checked hereinafter by a consideration of the physical processes of the experiment: The boundary-layer flow on a rotor blade is illustrated in figure 15. The strong deflection of the boundary layer on the suction side near the hub is clearly evident. This process presumably is caused by the combined action of the centrifugal force on the boundary layer, together with the hub flow mentioned at the close of section V. In its net effect on the main flow it is about equivalent to a boundary-layer suction at the sections near the hub. The deflection of the boundary-layer flow apparently is stronger with increasing boundary-layer thickness, and thus effects a stabilization of flow above the $\zeta_{A_{max}}$ value of the isolated section. At the same time, the glide angle ϵ does not increase as much as on the isolated section. A direct consequence is that the efficiency of the sections near the hub itself does not drop as rapidly as figure 27 indicates. The reason for the failure of the throughflow distribution calculation also emerges, and the extrapolation made above is in fact reliable.

The question now arises as to why this stabilization of flow does not show up at the outer sections, and why a substantial outward deflection of flow for these sections could not be observed at all. The basis for a deflection of boundary-layer flow is naturally a minimum boundary-layer thickness, which can only be exceeded on the suction side. But in the outer parts of the blade, centrifugal force and hub flow (see sec. V) work against each other, so that the net effect precisely cancels out.

To prevent misconceptions the following should be noted: The rotor flow separation discussed here has nothing to do with the stability condition

$$\eta - \frac{1}{R^2} \left(\frac{\psi}{2\eta} + \delta_1 \right) > 0 \quad \text{set up at the close of section VI.}$$

In the case in point $\delta_1 = 0$, and the expression vanishes for $\eta = \frac{1}{R^2} \frac{\psi}{2\eta}$. As is easily ascertained from figure 27,

η must assume the value 0.51. For such an efficiency, however, the process of flow separation is already far advanced.

The following may be said by way of summary: If several rotors have been designed for the same operating point, the one the blade chord of which increases most strongly toward the outside will achieve the lowest throughflow coefficient. It is to be supposed that the blade chord increase of rotor III does not as yet represent the best in this respect. Naturally, the total head boost becomes more nonuniform for rotors with blade chord increasing outwardly, the greater is the deviation from the design operating condition. But this is of secondary importance on fans designed to operate over a large throttling range.

A different plot of the fan characteristic is chosen to bring out the greater throttling achieved by rotor III as compared with rotors I and II. The flow resistances to be overcome by a given fan are proportional to the square of the throughflow velocity. The magnitude of the proportionality factor is a direct measure of the throttling strength. Setting $\bar{\psi} = \frac{1}{\sigma_0} \varphi_0^2$ it follows from these considerations that σ_0 is inversely proportional to the throttling, and decreases with increasing throttling. Figure 35 gives the curves $\bar{\varphi}$ and η_g as functions of σ_0 . It is evident that the maximum attainable throttling with rotor III is about twice as great as with rotor I. It follows from the definition of the throttling coefficient $\sigma_0 = \frac{\varphi_0^2}{\bar{\psi}}$ that $\sigma_{0\min}$ can be reduced by decreasing $\bar{\varphi}_{0\min}$ as well as by increasing $\bar{\psi}_{\max}$. Figures 25 to 27 or 31 show that both measures may be used in the rotor family I to III.

Figure 35 shows a small efficiency decrease of rotor III as compared with rotor I. This is largely due to the fact that the actual exit energy is greater than the measured exit energy when the axial exit velocity is not constant over the whole cross section and has a residual rotation.

VIII. FURTHER EXPERIMENTAL RESULTS

Another rotor, in addition to rotors I to III, was experimentally investigated. The design of rotor III specified a mean throughflow coefficient $\bar{\varphi}_0 = 0.45$ and a pressure coefficient $\bar{\psi} = 2.2$. The model had 13 blades with profile chords increasing toward the outside. The rotor data are given in figure 36 and table 3. Since the blades on all rotors were adjustable, the pressure-quantity curves could be measured for various blade angles. The blade setting is defined by the blade angle $\delta_1(R=0.96)$ of the profile at $R = 0.96$. The angle δ_1 used in the theory is related to the angle of incidence δ by $\delta = 90^\circ - \delta_1$. Stator I was used in the tests with the first of the three rotors, and stator II with rotor IV; and the same stator was retained for all the blade angles, although still more favorable results could have been achieved by the use of different stators, each suited to a particular blade angle. The measurements were made at rotational speeds ranging between 1700 to 2500 rpm. Figures 37 to 40 give the test results in graphic form, while table 4 contains the corresponding numerical values.

The foregoing investigations (table 3) disclosed the need for the inclusion of the clearance losses in the rotor calculation. To obtain a somewhat more reliable foundation for it, rotor III with blade angle $\delta_1(R=0.96) = 27.5^\circ$ was progressively turned down, the clearance between blade and outer wall being correspondingly enlarged. The performance of rotor III in combination with stator II was measured at every step. The measured results are plotted against σ_0 in figure 41, since, according to the previous discussions, not only the efficiency but also the maximum attainable throttling must depend on the clearance. The numerical values are given in table 5. The reduction in efficiency is most apparent. The

efficiency is plotted against the ratio $s/2r_a$ in figure 42 for the throttling coefficients $\sigma_0 = 0.32, 0.64,$ and $1.14,$ where s is the clearance, and $2r_a$ is the original rotor diameter (500 mm). The efficiencies are readily ex-

trapolated to zero clearance since $\eta\left(\frac{s}{2r_a}\right)$ can be represented sufficiently exactly by a straight line. There is an efficiency reduction of 0.02 to 0.03 for the normally

existent clearance $\frac{s}{2r_a} = 0.002.$ It is of the same order

of magnitude as that determined previously by altogether different means. Simultaneously with the reduction in efficiency, there is an increase of $\sigma_{0\min}$ with clearance increase. The dotted line connecting the maximums of the Ψ curves in figure 41 gives $\sigma_{0\min}.$ In contrast to the linear dependence of efficiency on clearance, there is a greater change in $\sigma_{0\min}$ for small clearances than for larger ones.

Translation by Wm. Mutterperl,
National Advisory Committee
for Aeronautics.

REFERENCES

1. Joukowsky, N.: Theorie tourbillonnaire de l'hélice propulsive. Gauthier-Villars (Paris), 1929.
2. Lamb, Horace: Hydrodynamics. The University Press (Cambridge, Eng.), 5th ed., 1924.
3. Betz, Albert: Diagrams for Calculation of Airfoil Lattices. NACA TM No. 1022, 1942.
4. Weinig, F.: Die Strömung um die Schaufeln von Turbomaschinen. J. A. Barth (Leipzig), 1935.
5. Christiani, K.: Experimentelle Untersuchung eines Tragflügelprofils bei Gitteranordnung. Luftfahrtforschung, Bd. 2, Heft 4, Aug. 1928, pp. 91-110.
6. Walchner, O.: Berechnung von Luftschauben mit kleinem Schubbeiwert und kleinem Fortschrittsgrad (Hubschrauben). Luftfahrtforschung, Bd. 13, Nr. 4, April 1936, pp. 103-110.
7. Gutsche, F.: Kennwerteinflüsse bei Schiffsschrauben-Modellversuchen. Jahrb. der Schiffbautechnischen Gesellschaft Berlin, Bd. 37, 1936, p. 277.
8. Keller, C.: Axialgebläse vom Standpunkt der Tragflügeltheorie. Eidgenössische Tech. H.S. Zürich, Institut für Aerod. (Rep. 2), 1934.
9. Peters, H.: Conversion of Energy in Cross-Sectional Divergences under Different Conditions of Inflow. NACA TM No. 737, 1934.
10. Flachsbart, O.: Messungen an ebenen und gewölbten Platten. IV. Lfg, no. 11, pp. 96-100 of Ergebnisse der Aerodynamischen Versuchsanstalt zu Göttingen, L. Prandtl and A. Betz, ed., R. Oldenbourg (München und Berlin), 1932.

FIGURE LEGENDS

Figure 1.- Definition of the performance of a rotor blade element.

Figure 2.- The axial velocities induced in the plane $x = 0$ by a trailing ring vortex element are doubled by geometric reflection in this plane, all other velocity components being canceled.

Figure 3.- A ring of cross section $dxdr$, which intersects an axial cascade, cuts an element $dsdr$ out of each blade, and $dx = ds \cos \beta$.

Figure 4.- An element on the pressure side, of unit length radially, exerts an axial force $dS_d = -p_d |d(r\theta_d)|$

on the fluid. Since $|d(r\theta_d)| = -\frac{\partial(r\theta_d)}{\partial x} dx$ then

$\frac{\partial S_d}{\partial x} = p_d \frac{\partial(r\theta_d)}{\partial x}$. Correspondingly, for a suction-side

element, $\frac{\partial S_s}{\partial x} = -p_s \frac{\partial(r\theta_s)}{\partial x}$.

Figure 5 (left).- Velocity diagram of cascade flow.

Figure 6 (right).- Resolution of forces on a section in cascade.

Figure 7.- Diagram I for the calculation of rotor section characteristics. The family of curves $|K| = \lambda' |\zeta_{Ag}|$

$\left(1 + \frac{\epsilon}{\cot \beta}\right)$ is given in the diagram. The stream

direction at the location of the section, defined by the angle β , is given by the family of straight lines all going through the point $X = 0, Y = 4$. The line for $\beta = \beta_0$ intersects the x -axis in the point $X = \cot \beta, Y = 0$. (For very large $\cot \beta_0$, the straight lines cut the ordinate line $X = 0.5$, which has the scale $\tan \beta$, in the point $\tan \beta = \tan \beta_0$.) -

For a given section, then, since $\beta = \delta + \alpha$, the parameter K is known as a function of β from the section polars. The operating point X, Y is given as the intersection of the straight line $\beta = \beta_0$ and

the corresponding curve $K = K(\beta_0)$. - If an operating point X_0, Y_0 is given, then the corresponding values of $\cot \beta_0$ and $K(\beta_0)$ can be taken from the diagram. After a choice of λ' , ζ_{Ag} and thence the angle of attack α are obtained by iteration. The scale $1 - \frac{Y}{2}$ gives the tangential velocity relative to the rotor as a fraction of the entrance rotation:

$$\frac{w_{u_2}}{r\omega} \frac{1}{\delta_1^*} = \frac{w_{u_2}}{w_{u_1}} = 1 - \frac{Y}{2}$$

Figure 8.- Diagram II for the calculation of rotor efficiency: The solid line ellipses are the curves $f_1 = \text{constant}$, the dotted ellipses are the curves $f_2 = \text{constant}$. The efficiency is

$$\eta = 1 + \frac{\delta_1^*}{\frac{1}{\epsilon} f_1 + f_2}$$

Figure 9.- Diagram III for the calculation of section characteristics of stationary guide vanes: The diagram gives the family of curves $|K| = \lambda' \left| \zeta_{Ag} \left(1 + \frac{\epsilon}{\cot \beta} \right) \right|$. The stream angle β at the location of the section is given by the family of parallel lines of slope $\frac{Y^* - Y_0^*}{X^* - X_0^*} = 4$, and the line for $\beta = \beta_0$

intersects the X^* -axis in the point $X^* = \tan \beta_0$. For a given section then, since $\beta = \delta + \alpha$, the parameter K is known as a function of β from the section polars. The operating point X^*, Y^* is the intersection of the straight line $\beta = \beta_0$ with the corresponding curve $K = K(\beta_0)$. If an operating point X_0^*, Y_0^* is given initially, then the corresponding $\tan \beta_0$ and $K(\beta_0)$ can be taken from the diagram. After choosing λ' , ζ_{Ag} and thence the angle of

attack α are calculated by iteration. The dotted line denotes the operating points with no rotation at exit. If a straight line is drawn through the operating point and the origin, the intersection of this line with the scale f_3 gives the exit rotation in fractions of the entrance rotation:

$$\frac{c_{u2}}{rw} \frac{1}{\phi_1^*} = \frac{w_{u2}}{w_{u1}} = f_3$$

Figure 10.- Diagram IV for the calculation of the energy losses of guide vanes:

$$\Delta\psi^* = \lambda \zeta_w (\varphi^*)^2 f_4$$

Figure 11.- Coordinates for the calculation of the thickness correction.

Figure 12.- The profile angle of attack for pump cascades is lowered by the disturbance velocity due to finite blade thickness.

Figure 13.- The profile angle of attack for turbine cascades is increased by the disturbance velocity due to finite blade thickness.

Figure 14 (right).- Schematic representation of the origin of the secondary flow for stationary cascades with end plates.

Figure 15 (below).- Boundary layer flow in a blower rotor. The dotted lines denote the corresponding cylindrical sections.

Figure 16.- Sketch of the blower test stand.

Figure 17.- Blade of the eight-blade rotor I. (See table I.)

Figure 18.- Blade of the eight-blade rotor II. (See table I.)

Figure 19.- Blade of the eight-blade rotor III. (See table I.)

Figure 20.- Blade of the nine-blade stator I. (See table 2.)

Figure 21.- Blade of the nine-blade stator II. (See table 2.)

Figure 22 (lower right). ——— Cascade coefficient k for rotors I, II, and III. — — — Finite blade thickness coefficient $D\lambda^2$.

Figure 23.- Section characteristics for rotor III: — — — for $k = 1$, $D = 0$; — — — for $D = 0$, but taking the cascade coefficient k of figure 22 into account.

Figure 24.- Section characteristics for rotor III: — — — takes into account the cascade coefficient of figure 22 but $D = 0$ (see fig. 23); ——— takes into account the cascade coefficient k and the thickness correction $D\lambda^2$ of figure 22.

Figure 25.- Section characteristics for four sections of

rotor I. ——— + ——— + $\frac{r}{r_a} = 0.96$; ——— $\frac{r}{r_a} = 0.80$;
 ——— . ——— . $\frac{r}{r_a} = 0.64$; ——— $\frac{r}{r_a} = 0.52$. The thick

cross lines denote the operating points of the individual sections operating together.

Figure 26.- Section characteristics for four sections of

rotor II: ——— + ——— + $\frac{r}{r_a} = 0.96$; ——— $\frac{r}{r_a} = 0.80$;
 ——— . ——— . $\frac{r}{r_a} = 0.64$; ——— $\frac{r}{r_a} = 0.52$. The thick

cross lines denote the operating points of the individual sections operating together.

Figure 27.- Section characteristics for four sections of

rotor III: ——— + ——— + $\frac{r}{r_a} = 0.96$; ——— $\frac{r}{r_a} = 0.80$;
 ——— . ——— . $\frac{r}{r_a} = 0.64$; ——— $\frac{r}{r_a} = 0.52$. The thick

cross lines denote the operating points of the individual sections operating together.

Figure 28.- Distribution of total head increase for rotor

I: $\left[\delta_1 \left(\frac{r}{r_a} = 0.96 \right) = 31^\circ \right]$: ——— from experiment and
 ——— from theory.

Figure 29.- Distribution of total head increase for rotor

III: $\left[\delta_1 \left(\frac{r}{r_a} = 0.96 \right) = 27.5^\circ \right]$: ——— from experiment
 and ——— from theory.

Figure 30 (left).- Average rotor characteristics for

rotor III $\left[\delta_1 \left(\frac{r}{r_a} = 0.96 \right) = 27.5^\circ \right]$ — — • — — measured
 torque curve, — — • — — measured total head curve and
 measured efficiency, ——— theoretical mean curves.

Figure 31 (right).- Blower characteristic for rotor III

$\left[\delta_1 \left(\frac{r}{r_a} = 0.96 \right) = 27.5^\circ \right]$ and stator I. The experimen-
 tally determined points are denoted by zero circles.
 (See table 4.)

Figure 32.- Blower characteristic for rotor III

$\left[\delta_1 \left(\frac{r}{r_a} = 0.96 \right) = 28^\circ \right]$ and stator II. The experimen-
 tally determined points are denoted by zero circles.
 (See table V for $\frac{s}{2r_a} = 0.002$.)

Figure 33.- Pressure-quantity curves for the blower in-
 stallations: Rotor I, II, and III each with exit guide
 vanes I. (Blade angles in accordance with figs. 17 to
 19.)

Figure 34.- Extrapolation of the throughflow coefficients

for the section $\frac{r}{r_a} = 0.96$ from the mean throughflow coefficients for which the tests indicate separation of the rotor flow.

Figure 35.- Experimentally determined blower characteristics for the blower unit: Rotor I, II, and III with stator I downstream, as a function of the throttling coefficient σ_0 . The rotor blade angles correspond to figures 17 to 19. (See table 4.)

Figure 36.- Blades of the 13-blade rotor IV. (See table 3.)

Figure 37. Experimental blower characteristics for rotor I and exit stator I at various rotor blade angles. (See table 4.)

Figure 38.- Experimental blower characteristics for rotor II and exit stator I at various rotor blade angles. (See table 4.)

Figure 39.- Experimental blower characteristics for rotor III and exit stator I at various rotor blade angles. (See table 4.)

Figure 40.- Experimental blower characteristics for rotor IV and exit stator II at various rotor blade angles. (See table 4.)

Figure 41 (left).- Experimental blower characteristics for rotor III and exit stator II for various clearances between rotor blade and housing.

Figure 42 (right).- Experimentally determined reduction in efficiency of rotor III and stator II with increasing tip clearance.

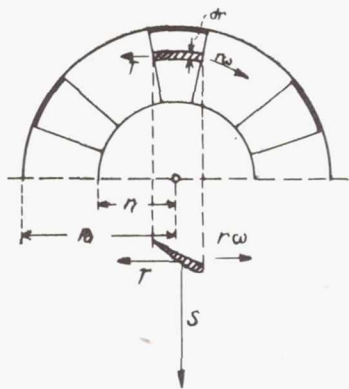


Figure 1.- Definition of the performance of a rotor blade element.

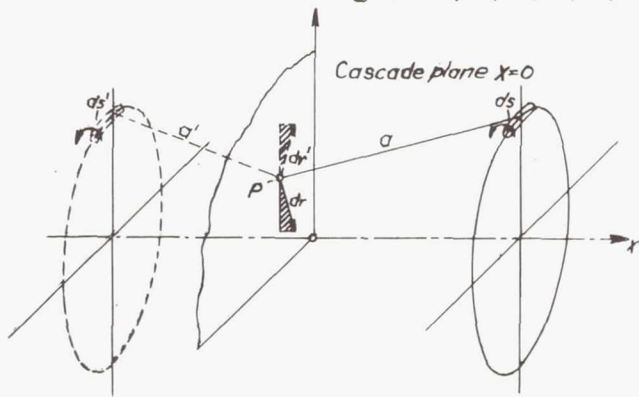


Figure 2.- The axial velocities induced in the plane $x = 0$;

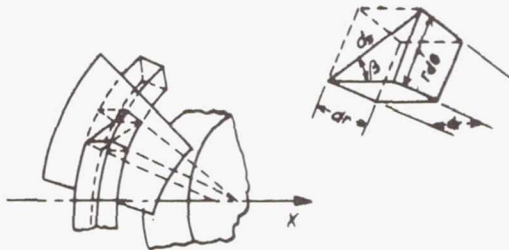


Figure 3.- A ring of cross section $dx dr$;

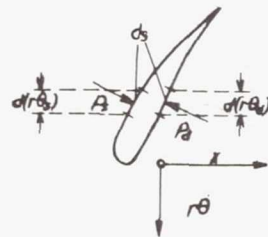


Figure 4.- An element on the pressure side, of unit length radially;

(A list of complete legends is given at end of text.)

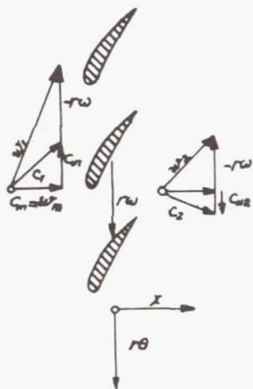


Figure 5.- Velocity diagram of cascade flow.

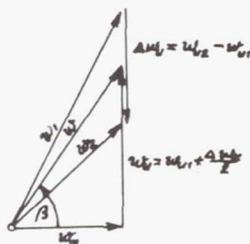


Figure 6.- Resolution of forces on a section in cascade.

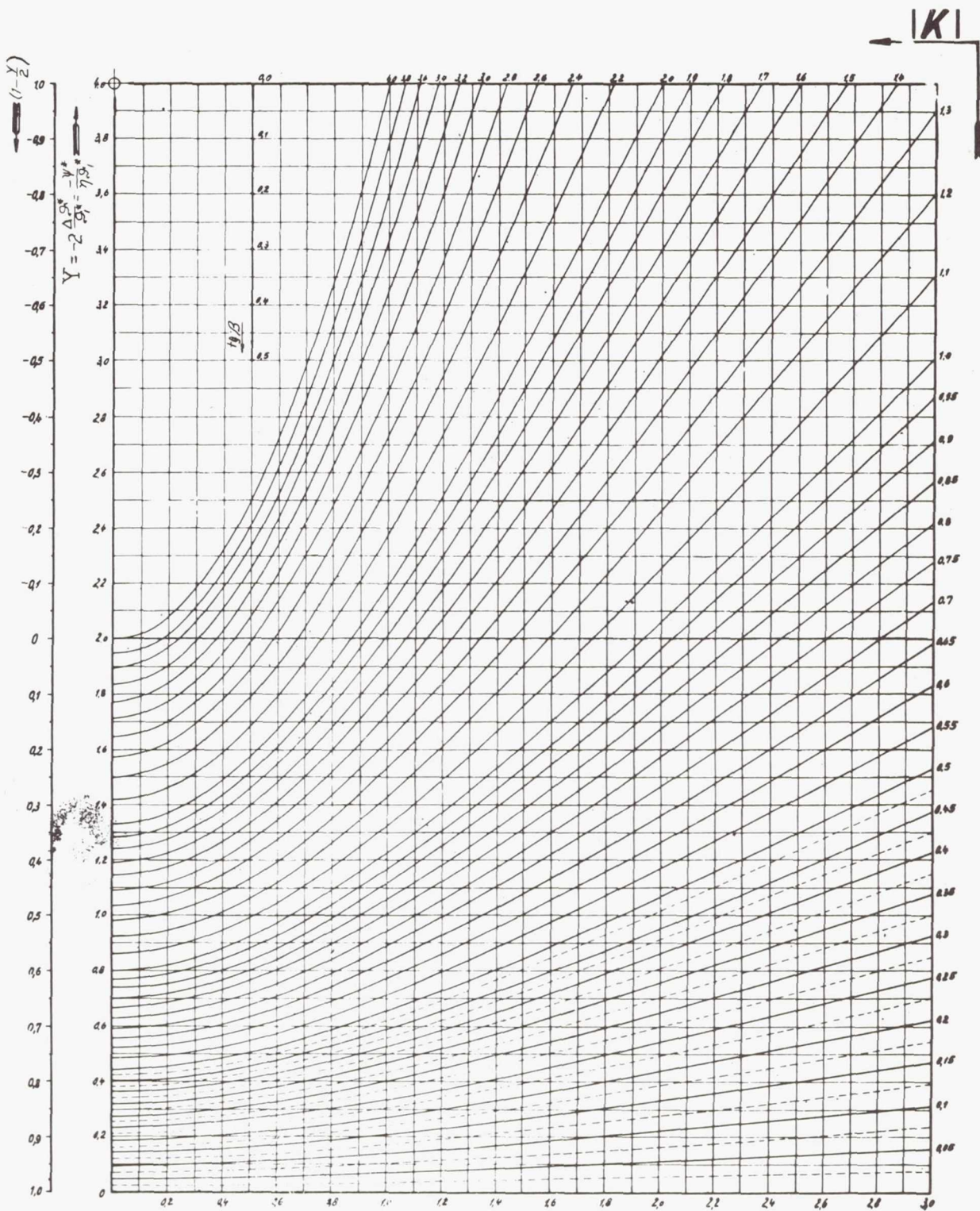


Figure 7.- Diagram I for the calculation of rotor section characteristics;

96

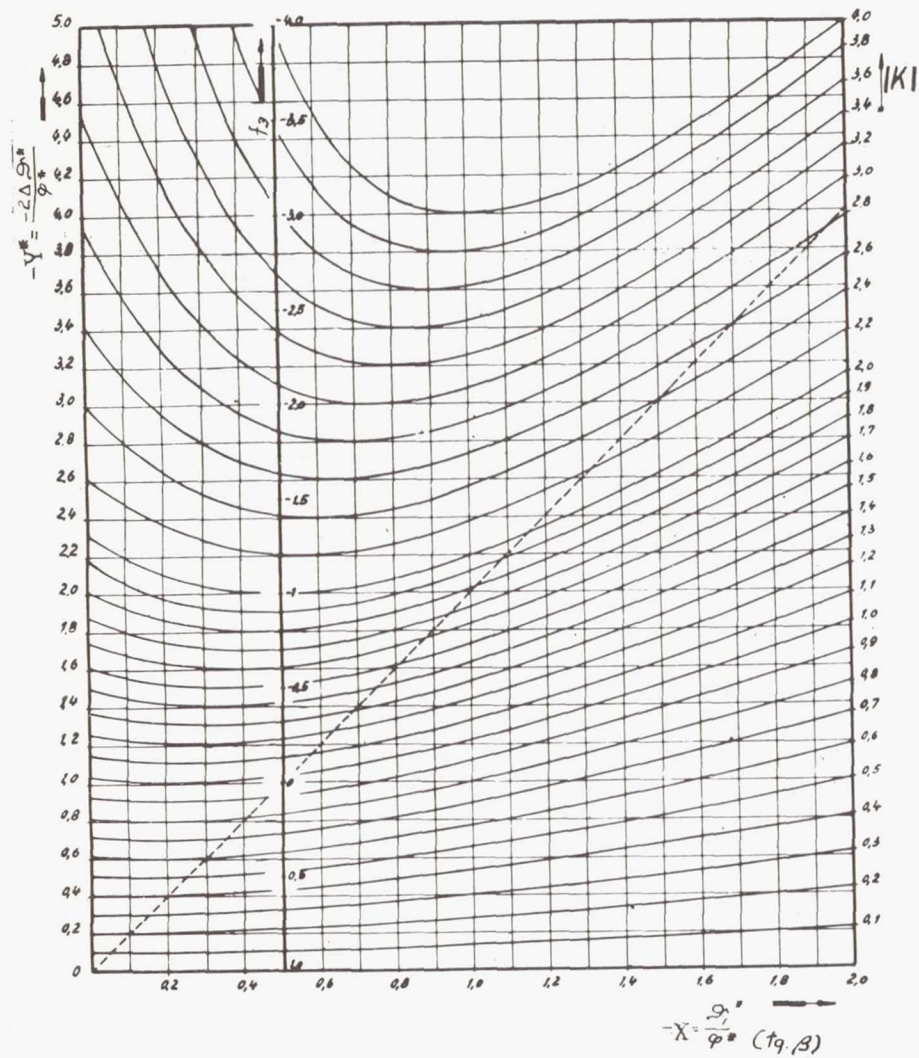


Figure 9.- Diagram III for the calculation of section characteristics of stationary guide vanes;

88

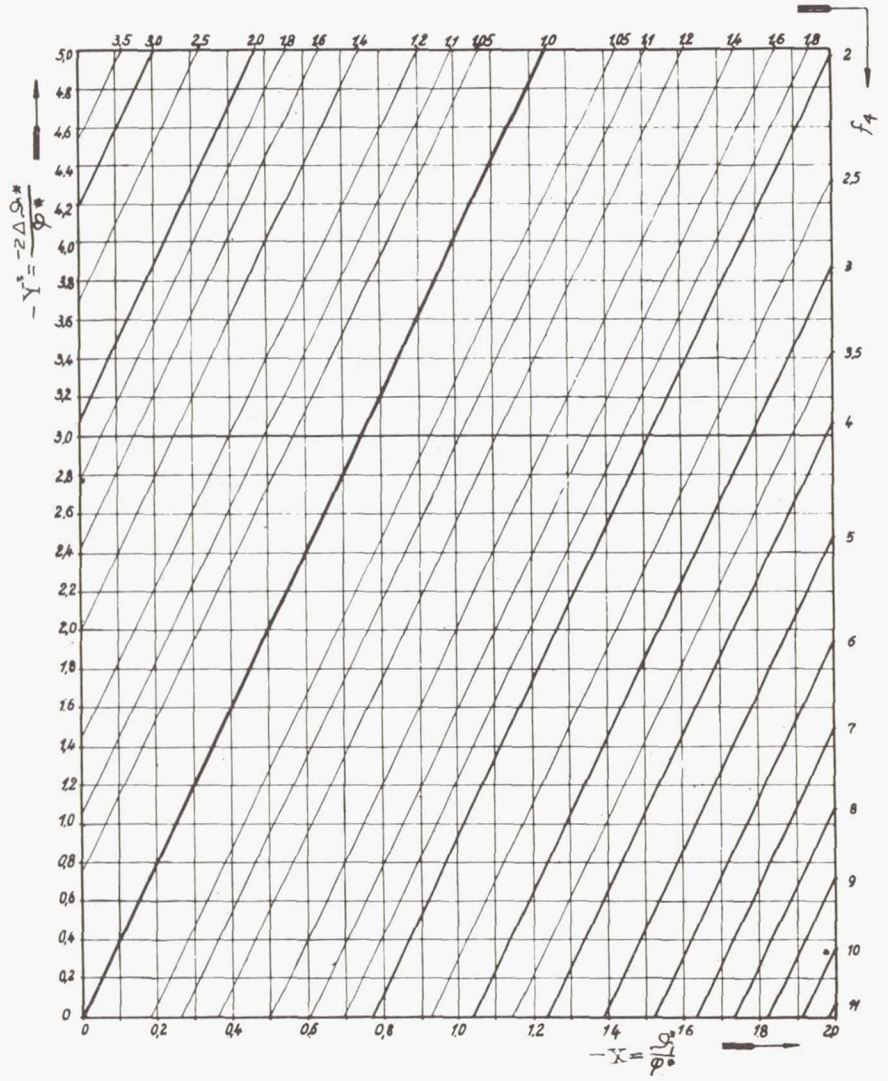


Figure 10.- Diagram IV for the calculation of the energy losses of guide vanes;

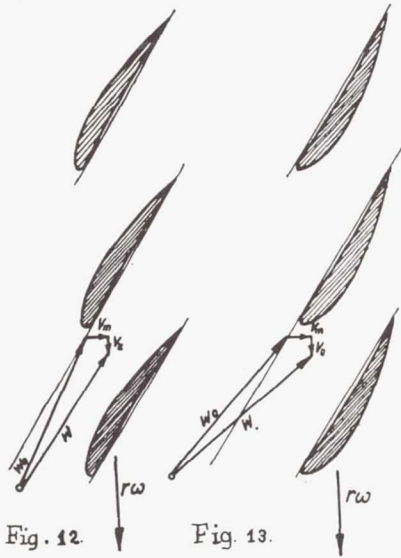
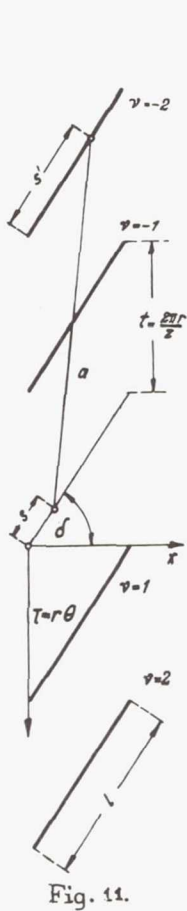


Fig. 12.

Fig. 13.

Figure 11.- Coordinates for the calculation of the thickness correction.

Figure 12.- The profile angle of attack for pump cascades is lowered by the disturbance velocity due to finite blade thickness.

Figure 13.- The profile angle of attack for turbine cascades is increased by the disturbance velocity due to finite blade thickness.

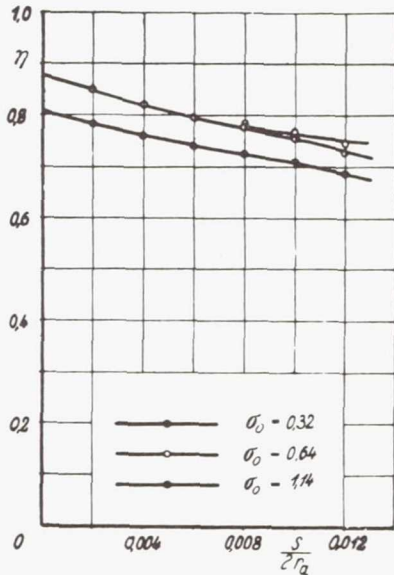


Figure 42.- Experimentally determined reduction in efficiency of rotor III and stator II with increasing tip clearance.

Section A-B

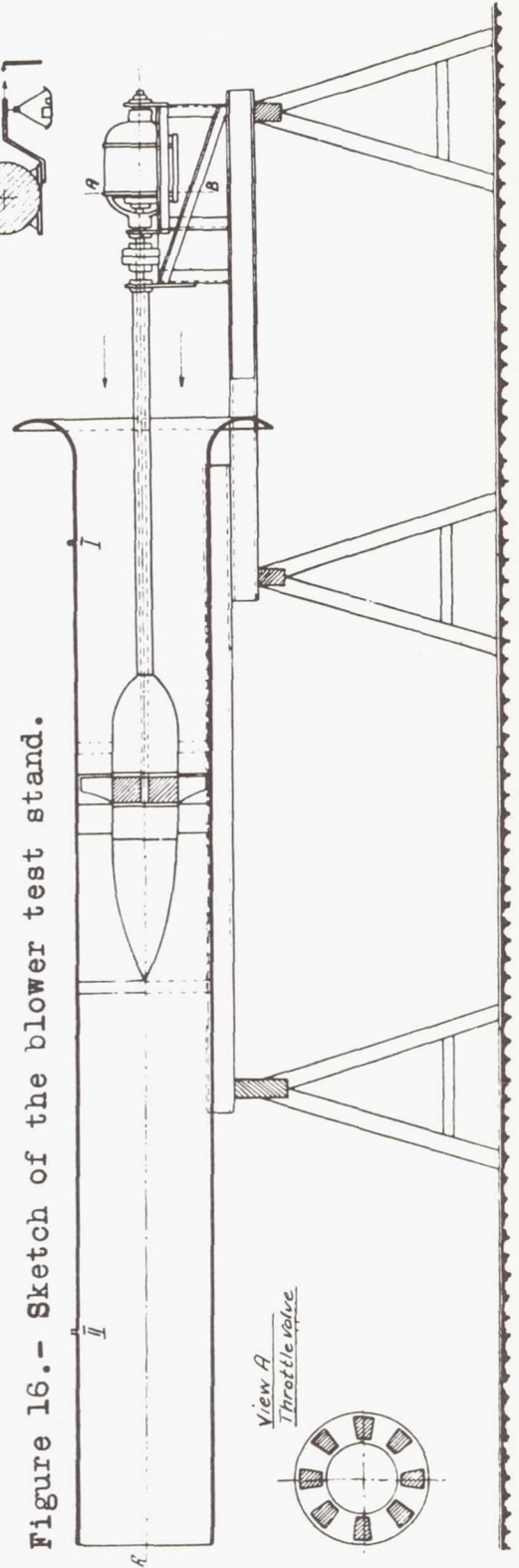


Figure 16.- Sketch of the blower test stand.

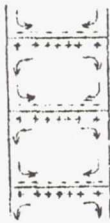


Figure 14.- Schematic representation of the origin of the secondary flow for stationary cascades with end plates.

Figure 15.- Boundary layer flow in a blower rotor. The dotted lines denote the corresponding cylindrical sections.

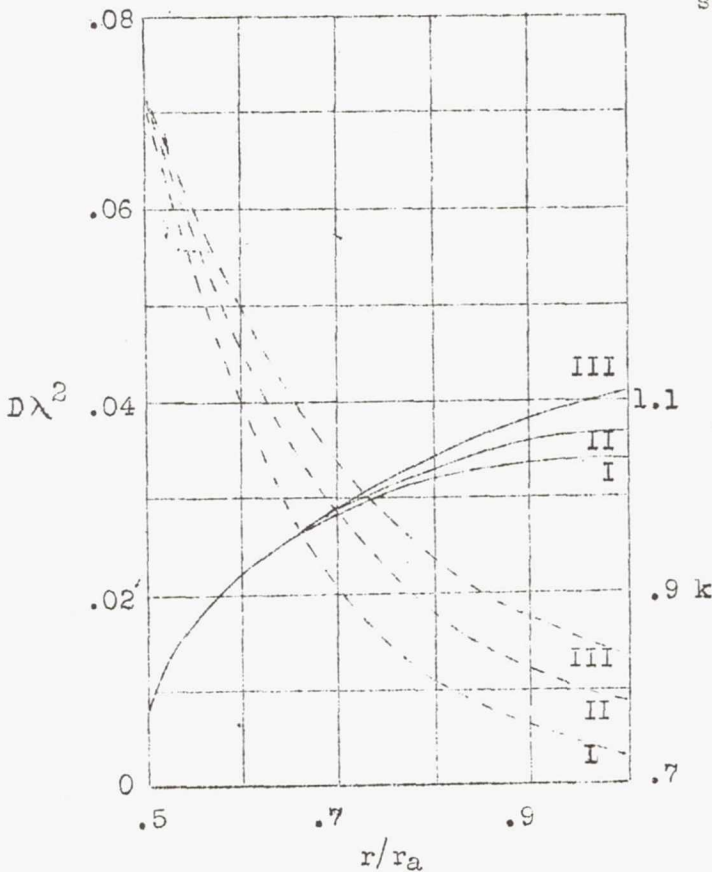
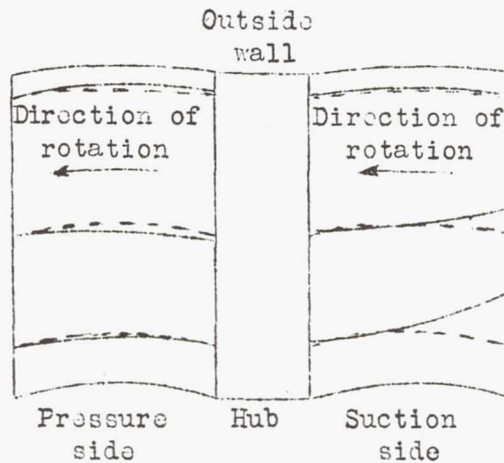


Figure 22.-
 ——— cascade coefficient k for rotors I, II, III.
 - - - finite blade thickness coefficient, $D\lambda^2$.

100

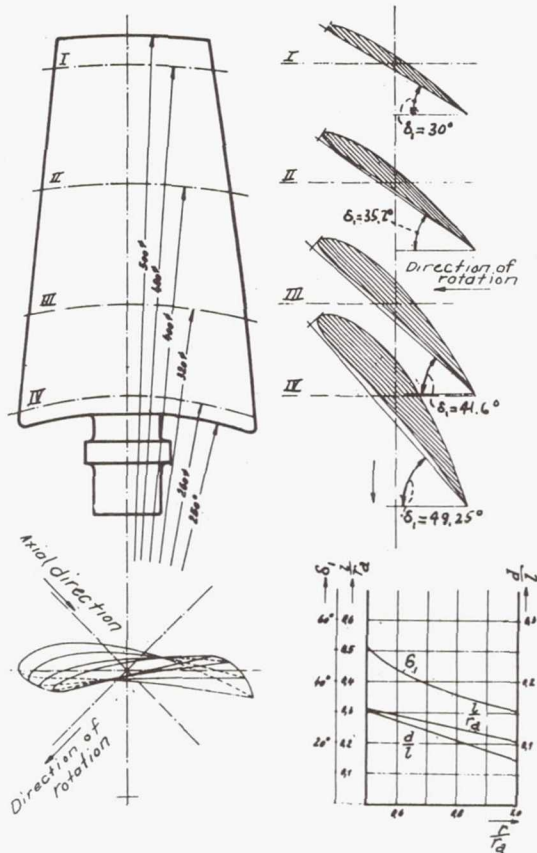


Figure 17.- Blade of the 8-bladed rotor I (see table 1).

Table 1.
8 bladed rotor I.

$\frac{r}{r_a}$	l	$\frac{d}{l}$	$\delta_1 = 90 - \delta$
0,52	78,80	0,149	49,25°
0,64	72,14	0,128	41,60°
0,80	63,55	0,099	35,20°
0,96	54,50	0,081	30,00°

Profile ordinates

	X	0	1,25	2,50	5,0	7,5	10,0	15,0	20,0	30,0	40,0	50,0	60,0	70,0	80,0	90,0	95,0	100
$\frac{r}{r_a} = 0,52$	Y_o	4,70	7,44	9,00	10,22	12,30	13,45	13,78	15,58	17,08	16,70	15,58	13,80	11,30	8,20	4,57	2,52	0,45
	Y_u	4,70	2,79	2,05	1,52	1,27	1,31	1,32	1,65	2,17	2,54	2,70	3,05	1,64	1,59	0,89	0,39	0
$\frac{r}{r_a} = 0,64$	Y_o	3,74	6,10	7,35	9,20	10,42	11,50	12,80	13,70	14,35	14,03	12,88	11,42	9,25	6,71	3,76	2,08	0,42
	Y_u	3,74	2,41	1,88	1,33	1,12	1,12	1,13	1,26	1,53	1,66	1,72	1,79	1,38	1,03	0,61	0,29	0
$\frac{r}{r_a} = 0,80$	Y_o	2,86	4,64	5,55	6,84	7,74	8,52	9,59	10,22	10,77	10,52	9,58	8,38	6,82	4,87	2,74	1,89	0,31
	Y_u	2,86	1,95	1,48	0,96	0,65	0,63	0,61	0,63	0,87	0,99	1,09	0,94	0,87	0,66	0,31	0,25	0
$\frac{r}{r_a} = 0,96$	Y_o	2,61	3,97	4,70	5,50	6,35	6,83	7,46	7,78	8,08	7,80	7,34	6,43	5,14	3,67	2,17	1,17	0
	Y_u	2,61	1,69	1,30	0,85	0,59	0,37	0,18	0	0	0	0	0	0	0	0	0	0

101

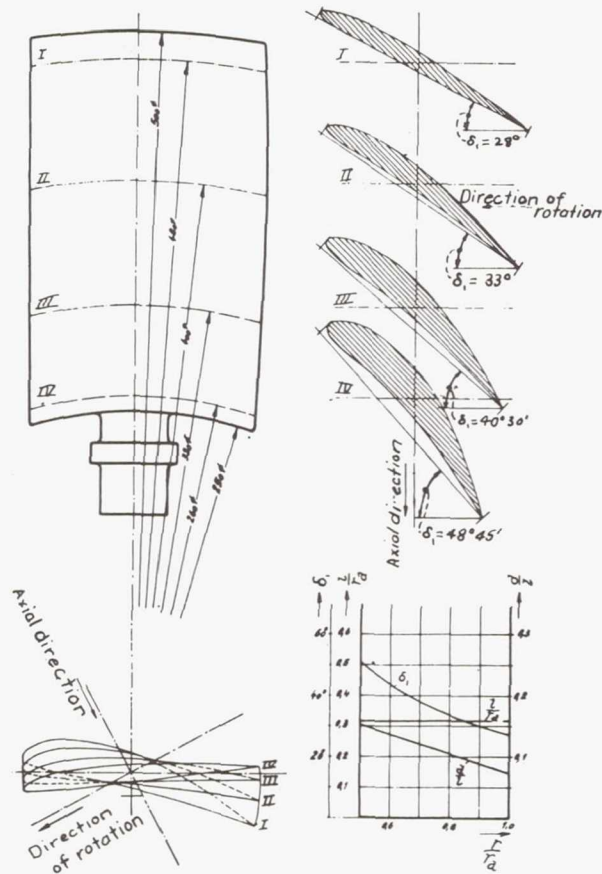


Figure 18.- Blade of the 8-bladed rotor II (see table 1).

Table 1 (continued)
8 bladed rotor II.

$\frac{r}{r_a}$	l	$\frac{d}{l}$	$\delta_1 = 90 - \delta$
0,52	80,74	0,149	48,75°
0,64	80,20	0,130	40,50°
0,80	80,06	0,098	33,00°
0,96	79,50	0,081	28,00°

Profile ordinates

X		0	1,25	2,5	5,0	7,5	10,0	15,0	20,0	30,0	40,0	50,0	60,0	70,0	80,0	90,0	95,0	100
$\frac{r}{r_a} = 0,52$	Y_o	4,78	7,73	9,39	11,62	13,50	14,85	16,91	18,30	19,70	19,70	18,70	16,85	14,21	10,65	6,08	3,40	0,59
	Y_u	4,78	2,94	2,38	2,03	2,04	2,28	3,00	4,22	4,88	5,57	5,82	5,50	4,80	3,75	1,51	1,18	0
$\frac{r}{r_a} = 0,64$	Y_o	3,64	6,49	7,75	9,61	10,30	12,00	13,65	14,70	15,90	15,65	14,60	13,10	10,95	8,10	4,06	2,67	0,54
	Y_u	3,64	2,37	2,05	1,50	1,42	1,47	1,81	2,22	2,86	3,39	3,62	3,45	2,97	2,23	1,37	0,85	0
$\frac{r}{r_a} = 0,80$	Y_o	2,87	4,67	5,63	7,52	8,12	9,00	10,20	10,95	11,50	11,28	10,50	9,25	7,75	5,30	2,77	1,45	0,50
	Y_u	2,87	1,87	2,15	1,25	1,03	1,05	1,25	1,40	1,67	1,87	2,00	1,87	1,60	1,25	0,65	0,35	0
$\frac{r}{r_a} = 0,96$	Y_o	2,31	3,72	4,39	5,44	6,16	6,74	7,53	7,92	8,10	7,75	6,92	5,94	4,74	3,40	1,88	1,13	0,50
	Y_u	2,31	1,53	1,16	0,63	0,38	0,20	0,13	0,08	0	0	0	0	0	0	0	0	0

102

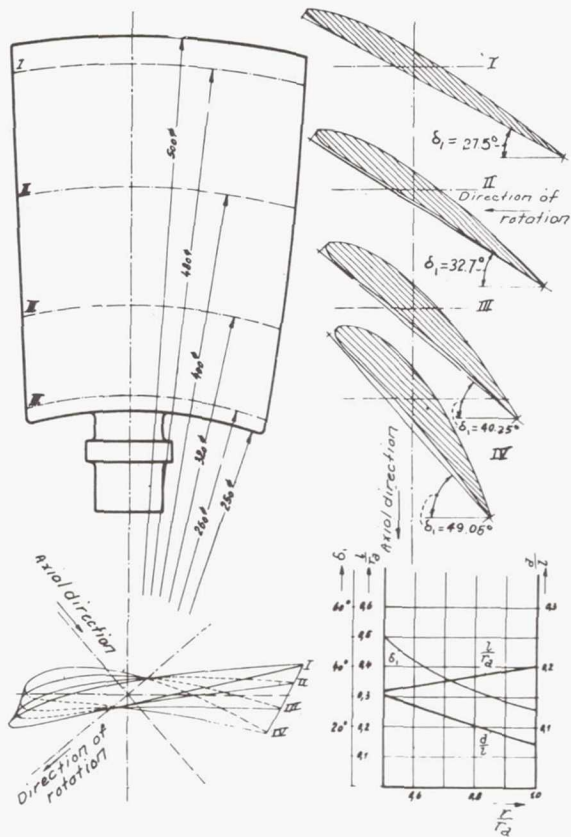


Figure 19.- Blade of the 8-bladed rotor III (see table 1).

Table 1 (continued)
3 bladed rotor III.

$\frac{r}{r_a}$	l	$\frac{d}{l}$	$\delta_1 = 90 - \delta$
0,52	80,70	0,150	49,05°
0,64	85,40	0,129	40,25°
0,80	91,00	0,098	32,70°
0,96	97,80	0,081	27,50°

Profile ordinates

	X	0	1,25	2,50	5,0	7,5	10,0	15,0	20,0	30,0	40,0	50,0	60,0	70,0	80,0	90,0	95,0	100
$\frac{r}{r_a} = 0,52$	Y_o	4,46	7,30	8,69	10,65	12,40	13,50	15,10	16,20	17,20	17,00	15,70	13,80	11,10	8,19	4,58	2,60	0,50
	Y_u	4,46	2,60	1,98	1,44	1,24	1,24	1,61	1,78	2,23	2,73	2,73	2,73	2,35	1,74	0,99	0,50	0
$\frac{r}{r_a} = 0,64$	Y_o	3,77	6,09	7,16	8,90	10,20	11,20	12,65	13,60	14,20	13,90	11,70	11,25	9,14	6,67	3,74	2,22	0,47
	Y_u	3,77	2,11	1,52	0,94	0,70	0,70	0,20	0,33	1,30	1,50	1,60	1,60	1,40	1,20	0,70	0,35	0
$\frac{r}{r_a} = 0,80$	Y_o	2,86	4,84	5,72	6,92	7,90	8,57	9,68	10,20	10,55	10,20	9,50	8,35	6,70	4,94	2,86	1,65	0,44
	Y_u	2,86	1,65	1,32	0,88	0,66	0,59	0,55	0,55	0,77	0,88	0,88	0,77	0,66	0,55	0,44	0,22	0
$\frac{r}{r_a} = 0,96$	Y_o	2,25	3,68	4,41	5,36	6,06	6,61	7,35	7,80	8,08	7,78	7,00	6,02	4,82	3,44	1,97	1,23	0,44
	Y_u	2,25	1,31	0,98	0,61	0,37	0,22	0,08	0	0	0	0	0	0	0	0	0	0

103

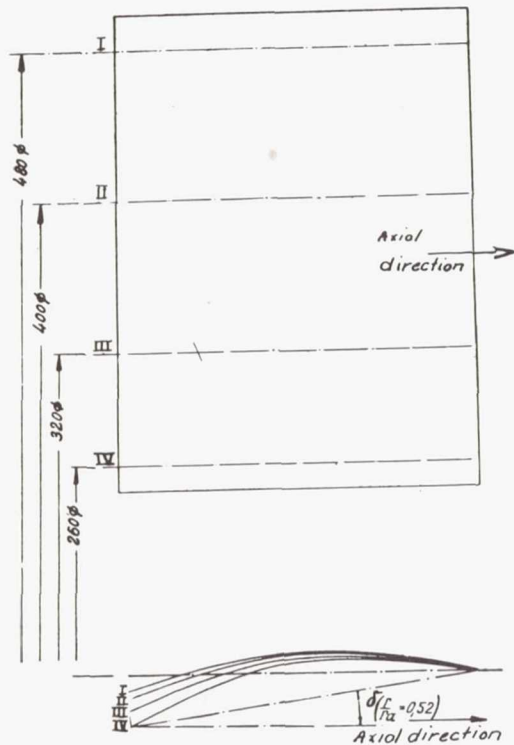


Figure 20.- Blade of the 9-bladed stator I (see table 2).

Table 2.
9 bladed stator I.

$\frac{r}{r_a}$	l	δ
0,52	93,6	8,2°
0,64	93,6	6,3°
0,80	93,8	4,2°
0,96	94,0	3,0°

Profile ordinates

X		0	1,25	2,50	5,0	7,5	10,0	15,0	20,0	30,0	40,0	50,0	60,0	70,0	80,0	90,0	95,0	100
$\frac{r}{r_a} = 0,52$	Y	0	0,75	1,10	1,90	3,0	4,0	5,30	6,80	9,10	10,6	10,9	10,40	8,80	6,50	4,10	2,10	0
$\frac{r}{r_a} = 0,64$	Y	0	0,64	1,10	1,90	2,70	3,30	4,90	6,20	8,30	9,40	9,50	9,00	8,00	6,20	3,30	2,00	0
$\frac{r}{r_a} = 0,80$	Y	0	0,64	0,96	1,60	2,24	3,09	4,48	5,76	7,46	8,53	8,96	8,53	7,46	5,55	3,20	2,03	0
$\frac{r}{r_a} = 0,96$	Y	0	0,64	0,96	1,49	2,24	3,09	4,47	5,54	7,34	8,41	8,52	8,41	7,34	5,54	3,19	1,70	0

104

Figure 21.- Blade of the 9-bladed stator II (see table 2).

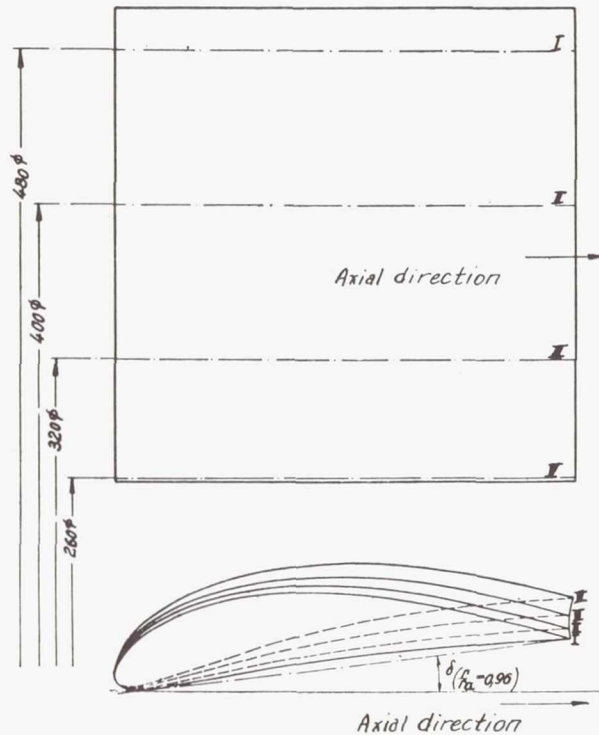


Table 2 (continued)

9 bladed stator II.

$\frac{r}{r_a}$	l	δ
0,52	121,6	12,4°
0,64	119,6	9,5°
0,80	119,6	8,2°
0,96	119,6	6,9°

Profile ordinates

X	0	1,25	2,50	5,0	7,5	10,0	15,0	20,0	30,0	40,0	50,0	60,0	70,0	80,0	90,0	95,0	100	
$\frac{r}{r_a} = 0,52$	Y_o	2,48	6,20	8,35	11,68	12,64	13,90	15,95	17,50	19,00	19,00	18,00	16,05	13,21	9,35	5,04	2,65	0
	Y_u	2,48	0,91	0,25	0	0,41	0,83	1,49	1,90	3,06	3,89	4,30	4,30	3,89	3,06	1,49	0,83	0
$\frac{r}{r_a} = 0,64$	Y_o	2,93	6,53	8,36	10,60	12,38	13,80	15,72	17,05	18,40	18,40	17,20	15,40	12,55	9,20	5,02	2,76	0
	Y_u	2,93	0,84	0,58	0	0,42	0,75	1,17	1,67	2,51	3,18	3,51	3,51	3,18	2,51	1,50	0,84	0
$\frac{r}{r_a} = 0,80$	Y_o	3,32	6,70	8,36	10,53	12,20	13,62	15,30	16,72	18,00	17,82	16,72	14,90	11,88	8,36	4,60	2,42	0
	Y_u	3,32	1,51	0,84	0,17	0	0,33	0,84	1,26	1,76	2,34	2,51	2,59	2,59	1,84	1,09	0,59	0
$\frac{r}{r_a} = 0,96$	Y_o	3,76	6,60	8,20	10,40	11,90	13,10	14,90	16,60	17,60	17,50	16,10	14,20	11,30	7,79	4,18	1,67	0
	Y_u	3,76	1,67	0,84	0,33	0	0,08	0,58	0,84	1,67	1,84	2,01	1,67	1,67	1,09	0,59	0,25	0

105

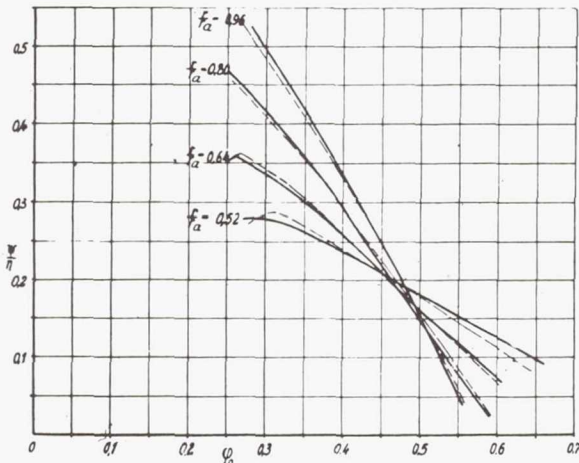


Figure 23.- Section characteristics for rotor III:----- for $k = 1$, $D = 0$; ——— for $D = 0$, but taking the cascade coefficient, k , of figure 22 into account.

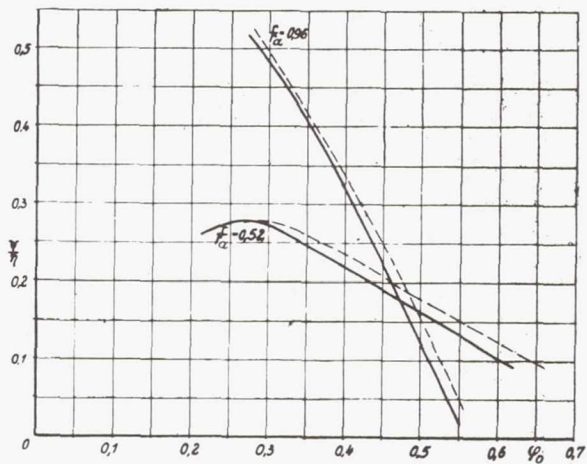


Figure 24.- Section characteristics for rotor III:----- takes into account the cascade coefficient of figure 22 but $D = 0$ (see figure 23); ——— takes into account the cascade coefficient k and the thickness correction $D\lambda^2$ of figure 22.

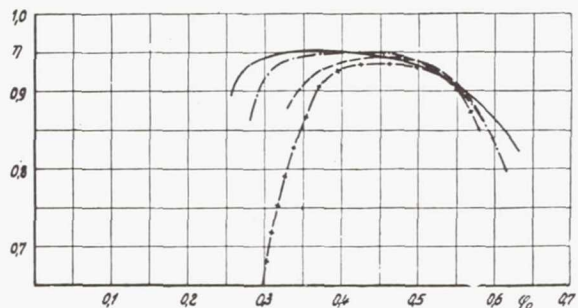
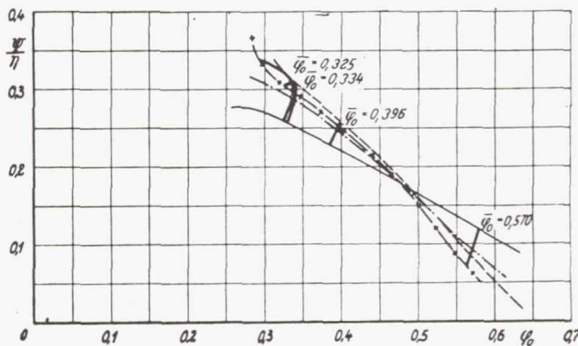


Figure 25.- Section characteristics for four sections of rotor I: —+— $r/r_a = 0.96$; ——— $r/r_a = 0.80$; ——— $r/r_a = 0.64$; ——— $r/r_a = 0.52$. The thick cross lines denote the operating points of the individual sections operating together.

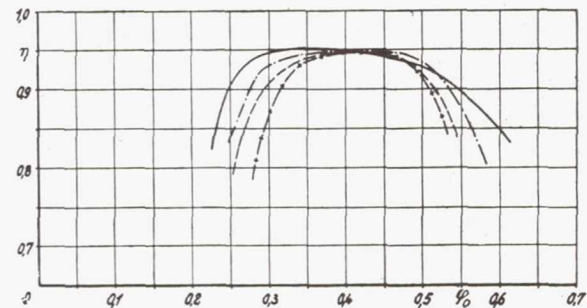


Figure 26.- Section characteristics for four sections of rotor II: —+— $r/r_a = 0.96$; ——— $r/r_a = 0.80$; ——— $r/r_a = 0.64$; ——— $r/r_a = 0.52$. The thick cross lines denote the operating points of the individual sections operating together.

106

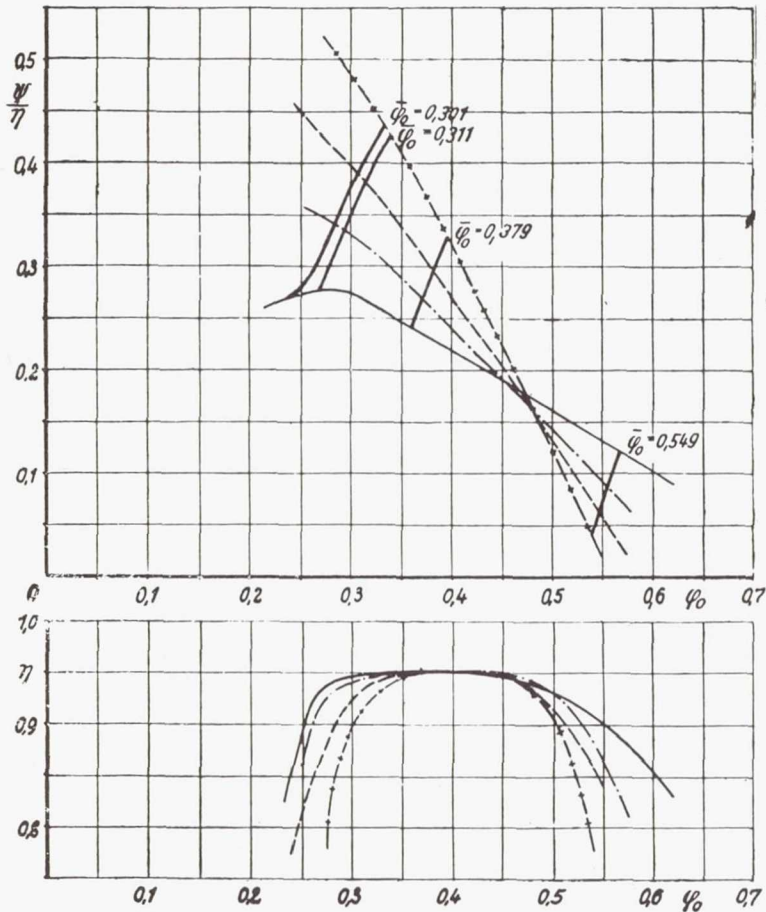


Figure 27.- Section characteristics for four sections of rotor III:
 — + — $r/r_a = 0.96$; — — — $r/r_a = 0.80$;
 — — — $r/r_a = 0.64$; — — — $r/r_a = 0.52$.
 The thick cross lines denote the operating points of the individual sections operating together.

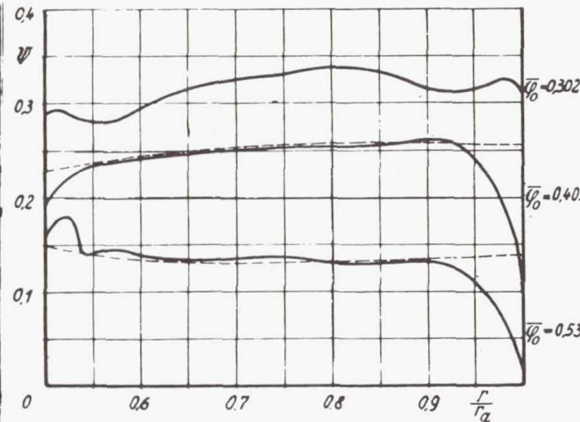


Figure 28.- Distribution of total head increase for rotor I [$\delta_1(r/r_a = 0.96) = 31^\circ$]: — from experiment and — — — from theory.

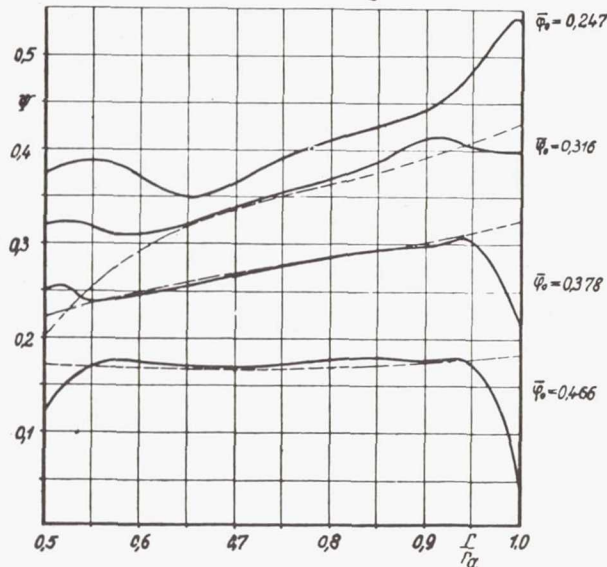


Figure 29.- Distribution of total head increase for rotor III [$\delta_1(r/r_a = 0.96) = 27.5^\circ$]: — from experiment and — — — from theory.

107

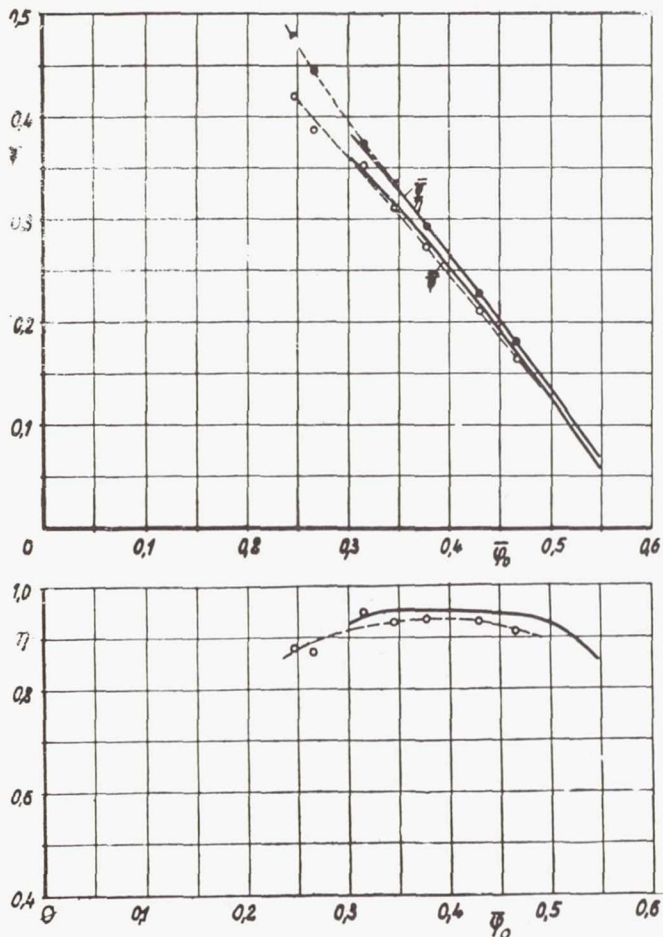


Figure 30.- Averaged rotor characteristics for rotor III [$\delta_1(r/r_a = 0.96)$

$= 27.5^\circ$]: ---●--- measured torque curve, ---○--- measured total head curve and measured efficiency, ——— theoretical mean curves.

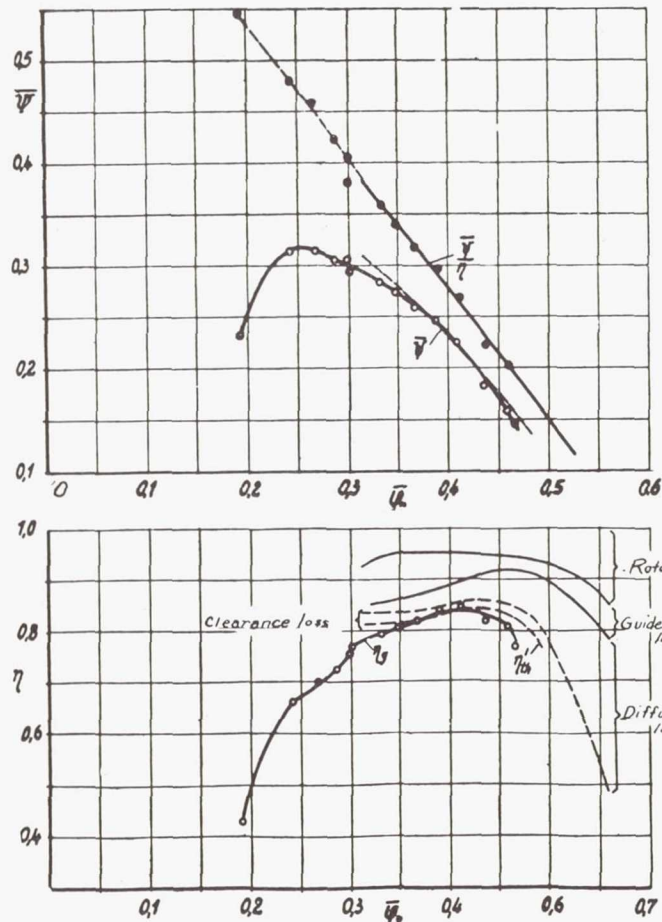


Figure 31.- Blower characteristic for rotor III [$\delta_1(r/r_a = 0.96) = 27.5^\circ$] and

stator I. The experimentally determined points are denoted by zero circles (see tab' 4).

108

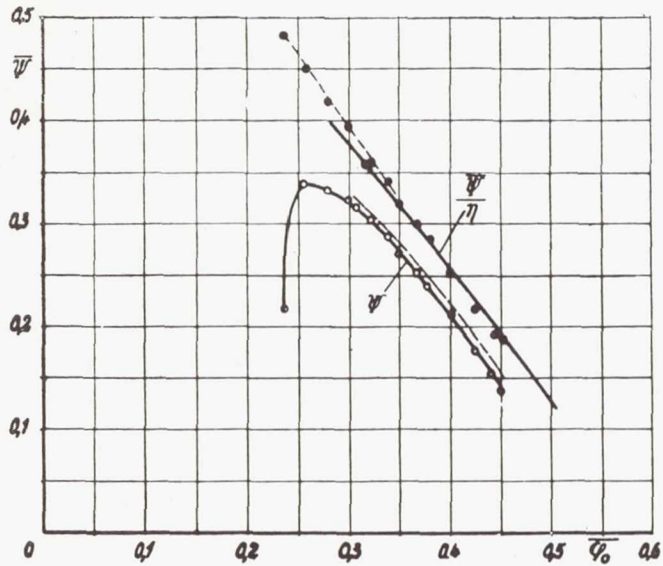


Figure 33.- Pressure-quantity curves for the blower installations: rotor I, II and III, each with exit guide vanes I. (Blade angles in accordance with figures 17 to 19).

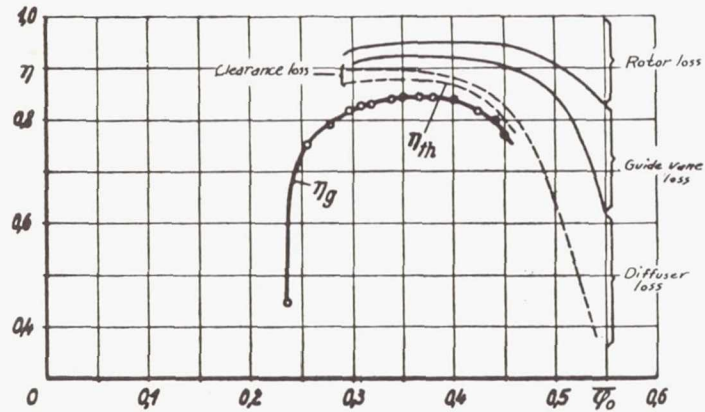
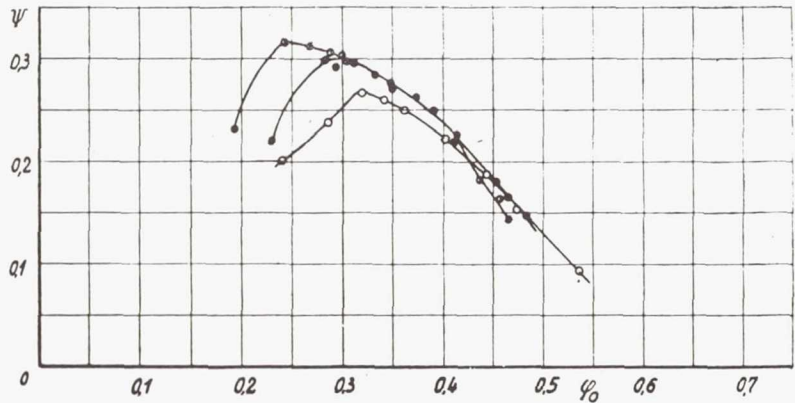


Figure 32.- Blower characteristic for rotor III [$\delta_1(r/r_a = 0.96)$ and stator II. The experimentally determined points are denoted by zero circles (see table 5 for $s/2r_a=0.002$).

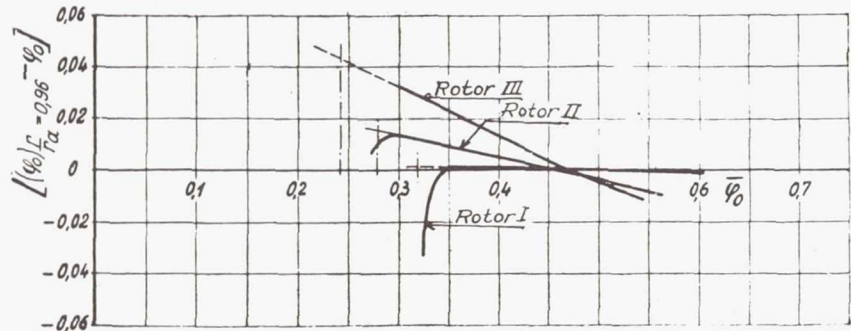


Figure 34.- Extrapolation of the throughflow coefficients for the section $r/r_a = 0.96$ from the mean throughflow coefficients for which the tests indicate separation of the rotor flow.

109

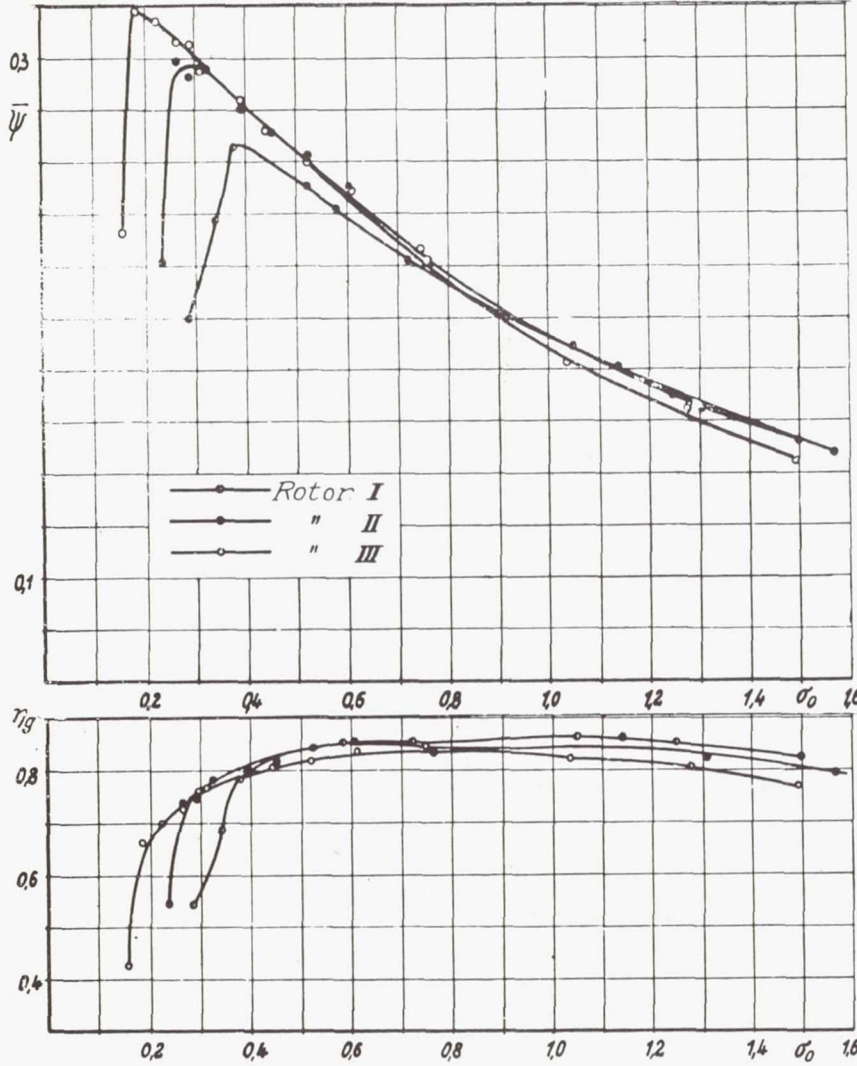


Figure 35.- Experimentally determined blower characteristics for the blower unit: rotor I, II, and III with stator I downstream, as a function of the throttling coefficient σ_0 . The rotor blade angles correspond to figures 17 to 19 (see table 4).

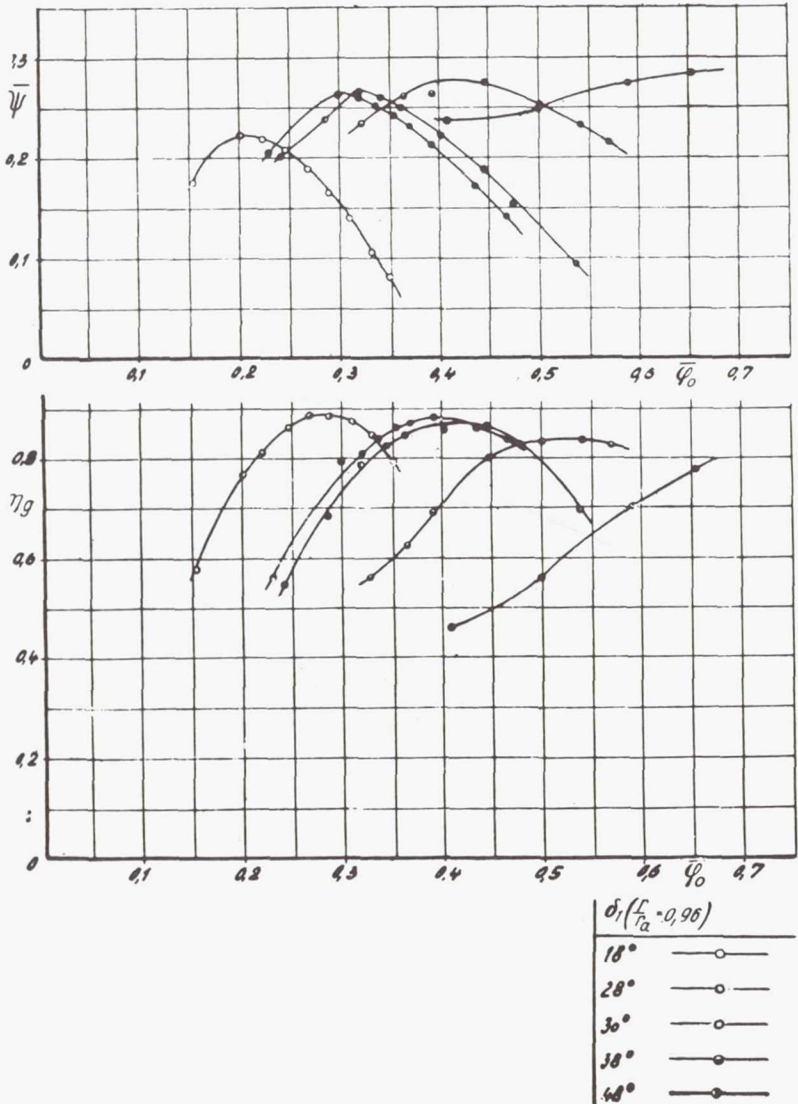


Figure 37.- Experimental blower characteristics for rotor I and exit stator I at various rotor blade angles (see table 4).

110

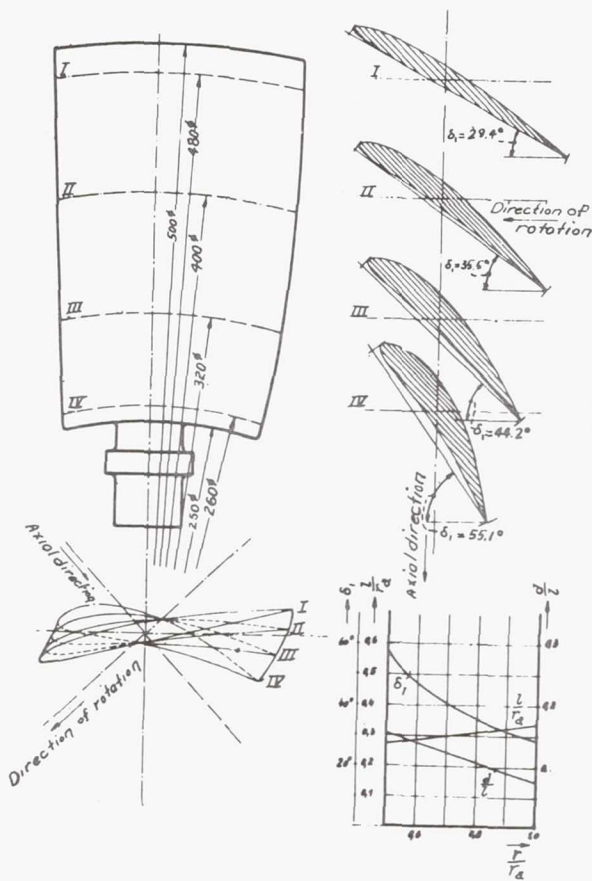


Figure 36.- Blades of the 13-bladed rotor IV (see table 3).

Table 3.
13 bladed rotor IV.

$\frac{r}{r_a}$	l	$\frac{d}{l}$	$\delta_1 = 90 - \delta$
0,52	68,10	0,149	55,10°
0,64	72,90	0,130	44,20°
0,80	79,10	0,100	35,50°
0,96	83,20	0,080	29,40°

Profile ordinates

X	0	1,25	2,50	5,0	7,5	10,0	15,0	20,0	30,0	40,0	50,0	60,0	70,0	80,0	90,0	95,0	100	
$\frac{r}{r_a} = 0,52$	Y_o	4,41	7,15	8,68	11,00	12,88	14,25	16,20	17,60	18,70	18,55	17,45	15,80	13,10	9,75	5,52	3,16	0,50
	Y_u	4,41	2,88	2,38	1,94	1,85	1,98	2,42	3,02	3,82	4,35	4,64	4,41	3,84	2,91	1,73	0,85	0
$\frac{r}{r_a} = 0,64$	Y_o	4,02	6,90	8,23	9,92	11,30	12,30	13,70	14,70	15,40	15,20	14,20	12,50	10,28	7,52	4,06	2,22	0,30
	Y_u	4,02	1,45	1,73	1,37	1,23	1,27	1,60	1,87	2,41	2,83	2,91	2,69	2,25	1,73	0,93	0,49	0
$\frac{r}{r_a} = 0,80$	Y_o	2,85	4,55	5,52	7,00	8,08	8,90	10,10	10,20	11,40	11,25	10,45	9,31	7,60	5,50	3,14	1,85	0,32
	Y_u	2,85	1,75	1,30	0,96	0,85	0,75	0,91	1,15	1,40	1,64	1,69	1,66	1,52	1,15	0,71	0,41	0
$\frac{r}{r_a} = 0,96$	Y_o	2,55	3,96	4,67	5,55	6,21	6,74	7,48	7,82	8,10	7,95	7,35	6,25	5,05	3,68	2,08	1,24	0,30
	Y_u	2,55	1,56	1,05	0,72	0,53	0,37	0,22	0,10	0,07	0	0	0	0	0	0	0	0



Table 4. Blower characteristics for rotor I. $\frac{s}{2r_a} = 0,002$. Stator I.

$\delta_1(\frac{r}{r_a} = 0,96) = 18^\circ$			$\delta_1(\frac{r}{r_a} = 0,96) = 28^\circ$			$\delta_1(\frac{r}{r_a} = 0,96) = 30^\circ$			$\delta_1(\frac{r}{r_a} = 0,96) = 38^\circ$			$\delta_1(\frac{r}{r_a} = 0,96) = 48^\circ$		
$\bar{\varphi}_0$	$\bar{\psi}$	η_σ												
0,349	0,082	0,791	0,466	0,142	0,833	0,536	0,095	0,698	0,570	0,216	0,827	0,652	0,283	0,775
0,331	0,105	0,846	0,435	0,172	0,860	0,479	0,153	0,823	0,540	0,232	0,837	0,590	0,277	0,703
0,311	0,139	0,875	0,394	0,212	0,880	0,445	0,189	0,863	0,500	0,253	0,833	0,505	0,250	0,558
0,288	0,162	0,882	0,370	0,231	0,868	0,402	0,223	0,857	0,446	0,273	0,803	0,409	0,239	0,462
0,269	0,189	0,885	0,354	0,243	0,860	0,362	0,251	0,844	0,393	0,264	0,688			
0,240	0,213	0,855	0,336	0,254	0,840	0,342	0,260	0,823	0,364	0,261	0,628			
0,221	0,218	0,810	0,318	0,261	0,810	0,318	0,266	0,787	0,322	0,235	0,563			
0,201	0,221	0,769	0,298	0,261	0,793	0,285	0,238	0,684						
0,154	0,175	0,578	0,229	0,204	0,560	0,241	0,201	0,547						

Blower characteristics for rotor II. $\frac{s}{2r_a} = 0,002$. Stator I.

$\delta_1(\frac{r}{r_a} = 0,96) = 18^\circ$			$\delta_1(\frac{r}{r_a} = 0,96) = 28^\circ$			$\delta_1(\frac{r}{r_a} = 0,96) = 38^\circ$			$\delta_1(\frac{r}{r_a} = 0,96) = 48^\circ$		
$\bar{\varphi}_0$	$\bar{\psi}$	η_σ									
0,364	0,083	0,714	0,482	0,148	0,799	0,591	0,224	0,806	0,694	0,329	0,783
0,344	0,110	0,790	0,466	0,165	0,827	0,566	0,245	0,833	0,655	0,327	0,790
0,313	0,159	0,850	0,454	0,181	0,863	0,523	0,266	0,820	0,593	0,335	0,757
0,293	0,186	0,860	0,412	0,222	0,846	0,468	0,297	0,807	0,472	0,293	0,547
0,282	0,200	0,860	0,390	0,250	0,857	0,428	0,308	0,770	0,400	0,270	0,467
0,266	0,213	0,837	0,350	0,272	0,820	0,395	0,307	0,723			
0,250	0,233	0,830	0,312	0,296	0,783	0,364	0,300	0,643			
0,219	0,253	0,784	0,293	0,293	0,746	0,315	0,246	0,525			
0,192	0,235	0,710	0,283	0,299	0,740						
0,166	0,211	0,572	0,229	0,221	0,545						

Blower characteristics for rotor III. $\frac{s}{2r_a} = 0,002$. Stator 1.

$\delta_1(\frac{r}{r_a} = 0,96) = 7,5^\circ$			$\delta_1(\frac{r}{r_a} = 0,96) = 17,5^\circ$			$\delta_1(\frac{r}{r_a} = 0,96) = 27,5^\circ$			$\delta_1(\frac{r}{r_a} = 0,96) = 37,5^\circ$			$\delta_1(\frac{r}{r_a} = 0,96) = 47,5^\circ$		
$\bar{\varphi}_0$	$\bar{\psi}$	η_σ	$\bar{\varphi}_0$	$\bar{\psi}$	η_σ	$\bar{\varphi}_0$	$\bar{\psi}$	η_σ	$\bar{\varphi}_0$	$\bar{\psi}$	η_σ	$\bar{\varphi}_0$	$\bar{\psi}$	η_σ
0,200	0,062	0,598	0,357	0,075	0,673	0,465	0,145	0,770	0,635	0,139	0,690	0,653	0,297	0,758
0,189	0,087	0,683	0,331	0,099	0,744	0,459	0,165	0,810	0,566	0,218	0,790	0,613	0,310	0,746
0,177	0,113	0,728	0,297	0,144	0,797	0,436	0,183	0,820	0,518	0,262	0,800	0,575	0,324	0,737
0,158	0,151	0,746	0,283	0,171	0,820	0,412	0,227	0,848	0,467	0,290	0,782	0,492	0,338	0,678
0,134	0,180	0,717	0,258	0,202	0,800	0,390	0,249	0,840	0,432	0,311	0,755	0,416	0,295	0,527
0,109	0,209	0,659	0,233	0,232	0,776	0,368	0,260	0,820	0,379	0,326	0,707	0,372	0,277	0,452
0,084	0,230	0,593	0,206	0,254	0,728	0,348	0,273	0,805	0,353	0,326	0,665			
0,071	0,236	0,542	0,185	0,263	0,710	0,333	0,284	0,793	0,322	0,303	0,590			
0,055	0,251	0,448	0,156	0,261	0,587	0,303	0,295	0,770	0,257	0,232	0,430			
						0,300	0,306	0,756						
						0,287	0,306	0,727						
						0,267	0,314	0,700						
						0,243	0,318	0,663						
						0,192	0,323	0,427						

112

Table 4. (Continued) Blower characteristics for rotor IV. $\frac{s}{2r_a} = 0,002$. Stator II.

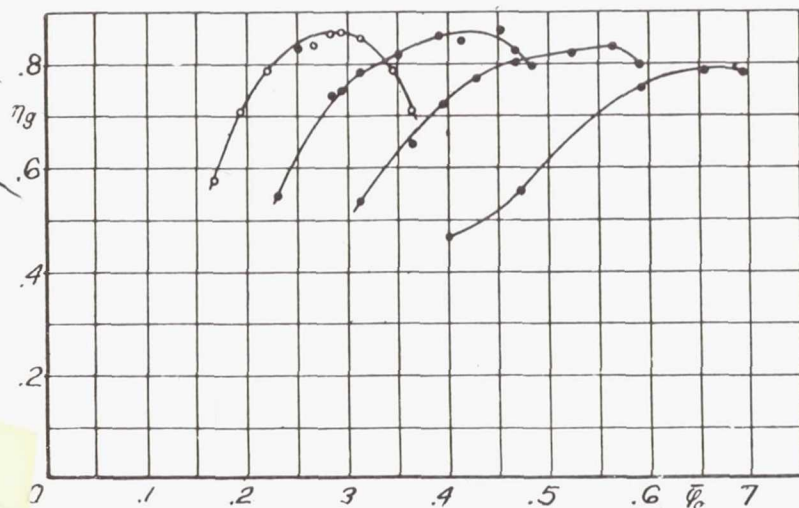
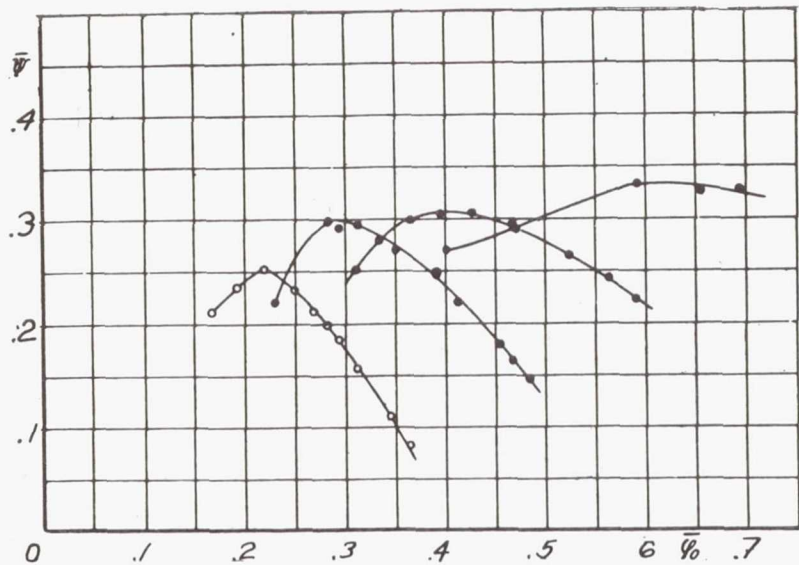
$\delta_1(\frac{r}{r_a}=0,96) = 9,5^\circ$			$\delta_1(\frac{r}{r_a}=0,96) = 19,5^\circ$			$\delta_1(\frac{r}{r_a}=0,96) = 24,5^\circ$			$\delta_1(\frac{r}{r_a}=0,96) = 29,5^\circ$			$\delta_1(\frac{r}{r_a}=0,96) = 34,5^\circ$			$\delta_1(\frac{r}{r_a}=0,96) = 39,5^\circ$			$\delta_1(\frac{r}{r_a}=0,96) = 44,5^\circ$		
$\bar{\varphi}_0$	$\bar{\psi}$	η_σ	$\bar{\varphi}_0$	$\bar{\psi}$	η_σ	$\bar{\varphi}_0$	$\bar{\psi}$	η_σ	$\bar{\varphi}_0$	$\bar{\psi}$	η_σ	$\bar{\varphi}_0$	$\bar{\psi}$	η_σ	$\bar{\varphi}_0$	$\bar{\psi}$	η_σ	$\bar{\varphi}_0$	$\bar{\psi}$	η_σ
0,233	0,082	0,587	0,377	0,092	0,646	0,436	0,126	0,710	0,502	0,166	0,744	0,572	0,213	0,754	0,628	0,266	0,780	0,682	0,312	0,766
0,220	0,131	0,723	0,351	0,128	0,725	0,415	0,168	0,780	0,475	0,221	0,798	0,527	0,273	0,809	0,597	0,298	0,795	0,649	0,350	0,798
0,210	0,156	0,773	0,334	0,181	0,797	0,395	0,211	0,810	0,438	0,270	0,825	0,483	0,319	0,815	0,566	0,325	0,800	0,613	0,377	0,798
0,197	0,192	0,778	0,297	0,255	0,842	0,357	0,270	0,830	0,391	0,326	0,823	0,458	0,342	0,823	0,516	0,371	0,810	0,555	0,417	0,797
0,178	0,230	0,780	0,278	0,272	0,828	0,328	0,301	0,820	0,357	0,361	0,822	0,418	0,378	0,805	0,489	0,386	0,800	0,517	0,433	0,791
0,158	0,260	0,743	0,250	0,317	0,800	0,313	0,326	0,820	0,330	0,378	0,796	0,379	0,411	0,797	0,441	0,417	0,790	0,453	0,441	0,753
0,132	0,290	0,708	0,220	0,341	0,760	0,276	0,358	0,790	0,286	0,400	0,747	0,348	0,427	0,765	0,394	0,442	0,760	0,432	0,453	0,734
0,097	0,314	0,585	0,206	0,347	0,723	0,235	0,377	0,720	0,256	0,413	0,711	0,317	0,428	0,733	0,380	0,439	0,750	0,336	0,316	0,511
0,061	0,352	0,428	0,164	0,284	0,546	0,183	0,251	0,480	0,185	0,256	0,410	0,228	0,249	0,446	0,283	0,282	0,476			

Table 5. Blower characteristics for rotor III. $\delta_1(\frac{r}{r_a}=0,96) = 28^\circ$. Stator II.

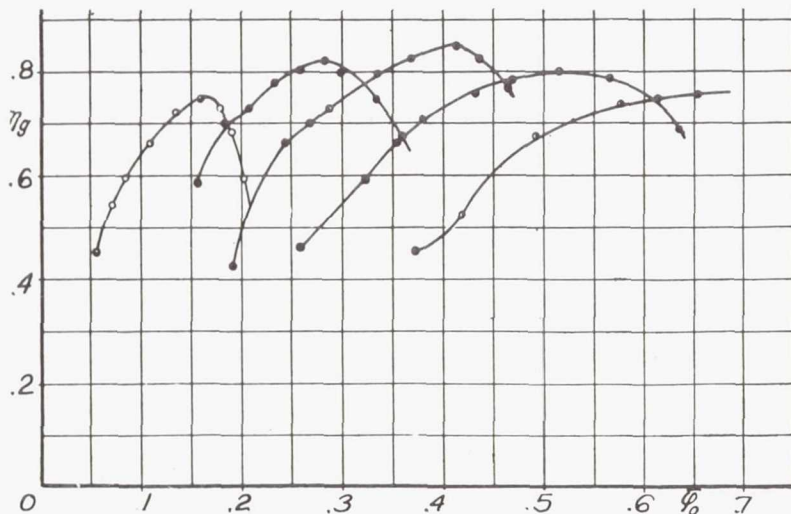
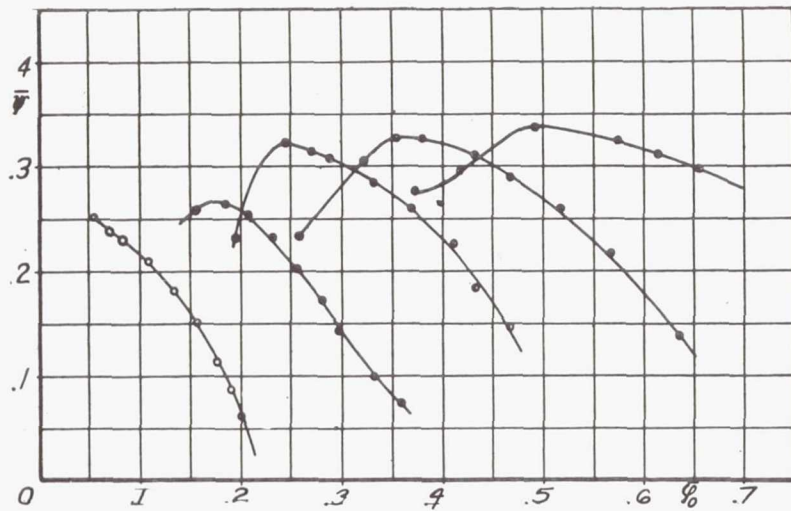
$\frac{s}{D} = 0,002$				$\frac{s}{D} = 0,004$				$\frac{s}{D} = 0,006$			
$\bar{\varphi}_0$	$\bar{\psi}$	η_σ	σ_0	$\bar{\varphi}_0$	$\bar{\psi}$	η_σ	σ_0	$\bar{\varphi}_0$	$\bar{\psi}$	η_σ	σ_0
0,451	0,137	0,773	1,50	0,442	0,131	—	1,49	0,440	0,132	0,710	1,47
0,443	0,165	0,800	1,263	0,428	0,151	—	1,21	0,432	0,148	0,740	1,26
0,425	0,179	0,817	1,010	0,416	0,195	—	0,885	0,415	0,170	0,770	1,01
0,401	0,211	0,840	0,760	0,388	0,208	0,827	0,721	0,388	0,207	0,790	0,725
0,380	0,240	0,840	0,602	0,372	0,231	0,813	0,598	0,374	0,229	0,800	0,612
0,368	0,254	0,846	0,531	0,343	0,291	0,820	0,403	0,347	0,262	0,810	0,459
0,351	0,273	0,845	0,454	0,313	0,292	0,798	0,335	0,317	0,293	0,790	0,342
0,340	0,288	0,842	0,402	0,290	0,309	0,784	0,271	0,289	0,304	0,780	0,274
0,322	0,304	0,830	0,338	0,267	0,315	0,744	0,226	0,258	0,300	0,720	0,221
0,308	0,317	0,824	0,299	0,214	0,237	0,560	0,193	0,212	0,228	0,550	0,197
0,300	0,324	0,820	0,276								
0,279	0,333	0,795	0,233								
0,256	0,339	0,750	0,193								
0,187	0,217	0,449	0,161								

$\frac{s}{D} = 0,008$				$\frac{s}{D} = 0,010$				$\frac{s}{D} = 0,012$			
$\bar{\varphi}_0$	$\bar{\psi}$	η_σ	σ_0	$\bar{\varphi}_0$	$\bar{\psi}$	η_σ	σ_0	$\bar{\varphi}_0$	$\bar{\psi}$	η_σ	σ_0
0,439	0,129	0,690	1,49	0,433	0,124	0,678	1,51	0,423	0,121	0,674	1,485
0,409	0,166	0,747	1,01	0,412	0,161	0,737	1,05	0,397	0,156	0,714	1,018
0,386	0,203	0,780	0,730	0,383	0,199	0,773	0,739	0,371	0,185	0,733	0,744
0,366	0,222	0,788	0,602	0,367	0,216	0,777	0,622	0,360	0,212	0,763	0,612
0,338	0,255	0,786	0,448	0,331	0,247	0,763	0,444	0,326	0,233	0,744	0,456
0,310	0,283	0,780	0,339	0,300	0,266	0,750	0,352	0,297	0,254	0,732	0,347
0,282	0,292	0,744	0,272	0,268	0,268	0,700	0,264	0,295	0,256	0,730	0,340
0,258	0,271	0,686	0,245	0,255	0,262	0,670	0,247	0,253	0,251	0,660	0,254
0,243	0,262	0,660	0,226	0,237	0,243	0,615	0,231	0,238	0,241	0,628	0,234

113



$d_1/r_a = 0.96$ Figure 38.- Experimental blower characteristics for rotor II and exit stator I at various rotor blade angles (see table 4).



$d_1/r_a = 0.96$ Figure 39.- Experimental blower characteristics for rotor III and exit stator I at various rotor blade angles (see table 4).

- $d_1/r_a = 0.96$
- 7.5° —○—
- 17.5° —●—
- 27.5° —○—
- 37.5° —○—
- 47.5° —○—

Handwritten scribbles.

Handwritten scribbles on a yellow sticky note.

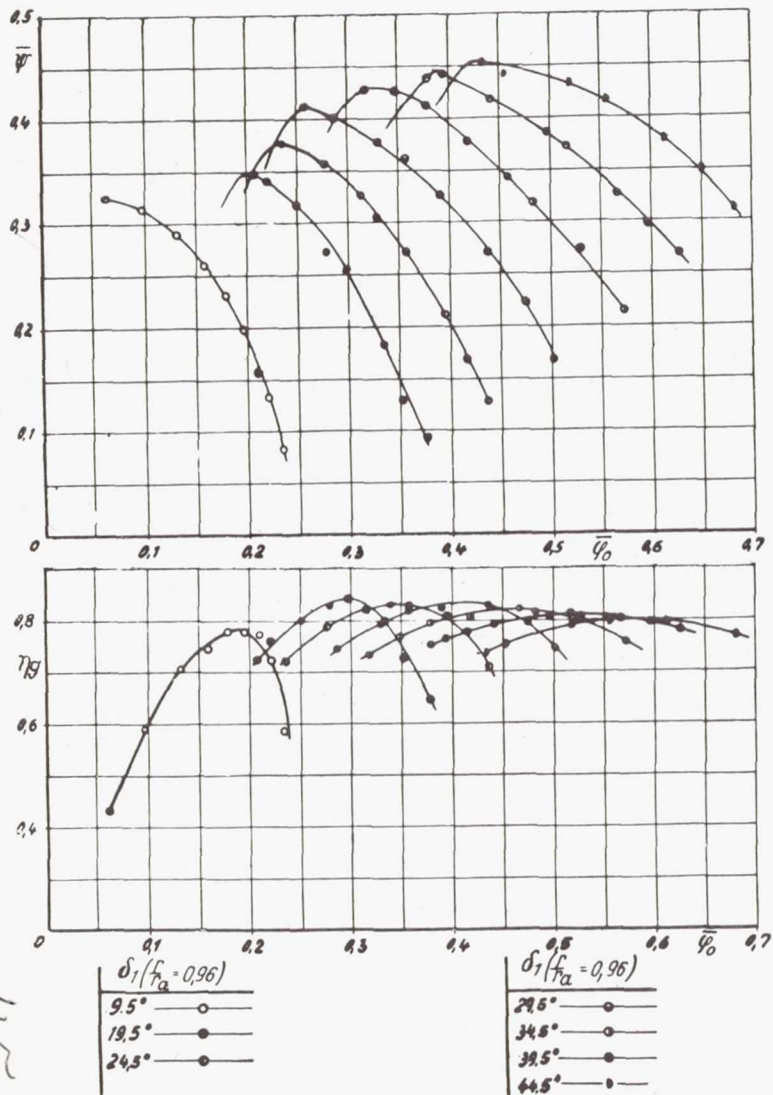


Figure 40.- Experimental blower characteristics for rotor IV and exit stator II at various rotor blade angles (see table 4).

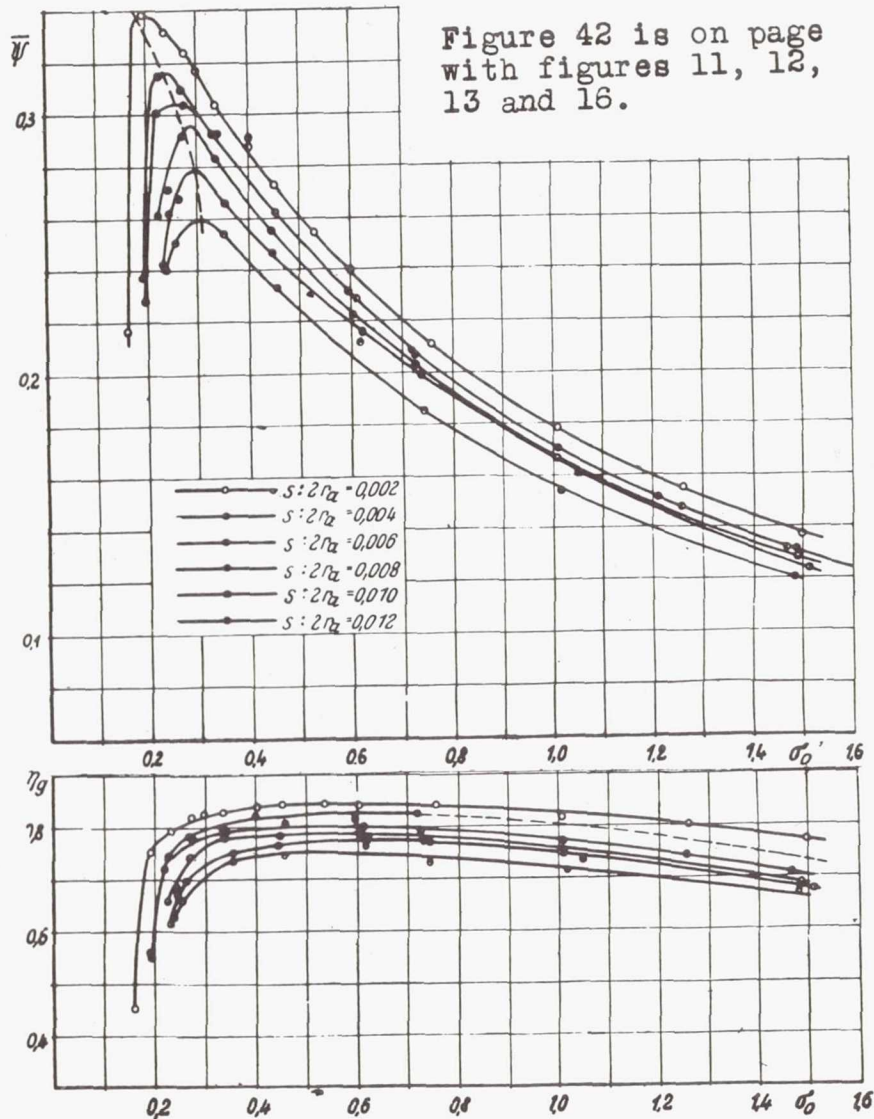


Figure 42 is on page with figures 11, 12, 13 and 16.

Figure 41.- Experimental blower characteristics for rotor III and exit stator II for various clearances between rotor blade and housing.